UNIVERSITY OF CALIFORNIA SAN DIEGO

Optimizing laser-ion acceleration with flat and structured foils

A dissertation submitted in partial satisfaction of the
requirements for the degree
Doctor of Philosophy

in

Engineering Sciences (Engineering Physics)

by

Joseph Strehlow

Committee in charge:

Professor Farhat Beg, Chair
Professor Alexey Arefiev
Dr. Christopher Holland
Professor Antonio Sanchez
Professor Clifford Surko
Professor David Whelan

2022

The thesis of Joseph Strehlow is approved, and it is acceptable in quality and form for publication on microfilm and electronically.

University of California San Diego

2022

DEDICATION

To my family, who have encouraged my curiosity since before I could walk.

EPIGRAPH

Happy the man, who, studying nature's laws,

Thro' known effects can trace the secret cause.

— Virgil, as interpreted by John Dryden

TABLE OF CONTENTS

LIST OF FIGURES

LIST OF TABLES

ACKNOWLEDGEMENTS

I remember it was almost 7 years ago when I was drafting my applications to PhD programs, committed to developing plasma-based particle accelerators. Professor Farhat Beg expressed an immediate willingness to support me via our first email exchange, and that has never wavered. Thank you, Farhat, for providing me the platform to become my own scientist, from my bewilderment of my first high power laser experiment, to successfully leading my own experiment in the twilight of my graduate program. For their mentorship in the laboratory or in the simulation box, Chris McGuffey, Mathieu Bailly-Grandvaux, Simon Bolaños, Joohwan Kim, and Daiki Kawahito have been invaluable. And for their infinite patience in answering my plasma theory questions over the years, I am indebted to Professors Chris Holland and Alex Arefiev.

To my academic peers, Krish Bhutwala, Nick Aybar, Sam Cordaro, and Brandon Edghill – our camaraderie the first couple years was unstoppable, and helped me push through my greatest self-doubts. From late night problem sets to tossing that beach ball (where did it come from?) around the office, there was always a background chaotic energy I fed into. There was never any hesitation in answering my trivial MATLAB questions, and our casual daily discussions helped me make minor breakthroughs culminating in this dissertation. I am grateful we became close long before covid reared its ugly head, and these daily moments between us abruptly became a mirage of the past.

To my best friends over in the Physics Department, Ryan Thiermann, Jason Platt, Mo Fizari, and Cameron Trapp – your combined extraversion was a welcome break from my home department. We camped, we surfed, and even managed to talk about topics other than physics most of the time. But out of all I had to leave behind in San Diego, I miss our beach bonfires the most.

To my mentors at Los Alamos National Laboratory, Sasi Palaniyappan, Cort Gautier, and Brian Albright, you bestowed upon me a trust and responsibility before I even had a chance to prove myself. Your faith in me as a young scientist has been a tremendous, and I value the

independence I have even before my postdoc has begun. I look forward to building a long career with you all at the Laboratory.

And finally, to Priscilla, the love of my life. You continue to help me trudge through the hard times and celebrate the victories, big and small. Thank you for finally bringing me out to New Mexico, albeit a bit sooner than I expected. I know we have wanted to call the mountains home long before we met, though I won't pretend we didn't have amazing years by the beach in San Diego, with access to more restaurants and coffee roasters than we could possibly explore in a lifetime. But no food scene can compare to the rugged canyons, pine forests, and snowcapped peaks right out our front door. I am so lucky to be here with you.

Chapter 4 contains a partial reprint as it appears in J. Strehlow, P. Forestier-Colleoni, C. McGuffey, M. Bailly-Grandvaux, T. S. Daykin, E. McCary, J. Peebles, G. Revet, S. Zhang, T. Ditmire, M. Donovan, G. Dyer, J. Fuchs, E. W. Gaul, D. P. Higginson, G. E. Kemp, M. Martinez, H. S. McLean, M. Spinks, H. Sawada, and F. N. Beg. "The response function of Fujifilm BAS-TR imaging plates to laser-accelerated titanium ions." *Review of Scientific Instruments* 90, 083302 (2019). The dissertation author is the primary investigator and author of this paper. This material is based on work supported by the Air Force Office of Scientific Research (AFOSR) under Award Number FA9550-14-1-0282, and by the Department of Energy, National Nuclear Security Administration (NNSA) under Award Number DE-NA0003842. The authors also acknowledge the support from the technical staff of the Texas Petawatt Laser at the University of Texas, Austin.

Chapter 5 contains a partial reprint of a manuscript in preparation for submission to *Scientific Reports*, as J. Strehlow, M. Bailly-Grandvaux, J. Kim, S. Bolanos, H. Smith, A. Haid, E.L. Alfonso, C. Aniculaesi, H. Chen, T. Ditmire, M.E. Donovan, B.M. Hegelich, T. Ma, H.S. McLean, H.J. Quevedo, M.M. Spinks, and F.N. Beg. "A laser parameter study on enhancing proton generation from microtube foil targets." The dissertation author is the primary investigator and author of this work. This work is supported by the DOE NNSA under Award Numbers

DE-NA0003842 and DE-NA0003525; by Triad National Security, LLC, for the DOE NNSA under Contract No. 89233218CNA000001; and by the DOE Office of Science, Fusion Energy Sciences under Contract No. DE-SC0021125, the LaserNetUS initiative at the Texas Petawatt Laser facility.

Chapter 6 contains a partial reprint as it appears in J. Strehlow, D. Kawahito, M. Bailly-Grandvaux, F. N. Beg, and G. M. Petrov. "The effects of laser pulse length and collisional ionization on the acceleration of titanium ions." *Plasma Physics and Controlled Fusion* 63, 065011 (2021). The dissertation author is the primary investigator and author of this paper. This material is based on work supported by the Department of Energy, National Nuclear Security Administration (NNSA) under Award Number DE-NA0003842. JS is partially funded by Sandia National Labs which is managed and operated by National Technology & Engineering Solutions of Sandia, LLC, a subsidiary of Honeywell International, Inc., for the U.S Dept. of Energy's National Nuclear Security Administration under contract DE-NA0003525. GP wishes to acknowledge financial support from Naval Research Laboratory 6.1 Base Program.

VITA

2016	B.S. in Engineering Physics, University of Illinois at Urbana-Champaign
2016-2022	Graduate Research Assistant, University of California San Diego
2022	Ph.D. in Engineering Sciences (Engineering Physics), University of California San Diego

PUBLICATIONS

J. Strehlow, M. Bailly-Grandvaux, J. Kim, S. Bolanos, H. Smith, A. Haid, E.L. Alfonso, C. Aniculaesi, H. Chen, T. Ditmire, M.E. Donovan, B.M. Hegelich, T. Ma, H.S. McLean, H.J. Quevedo, M.M. Spinks, and F.N. Beg. "A laser parameter study on enhancing proton generation from microtube foil targets." *Scientific Reports* (submitted 2022).

J. Strehlow, D. Kawahito, M. Bailly-Grandvaux, F. N. Beg, and G. M. Petrov. "The effects of laser pulse length and collisional ionization on the acceleration of titanium ions." *Plasma Physics and Controlled Fusion* 63, 065011 (2021).

A. Higginson, S. Zhang, M. Bailly-Grandvaux, C. McGuffey, K. Bhutwala, B. J. Winjum, J. Strehlow, B. Edghill, M. Dozières, F. S. Tsung, R. Lee, S. Andrews, S. J. Spencer, N. Lemos, F. Albert, P. King, M. S. Wei, W. B. Mori, M.J-E. Manuel, and F. N. Beg. "Electron acceleration at oblique angles via stimulated Raman scattering at laser irradiance $>10^{16}$ W/cm^2μm^2." *Physical Review E* 103, 033203 (2021).

M. Bailly-Grandvaux, D. Kawahito, C. McGuffey, J. Strehlow, B. Edghill, M.S. Wei, N. Alexander, A. Haid, C. Brabetz, V. Bagnoud, R. Hollinger, M.G. Capeluto, J.J. Rocca, and F.N. Beg. "Ion acceleration from microstructured targets irradiated by high-intensity, picosecond laser pulses." *Physical Review E* 102, 021201 (2020).

K. Bhutwala, M. Bailly-Grandvaux, J. Kim, M. Dozières, E. Galtier, C. B. Curry, M. Gauthier, E. Cunningham, H. J. Lee, P. Forestier-Colleoni, A. Higginson, N. Aybar, R. Hua, B. Edghill, J. Strehlow, G. M. Dyer, S. H. Glenzer, J. B. Kim, N. Alexander, E. D. Rio, M. S. Wei, Y. Ping, A. McKelvey, G. W. Collins, F. N. Beg, and C. McGuffey. "Development of a platform at the Matter in Extreme Conditions end station for characterization of matter heated by intense laser-accelerated protons." *IEEE Transactions on Plasma Science* 48, 2751 (2020).

J. Strehlow, P. Forestier-Colleoni, C. McGuffey, M. Bailly-Grandvaux, T. S. Daykin, E. McCary, J. Peebles, G. Revet, S. Zhang, T. Ditmire, M. Donovan, G. Dyer, J. Fuchs, E. W. Gaul, D. P. Higginson, G. E. Kemp, M. Martinez, H. S. McLean, M. Spinks, H. Sawada, and F. N. Beg. "The response function of Fujifilm BAS-TR imaging plates to laser-accelerated titanium ions." *Review of Scientific Instruments* 90, 083302 (2019).

M.J-E. Manuel, J. Strehlow, J. S. Green, D. Parker, E. L. Alfonso, J. Jaquez, L. Carlson, D. Neely, F. N. Beg, and T. Ma. "Intrinsic resolution limits of monolithic organic scintillators for use in rep-rated proton imaging." *Nuclear Instruments and Methods in Physics Research Section A: Accelerators, Spectrometers, Detectors and Associated Equipment* 913 (2019): 103-106.

ABSTRACT OF THE DISSERTATION

Optimizing laser-ion acceleration with flat and structured foils

by

Joseph Strehlow

Doctor of Philosophy in Engineering Sciences (Engineering Physics)

University of California San Diego, 2022

Professor Farhat Beg, Chair

The ability of relativistic laser pulses to accelerate ions from foil targets has long been established. These beams, with their high current density and ultrashort duration, are essential tools in high energy density science and have great promise as an upcoming technology in accelerator physics. To best fulfill their applications, the conversion efficiency of laser to ion energy must be optimized, with the ultimate goal of tunable ion energy, yield, and other beam parameters. The acceleration of both light and heavy ions is of interest, as they each have different uses, such as neutron generation and rare isotope production.

Two experiments were carried out at the Texas Petawatt laser facility. The first experiment studied the response of imaging plate detectors to heavy ions, expanding the published literature

beyond light ion calibrations. Successful modeling of the imaging plate's response function is essential to determining the absolute number of ions accelerated. A comparison of all published calibrations produces an empirical estimate for ion response for any arbitrary ion as a function of atomic mass. The second experiment investigated ion acceleration from 3D printed targets, whose protruding structure increases laser-target coupling. These structures were of the "microtube" geometry, and are most effective under the right conditions of laser intensity, pulse duration, and energy. These results are then compared to experiments on similar target structures at the PHELIX and ALEPH laser facilities, which also showed enhanced ion production.

A numerical study on heavy ion acceleration was also conducted, in an optimization of the generation of multiply charged titanium beams. A thickness scan on submicron targets was executed for two laser pulse lengths to determine the best performing target for each laser. In the relativistically induced transparency regime, we show that collisional ionization cannot be neglected for sufficiently long laser pulses (near picosecond). Identifying this threshold is crucial for balancing the conservation of computational resources with accurate particle-in-cell modeling.

This large body of experimental and numerical data continue to support the tremendous progress in short pulse laser-ion acceleration over the course of three decades. Continuing to push the bounds in conversion efficiency and beam control is essential for breaking ground in high energy density physics and accelerator development.

Chapter 1

Introduction

1.1 High energy density physics with short pulse lasers

A plasma, a collection of freely flowing charges, expands across a broad regime of density and temperatures. From solar wind, with a Debye length of 100 m [1], to a fs laser incident on a 100 nm foil, plasma spans many orders of magnitude in characteristic space and time scales. Therefore, it is sensible to divide the broad topic of plasma physics into sub-fields to address fundamental questions. One such dividing line can be drawn for plasmas with energy densities exceeding 10^{11} J/m^3, corresponding to 1 MBar of pressure. These systems, holding the energy density necessary to readily ionize hydrogen, fall under the category of High Energy Density Physics, or HEDP [2]. As shown in Figure 1.1, these phenomena, such as inertial confinement fusion (ICF) require an unprecedented combination of mass density and temperature.

The United States contains several large facilities for accessing the HEDP regime. The National Ignition Facility (NIF) and Z-Machine, both operated by the US Department of Energy, are capable of delivering >1 MJ of energy to a small volume, $\sim$1 mm^3 for NIF and $\sim$100 mm^3 for Z. The smaller-scale Omega laser delivers 40 kJ to a similar volume as NIF. Fortunately, access to a billion-dollar facility is not necessary to reach HEDP conditions. Tightly focused

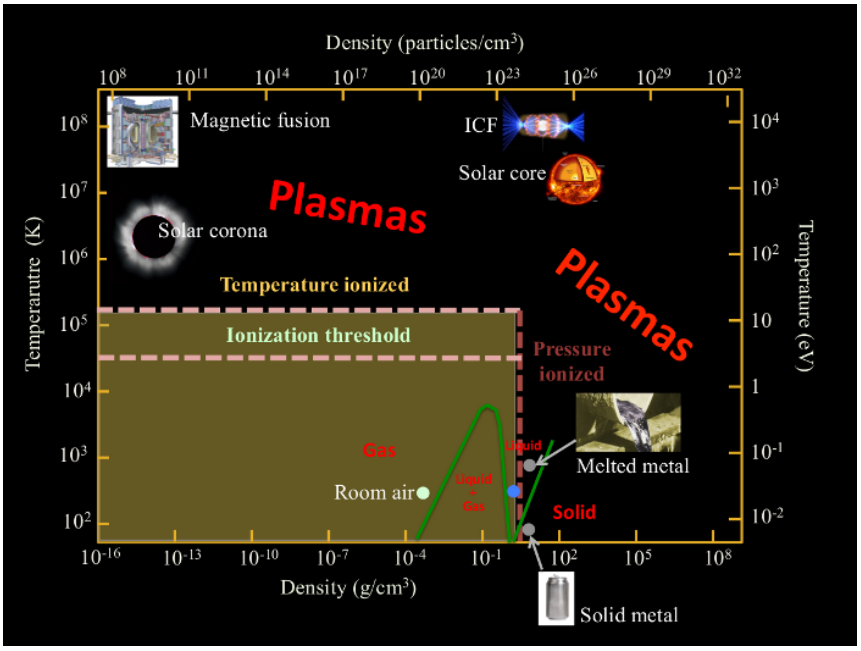

Figure 1.1: The broad regimes of plasma physics spanning density and temperature space. High energy density physics (HEDP) encompasses inertial confinement fusion (ICF) and the solar core. Figure courtesy of Ref. [3].

lasers, which can deliver up to hundreds of Joules in a $\sim$10 μm focal spot, are more accessible to the everyday scientist. These PetaWatt (PW) class lasers are ultrafast in duration ($\lesssim$ ps), yet can readily reach the HEDP regime to generate energetic bursts of secondary radiation.

These radiation sources, in addition to having practical applications, are interesting vehicles to studying HEDP in their own right. Studying the laser acceleration of ions, for example, sheds light into fluid instabilities in the relativistic regime [4], as well as the ability of radiation pressure pistons to drive shock waves [5]. These beams can also be used as tools to generate exotic states of matter [6], and for imaging plasmas [7]. Laser-driven ions can also generate neutrons via a beam-target interaction, which can be used to investigate nuclear processes in a compact platform [8].

Laser-driven electrons also have a diversity of applications. The high fluxes of electrons emitted from a laser-matter interaction can be used for radiography [9] and transport studies in dense plasmas [10]. With multi-GeV energies, laser-electron accelerators even have promise

towards compact particle colliders [11]. Conveniently, there is tremendous overlap in the generation of energetic electrons and ions. Due the relatively high mobility of electrons compared to ions, electrons are the primary absorber of laser energy. Energetic electrons can then transfer their energy to the ions in a variety of ways, including electrostatic forces [12, 13] and the aforementioned fluid instabilities and shock waves.

Decades of work have been devoted to improving laser-driven radiation sources. For ion acceleration, the focus of this dissertation, the field has evolved from the first rigorous explanation of an acceleration mechanism in 2001 [12], to shooting additively manufactured structures in the laboratory [14, 15] in the 2020's. One of the main avenues of research today is improving the coupling of laser energy into the target, in the quest for higher ion energies and conversion efficiencies. In addition to structured targets, the aerial density of a foil target can also be optimized. A thickness scan on plastic foils at the Vulcan laser resulted in the current energy record for proton acceleration: up to 97 MeV [16]. The reason for such resounding success is that for thick targets, the laser is inefficiently absorbed and only the surface contaminants (i.e. residual water and oils on the foil from the environment) are accelerated favorably. For ultrathin targets, the foil disintegrates before the laser can be efficiently be absorbed. This intermediate target regime, explained in detail in Section 2.2, gives rise to many interesting plasma phenomena on a micron scale length, such as relativistically induced transparency (RIT) and shock formation. The broader regime of highly relativistic plasma physics was largely inaccessible until the late 20th century due to the lack of a sufficient driver, i.e. a laser pulse of sufficient intensity. In the section that follows, a brief history of laser technology is presented, as it is important to understand the rise of the tool that enables this field to exist.

1.2 Evolution of high power laser technology

The history of the laser arguably begins with Albert Einstein's work on the quantization of light. In his seminal 1916 work [17], he was able to expand upon Max Planck's classically derived formalism. Via equipartition, Planck derived his famous relation which yields the spectral radiance B of a blackbody:

$$U(\nu, T) = \frac{2h\nu^3}{c^2} \frac{1}{e^{h\nu/k_B T} - 1} \tag{1.1}$$

where ν is the frequency, T is the temperature, h is Planck's constant, k_B is Boltzmann's constant, and c is the speed of light. For a two-level system, an atom can emit or capture a photon of frequency ν as $E_2 - E_1 = h\nu$. The population rate of change for each level can be written as:

$$\frac{dn_1}{dt} = An_2 + B_{21}Un_2 + B_{12}Un_1 = 0 \tag{1.2}$$

$$\frac{dn_2}{dt} = -An_2 + B_{21}Un_2 + B_{12}Un_1 = 0 \tag{1.3}$$

where A and B are the so-called Einstein coefficients. The An_2 term represents the spontaneous emission rate of the system, $B_{21}Un_2$ the stimulated emission, and $B_{12}Un_1$ the absorption. A decade later, in 1928, the process was experimentally verified with electrostatic gas discharges by Hans Kopfermann and Rudolf Ladenburg.[18]. In 1950, Alfred Kastler proposed that a bright light source can drive the above equations of population out of equilibrium ("optical pumping"), achieving what is now known as population inversion [19].

The first practical generator of stimulated emission, known as the maser (microwave amplification by stimulated emission of radiation), was invented by a team at Columbia University in 1953. The device achieved population version of ammonia (NH_3) by electrostatically separating the upper from lower inversion states. The upper states are focused, and the lower states defocus,

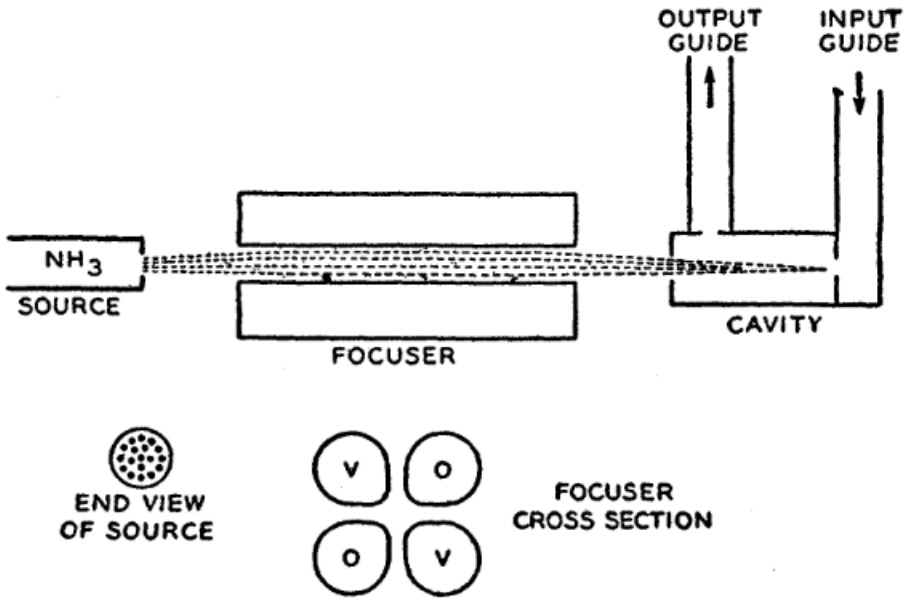

Figure 1.2: Simplified sketch of the original maser, completed in 1953 at Columbia University. The focuser directs ammonia (NH_3) of an inverted state into the resonant cavity. Image courtesy of Ref. [20].

directing the upper inversion population into a microwave resonant cavity. Figure 1.2 shows a sketch of the device from the original paper of Gordon, Zeiger, and Townes [20], which operated at 24 GHz (12 mm wavelength).

The "optical maser", now known today as a laser, soon followed. In 1960, Theodore Maiman at the Hugh Research Laboratories employed the optical pumping technique to drive the first flash of laser light. Two techniques, Q-switching and mode-locking, followed to increase the intensity at best focus well beyond 10^{10} W/cm^2. Q-switching uses a shutter, either passive or active, to allow the buildup of population inversion in the cavity. This technique can generate laser beams of GW power in a ns pulse. Mode-locking, however, generates Watts of power in an ultrashort pulse ($\ll$ ns). To mode-lock a laser, a cavity can be designed so the laser light produces a train of pulses locked in phase, narrowing the duration of each individual pulse [21].

These two techniques led to a rapid progress in focused intensity throughout the 1960s, where it saturated around 10^{15} W/cm^2. As seen in Figure 1.3, the next revolution occurred

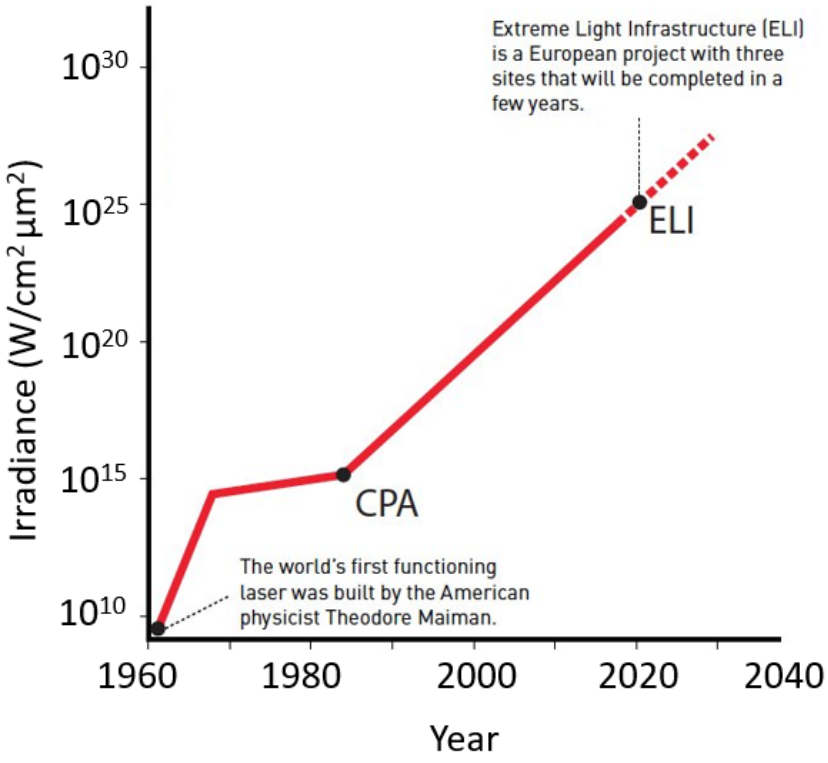

Figure 1.3: Progress in maximally achieved laser intensity since the invention of the laser. Figure modified from Ref. [22].

in 1985 with the invention of chirped pulse amplification (CPA). Before this technology, any efforts to increase the focused intensity were met with the amplifying material being destroyed. However, a similar effect was achieved with microwaves at Bell Labs in 1960 [23]. Microwaves were sent through a positively dispersive delay line to achieve the desired chirp, followed by the amplification stage. To adapt this technique to optical pulses, Strickland and Mourou implemented two stages of gratings. The first pair stretches the pulse to lower its peak power, where then it can go through the amplifier without damaging it. After amplification, the second pair can then re-compress the pulse to its original duration. Though this often happens in stages, a cartoon of a simple one-stage system is described in Figure 1.4. The invention of the CPA was awarded half of the Nobel Prize in Physics in 2018. A recent achievement of this technology occurred in 2021, when the Center for Relativistic Laser Science (CoReLS) achieved a record intensity of

10^{23} W/cm^2 [24].

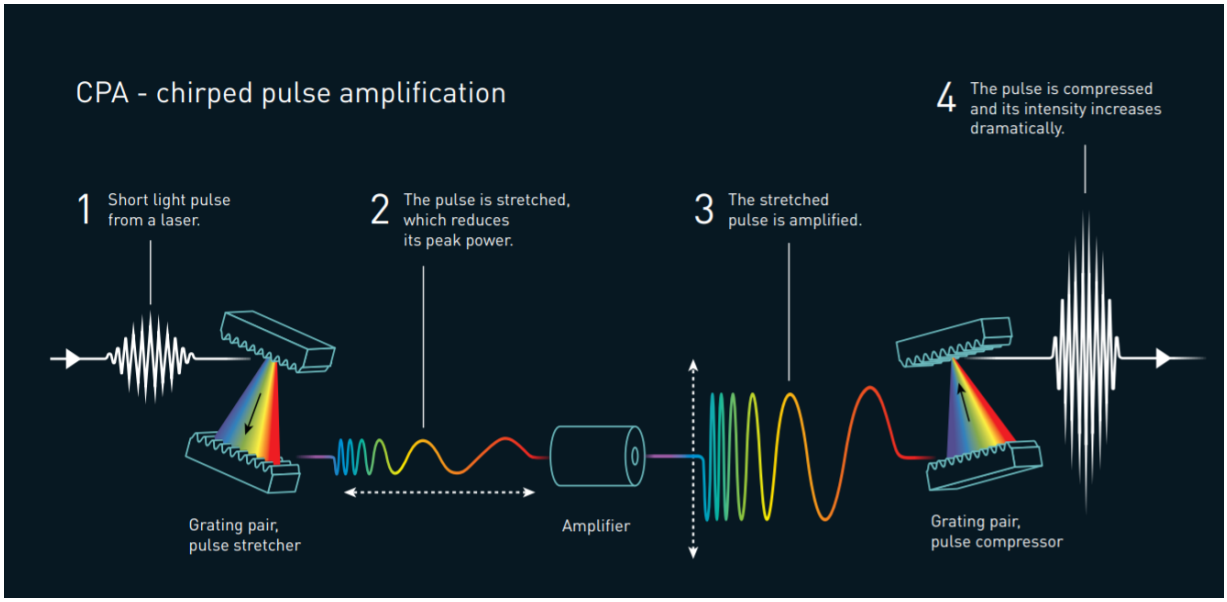

Figure 1.4: Cartoon of chirped pulse amplification (CPA). Figure courtesy of Ref. [22].

For most practical cases, high intensity laser experiments operate at 10^{20} – 10^{21} W/cm^2. At this regime, relativistic kinematics is certainly important, but the dominance of non-classical phenomena, such as quantum electrodynamics (QED), is generally considered negligible except in very extreme cases. For the purposes of this work, relativistic plasma physics is satisfactory, and the following analysis of this work proceeds as such.

1.3 Outline of the dissertation

Chapter 2 provides an introduction to plasma physics. It begins by giving the definition of a plasma and defining crucial spatial and time scales. A transition into laser-plasma physics follows, describing plasma response to an electromagnetic wave. Single-particle motion and both collective effects are addressed, along with an examination of absorption mechanisms. The chapter concludes with an in-depth survey of laser-ion acceleration, outlining the transitions between different acceleration regimes, accompanied by the derivations of analytical models.

Chapter 3 gives a comprehensive overview of the experimental and numerical methods necessary for conducting the body of the dissertation. This chapter first illustrates the details of the Texas Petawatt (TPW) laser system. This laser was employed for the experiments described in Chapters 4 and 5, and its laser parameters formed the basis of the numerical study in Chapter 6. The choice of diagnostics for various experiments is explained, along with the fabrication techniques of advanced targets fielded by the author. Details of the FLASH and PIC codes used to support this dissertation are also presented.

Chapter 4 introduces the most common detectors fielded in laser-plasma experiments, detailing their composition and use. A calibration of an imaging plate detector is conducted for an uncalibrated ion species. This calibration is then compared to other peer-reviewed works.

Chapter 5 details an experimental investigation on proton acceleration from 3D printed targets of the microtube geometry. An optimum set of laser parameters are found for the targets by varying the laser energy, intensity, and pulse length. For laser pulses of exceedingly high energy, the microtube targets are shown to be similarly effective as readily available flat targets. These results are corroborated by radiation-hydrodynamic and particle-in-cell simulations.

Chapter 6 describes a numerical study aimed at optimizing heavy ion acceleration with ultrathin foils. Two laser pulses of the same intensity but different pulse lengths are studied, incident on foils ranging from 10 - 500 nm. The optimum thickness is determined by the concurrency of target transparency with the arrival of the laser peak, in good agreement with established literature. The acceleration dynamics are analyzed in rigor, revealing that radiation pressure and shock wave acceleration follow in stages to drive fast ions into the TNSA sheath field. These processes appear in both pulse durations studied (140 and 650 fs). The distribution of multiply charged ions, both in physical and energy space, is evaluated with and without collisions.

Chapter 7 concludes the dissertation, unifying the body of work in the mission to optimize laser-ion acceleration with a scan of laser and target parameters. Updated imaging plate calibrations are presented that extend the work of this dissertation. The author also expresses an

interest in further benchmarking the modeling codes and investigating the role of dimensionality in these studies. A future experiment on structured targets for γ-ray generation is also proposed.

1.4 Role of the author

For the imaging plate (IP) detector calibration study presented in Chapter 4, the author etched the CR-39 track detectors with P. Forestier-Colleoni. The author determined the response function of the IP to energetic titanium ions by matching the data set of both the CR-39 and IP detectors. The author also compared the published IP calibrations with his own to fit a broad trend to estimate IP response to any arbitrary energetic ions. The author was not present for the beam time at the Texas Petawatt Laser.

In the experiment conducted in Chapter 5, the author designed the experiment along with C. McGuffey, M. Bailly-Grandvaux, D. Kawahito, and F. N. Beg. The author, with help from M. Bailly-Grandvaux, commissioned the targets from General Atomics to be additively manufactured. During the beam time, the author was the Principal Investigator at the Texas Petawatt (TPW), with significant support in the target area from S. Bolanos, H. Smith, and M. Bailly-Grandvaux. The author analyzed the Thomson and electron spectrometer data, S. Bolanos analyzed the RCF data, and M. Bailly-Grandvaux analyzed the x-ray spectra. M. Bailly-Grandvaux and J. Kim ran supporting simulations and assisted the author with interpreting the results.

In the numerical investigation presented in Chapter 6, the author and D. Kawahito designed the study based on past experimental results at the Texas Petawatt and Trident lasers. D. Kawahito ran the simulations. The author primarily conducted the post-processing of the simulations, but is indebted to D. Kawahito for his guidance throughout. The author determined the ion acceleration mechanisms at play and the roles of collisional processes and pulse length, with assistance from D. Kawahito and M. Bailly-Grandvaux.

Chapter 2

Plasma theory

2.1 Introduction to laser-plasma interactions

When a high-intensity laser pulse interacts with neutral atoms, rapid ionization occurs at the rising edge of the pulse. Thus begins the onset of the laser-plasma interaction, in which the laser and plasma exchange energy in a variety of processes. Examples of these processes include single particle motion, the ponderomotive force, the absorption of the laser pulse, and ion acceleration. These phenomena are introduced in detail in the following sections

2.1.1 Propagation of an EM wave in a plasma

When an EM wave, such as a laser, propagates into a plasma, the dispersion relation of the EM wave is modified. The modification arises from the plasma's response to the EM wave. We begin with Maxwell's equations (specifically Faraday's law and Ampere's law) in a vacuum.

$$\nabla \times \mathbf{E} = -\frac{d\mathbf{B}}{dt} \tag{2.1}$$

$$c^2 \nabla \times \mathbf{B} = \frac{d\mathbf{E}}{dt} \tag{2.2}$$

Taking the curl of Ampere's law and substituting it into Faraday's law yields:

$$c^2 \nabla \times (\nabla \times \mathbf{B}) = \nabla \times \frac{d\mathbf{E}}{dt} = -\frac{d^2\mathbf{B}}{dt^2} \tag{2.3}$$

The assumption that the EM wave oscillates sinusoidally, as $e^{i(kx-\omega t)}$, yields:

$$\omega^2 \mathbf{B} = -c^2 \mathbf{k} \times (\mathbf{k} \times \mathbf{B}) \tag{2.4}$$

The "curl of curl" vector identity can then be applied:

$$\omega^2 \mathbf{B} = -c^2 [\mathbf{k}(\mathbf{k} \cdot \mathbf{B}) - k^2 \mathbf{B}] \tag{2.5}$$

Since the field components of an EM wave are perpendicular to the direction of propagation, $\mathbf{k} \cdot \mathbf{B} = 0$, simplifying the result to a familiar relation.

$$\omega^2 \mathbf{B} = -c^2 [0 - k^2 \mathbf{B}] \tag{2.6}$$

$$\omega^2 = c^2 k^2 \tag{2.7}$$

Now that we have derived the dispersion relation for an EM wave in vacuum, it can be readily modified to account for plasma response. To do so, Ampere's law must include the so-called displacement current term, as:

$$c^2 \nabla \times \mathbf{B} = \frac{d\mathbf{E}}{dt} + \mathbf{J}/\varepsilon_0 \tag{2.8}$$

Taking the curl of Faraday's law:

$$\nabla \times (\nabla \times \mathbf{E}) = -\nabla \times \frac{d\mathbf{B}}{dt} \tag{2.9}$$

$$\nabla(\nabla \cdot \mathbf{E}) - \nabla^2 \mathbf{E} - \nabla \times \frac{d\mathbf{B}}{dt}$$

Again taking the sinusoidal assumption of EM wave oscillations:

$$-\mathbf{k}(\mathbf{k} \cdot \mathbf{E}) + k^2 \mathbf{E} = \frac{i\omega}{\varepsilon_0 c^2} J + \frac{\omega^2}{c^2} \mathbf{E} \tag{2.10}$$

Since the field components of the EM wave are perpendicular to propagation, $\mathbf{k} \cdot \mathbf{B} = 0$.

$$(\omega^2 - c^2 k^2)\mathbf{E} = \frac{i\omega}{\varepsilon_0} \mathbf{J} \tag{2.11}$$

In the plasma, the ions are generally stationary, meaning the EM wave dispersion is dominantly modified by the electrons. The electron equation of motion is:

$$m \frac{\partial v}{\partial t} = -e\mathbf{E} \tag{2.12}$$

which becomes $v = \frac{e\mathbf{E}}{im\omega}$ due to sinusoidal behavior. With the electron current density as $J = -n_0 e v$, we can then substitute into Equation 2.11.

$$(\omega^2 - c^2 k^2)\mathbf{E} = \frac{i\omega}{\varepsilon_0} \frac{n_0 e^2 \mathbf{E}}{i\omega m} = \frac{n_0 e^2}{\varepsilon_0 m} \mathbf{E} \tag{2.13}$$

where the right-hand-side coefficient of $\mathbf{E}$ is the square of the electron plasma frequency (ω_p^2). This value represents the characteristic electron response time in a plasma. We now reach the conclusion that, when propagating in a plasma, the dispersion relation of an EM wave is:

$$\omega^2 = \omega_p^2 + c^2 k^2 \tag{2.14}$$

From this relation, an important property of laser-plasma interactions can be extracted. If the laser frequency exceeds the plasma frequency ($\omega \geq \omega_p$), the k-vector of the laser becomes imaginary. The maximum density of propagation, known as the critical density n_c, can be found readily by equating the plasma frequency with the frequency of an EM wave in vacuum.

$$\omega_p^2 = \omega^2 \tag{2.15}$$

$$\frac{n_c e^2}{\varepsilon_0 m} = c^2 k^2 \tag{2.16}$$

$$n_c = \varepsilon_0 m \omega^2 / e^2 \tag{2.17}$$

This can be written in practical units as $n_c = \frac{1.1\times10^{21}}{\lambda^2}$, where n_c is in cm^{-3} and the laser wavelength λ is in μm. When $n_0 \geq n_c$, the k-vector becomes imaginary, meaning the laser cannot propagate into the plasma beyond the skin depth δ. The skin depth can be calculated as:

$$e^{ikx} = e^{|k|x} = e^{-x/\delta} \tag{2.18}$$

$$\delta = \frac{1}{|k|} = \frac{c}{(\omega_p^2 - \omega^2)^{1/2}} \tag{2.19}$$

The skin depth can play an important role in laser-ion acceleration in specific regimes, as discussed further in Section 2.2.

2.1.2 Trajectory of an electron in an EM wave

To further study the response of a plasma to an EM wave, we can begin with the trajectory of a single electron. We start with the nonrelativistic regime ($v << c$). Let us take a plane wave propagating in the x-direction, such that

$$\mathbf{E} = E_0 \hat{\boldsymbol{\varepsilon}} e^{i(kx-\omega t)} \tag{2.20}$$

$$\mathbf{B} = \hat{x} \times \mathbf{E} \tag{2.21}$$

where $\hat{\boldsymbol{\varepsilon}}$ denotes the axis of electric field polarization. For non-relativistic motion, the B-field term of the Lorentz force on the electron can be neglected, yielding

$$m\frac{d\mathbf{v}}{dt} = -e\mathbf{E} \tag{2.22}$$

The electron velocity $\mathbf{v}$ and trajectory $\mathbf{r}$ can then be readily calculated via integration:

$$\mathbf{v} = -\frac{e\mathbf{E}}{im\omega} \tag{2.23}$$

$$\mathbf{r} = \frac{e\mathbf{E}}{m\omega^2} \tag{2.24}$$

The maximum velocity of the electron is $v_0 = eE_0/m\omega$. Normalizing for $v << c$, we find the dimensionless laser amplitude a_0.

$$a_0 = \frac{eE_0}{m\omega c} \tag{2.25}$$

For a_0 approaching unity, the magnetic force must be accounted for, which can be done as a perturbation for the first term on the order of a_0 and the second of order a_0^2. The total velocity $\mathbf{v}$ is broken down into two components, $\mathbf{v} = \mathbf{v}_1 + \mathbf{v}_2$, where $\mathbf{v}_1$ is the linear term and $\mathbf{v}_2$ is the perturbation. The $\mathbf{v}_1$ term dominates transverse motion (E-field component) and $\mathbf{v}_2$ is responsible for longitudinal motion ($\mathbf{v}_2$) as we shall see shortly.

$$m\frac{d(\mathbf{v}_1+\mathbf{v}_2)}{dt} = -e(\mathbf{E}+\frac{\mathbf{v}_1+\mathbf{v}_2}{c}\times\mathbf{B}) \tag{2.26}$$

Equating the terms of order a_0^2, we can approximate

$$m\frac{d\mathbf{v}_2}{dt} = -\frac{\mathbf{v}_1}{c}\times e\mathbf{B} \tag{2.27}$$

We assume the $\mathbf{v}_2$ perturbation does not contribute to the magnetic force since $\mathbf{v}_1$ is the primary driver of this term. Such an approximation also makes a straightforward analytical solution of the electron trajectory possible. For an EM wave of linear polarization, we assume that the $\mathbf{v}_1$ motion is dominated by the E-field.

$$\mathbf{v}_1 = \frac{eE_0}{m\omega}\hat{y}sin(\omega t) = a_0 c\hat{y}sin(\omega t) \tag{2.28}$$

$$y = -\frac{a_0 c}{\omega}cos(\omega t) \tag{2.29}$$

Substituting in for $\mathbf{v}_1$ and $\mathbf{B}$ into Equation 2.27

$$\frac{d\mathbf{v}_2}{dt} = -\frac{e}{mc}\hat{x}[a_0 csin(\omega t)][E_0 cos(\omega t)] \tag{2.30}$$

$$\frac{d\mathbf{v}_2}{dt} = -\frac{1}{2}a_0\hat{x}\omega csin(2\omega t) \tag{2.31}$$

Integrating to find the longitudinal velocity and position:

$$\mathbf{v}_2 = \frac{1}{4}a_0^2 ccos(2\omega t)\hat{x} \tag{2.32}$$

$$x = \frac{a_0^2 c}{8\omega}sin(2\omega t) \tag{2.33}$$

Combining the trajectories in x and y (Equations 2.33 and 2.29, respectively), we find the electron trajectory correct for up to order a_0^2:

$$16X^2 = Y^2(1-Y^2) \tag{2.34}$$

for $X = \omega x/a_0^2 c$ and $Y = \omega y/a_0 c$. Plotting the trajectory produces a figure-of-eight shape, as seen in Figure 2.1.

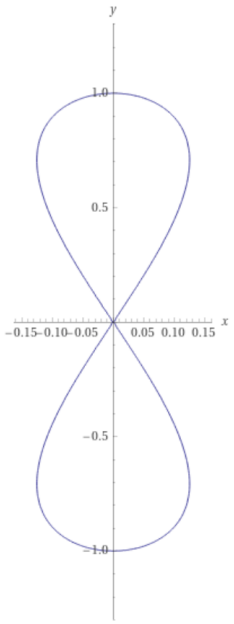

Figure 2.1: The normalized trajectory of an electron in a plane wave, as plotted from Equation 2.34. The electric field is responsible for the transverse oscillations, and the magnetic field drives the longitudinal oscillations.

The use of a_0 is still valid in the relativistic regime, but it requires an updated definition. Since it is the normalized amplitude of the electric field of a plane wave, a_0 can instead be defined using the laser intensity. The intensity is the cycle-averaged value of the Poynting vector:

$$I = <|S|> = \left\langle \frac{|E \times B|}{c/4\pi} \right\rangle = \frac{c}{8\pi}\left(\frac{m\omega c a_0}{e}\right)^2 \tag{2.35}$$

Solving for a_0 and converting to practical units:

$$a_0 = 0.85 \left(\frac{I\lambda^2}{10^{18}\ [\mathrm{W/cm^2}]} \right)^{1/2} \tag{2.36}$$

2.1.3 Ponderomotive force

Laser pulses are of a finite spot size, and thus have a gradient, stretching from the peak intensity (or electric field), out to infinity, where the laser field is zero. This electric field gradient generates a force on a charged particle. Our analysis begins by investigating electron motion in an oscillating electric field, but this time with a small perturbation.

$$m\frac{d\mathbf{v}}{dt} = -eE_0(y)cos(\omega t)\hat{y} \tag{2.37}$$

The motion can be broken up into two combined trajectories, as $x = x_0 + x_1$, where x_0 is its oscillating behavior, and x_1 is its guiding center drift.

$$m\frac{d^2x}{dt^2} = -e\left(E_0 + x_1\frac{\partial E_0}{\partial x} \right) cos(\omega t) \tag{2.38}$$

Averaging over one cycle for the oscillating motion yields:

$$m\frac{d^2x_0}{dt^2} = -e\frac{\partial E_0}{\partial x} < x_1 cos(\omega t) > \tag{2.39}$$

Assuming the electric field gradient is slowly varying over space, $E_0 >> x_1\frac{\partial E_0}{\partial x}$. This justifies the assumption that for x_1 motion, we can neglect the gradient term.

$$\frac{d^2x_1}{dt^2} = -\frac{eE_0}{m}cos(\omega t) \tag{2.40}$$

The trajectory of x_1 can be readily found by integrating twice:

$$x_1 = \frac{eE_0}{m\omega^2}cos(\omega t) \tag{2.41}$$

Substituting x_1 into the cycle-averaged motion for x_0 (Equation 2.39), and generalizing $\frac{\partial E_0}{\partial x}$ to ∇, we find the so-called "ponderomotive force":

$$m\frac{d^2x_0}{dt^2} = -\frac{e^2}{4m\omega^2}\nabla E_0^2 = \mathbf{F}_{pond} \tag{2.42}$$

From this formula, two immediate consequences of laser-plasma interactions emerge. Firstly, the inverse mass dependence indicates that very light particles (i.e. electrons) are pushed out very rapidly, much more than their heavy counterparts. In effect, the ponderomotive force acts primarily on electrons, and ions stay effectively stationary, unless acted upon by other electrostatic effects, such as the formation of plasma sheaths or space charge build-up. Another consequence of this force is charge independence. Any charged particle present in the laser field will be pushed away from the center, regardless of sign.

The ponderomotive force can also be estimated in the highly relativistic regime, for electrons with $a_0 \sim \gamma >> 1$. First, the series expansion of γ can be taken, to find how γ scales with electron velocity.

$$\gamma = (1 - v^2/c^2)^{-1/2} \rightarrow \gamma \sim v^2 \tag{2.43}$$

Velocity in turn scales linearly with electric field, as seen in Equation 2.22. a_0 is also directly proportional to E. As such a simple substitution can be made to estimate the order of the ponderomotive force:

$$\mathbf{F}_{pond} = -\frac{e^2}{4m\omega^2}\nabla E_0^2 = -\frac{1}{4}mc^2\nabla\left(\frac{e^2E_0^2}{m^2\omega^2c^2}\right) = -\frac{1}{4}mc^2\nabla(a_0^2) \tag{2.44}$$

$$\mathbf{F}_{pond} \approx mc^2\nabla\gamma \tag{2.45}$$

Though this derivation is far from rigorous, it still allows the physicist to build an intuition

for the transition to the relativistic regime. For a mathematically rigorous derivation (spanning many pages), see Chapter 5 of *High Power Laser-Matter Interaction* by Peter Mulser & Dieter Bauer [25].

2.1.4 Absorption mechanisms

Inverse bremsstrahlung absorption

Collisions with ions can dephase electrons from the laser pulse, thus robbing the laser of some of its energy. Collisions generally are more dominant in classical plasmas rather than relativistic laser-plasma interactions. Since it is non-relativistic, the magnetic component of the Lorentz force can be neglected. Instead, a collisional damping term must be introduced to the electron equation of motion in an oscillating electric field.

$$m\frac{d\mathbf{v}}{dt} = -\frac{eE}{m} - \nu_{ei}\mathbf{v} \tag{2.46}$$

where ν_{ei} is the frequency of electron-ion collisions. Assuming oscillatory motion as $e^{i(kx-\omega t)}$, the equation of motion can be linearized to be:

$$\mathbf{v} = -\frac{ie}{m(\omega + i\nu_{ei})}\mathbf{E} \tag{2.47}$$

Incorporating the electron current density $J = -en\mathbf{v}$:

$$\mathbf{J} = \frac{ine^2}{m(\omega + i\nu_{ei})} \tag{2.48}$$

It is evident that $\mathbf{J}$ depends on the plasma frequency, so we can rewrite:

$$\mathbf{J} = \frac{i\omega_p^2}{4\pi m(\omega + i\nu_{ei})} \tag{2.49}$$

Taking the curl of Ampere's law and combining with Faraday's law:

$$\nabla \times (\nabla \times \mathbf{E}) = -\frac{1}{c}\frac{\partial}{\partial t}(\nabla \times \mathbf{B}) = -\frac{1}{c}\left(\frac{4\pi}{c}\mathbf{J} + \frac{1}{c}\frac{\partial \mathbf{E}}{\partial t}\right) \tag{2.50}$$

Again taking the assumption of oscillatory motion, and substituting **J** for **E**:

$$k^2\mathbf{E} = -\frac{\omega}{c}\left(\frac{i\omega_p^2}{4\pi m(\omega + i\nu_{ei})}\mathbf{E} - \frac{\omega}{c^2}\mathbf{E}\right) \tag{2.51}$$

$$\left(\frac{kc}{\omega}\right)^2 = 1 - \frac{\omega_p^2}{\omega^2(1+i\nu_{ei})} \approx 1 - \left(\frac{\omega_p}{\omega}\right)^2\left(1 + \frac{i\nu_{ei}}{\omega}\right) \tag{2.52}$$

For low-density plasmas, it is valid to assume that the laser frequency is much greater than the frequency of electron-ion collisions ($\omega >> \nu_{ei}$). This justifies the series expansion

$$k \approx \frac{\omega}{c}\left[1 - \left(\frac{\omega_p}{\omega}\right)^2\right]^{1/2}\left(1 + \frac{i\nu_{ei}}{2\omega}\left(\frac{\omega_p}{\omega}\right)^2\frac{1}{1-\omega_p^2/\omega^2}\right) \tag{2.53}$$

k is now separated in terms of its real and imaginary terms, where the imaginary component represents the damping. Equation 2.53 can be distilled into the following form:

$$k = k_{Re} + \frac{1}{2}ik_{Im} \tag{2.54}$$

Matching the imaginary term k_{Im} to the imaginary term of Equation 2.53, the damping rate for the inverse bremsstrahlung mechanism (κ_{IB}) is found to be

$$\kappa_{IB} \approx \frac{\nu_{ei}}{c}\left(\frac{\omega_p}{\omega}\right)^2\left[1 - \left(\frac{\omega_p}{\omega}\right)^2\right]^{-1/2} \tag{2.55}$$

For a Maxwellian plasma, we can determine the damping rate's dependence on fundamental plasma parameters. In this case the collision frequency scaling can be used to determine the κ_{IB} scaling, as κ_{IB} varies linearly with ν_{ei}.

$$\nu_{ei} \propto \frac{n_e Z}{T_e^{3/2}} \tag{2.56}$$

An immediate conclusion of this scaling is that lower temperature, higher-Z plasmas have more collisions, and thus are more readily damping of an EM wave. It is also evident that, due to the ω_p/ω dependence, absorption is highest near the critical density surface. For very low collision frequencies, like in relativistic plasmas, inverse bremsstrahlung does not play a significant role. However, there are routes to a plasma absorption of laser energy without collisions. The remainder of this section is devoted to these mechanisms, known collectively as "collisionless absorption."

Resonance absorption

Resonance absorption is a mechanism of collisionless absorption that does not require relativistic laser intensities. However, it does require the plasma to have a density gradient. In addition, the polarization of the laser electric field must have a component along the axis of the gradient. Mathematically speaking, $\mathbf{E} \cdot \nabla n_e \neq 0$ is required to drive electrostatic waves into the plasma. In addition to assumed density gradient ∇n_e, we decompose the laser electric field as $\mathbf{E} = \mathbf{E}_\parallel + \mathbf{E}_\perp$. We begin the analysis of laser absorption into the plasma with Poisson's equation.

$$\nabla \cdot (\varepsilon \mathbf{E}) = \varepsilon \nabla \cdot \mathbf{E} + \nabla \varepsilon \cdot \mathbf{E} \tag{2.57}$$

Solving for the divergence of $\mathbf{E}$:

$$\nabla \cdot \mathbf{E} = -\frac{1}{\varepsilon} \mathbf{E}_\parallel \nabla_\parallel \varepsilon \tag{2.58}$$

where ε is the plasma dielectric. As the laser cannot propagate past the critical density, the dielectric function approaches 0, driving $\nabla \cdot E$ to infinity. However, the laser electric field can still deposit energy into the plasma. First we assume that the scale length L of the plasma is much

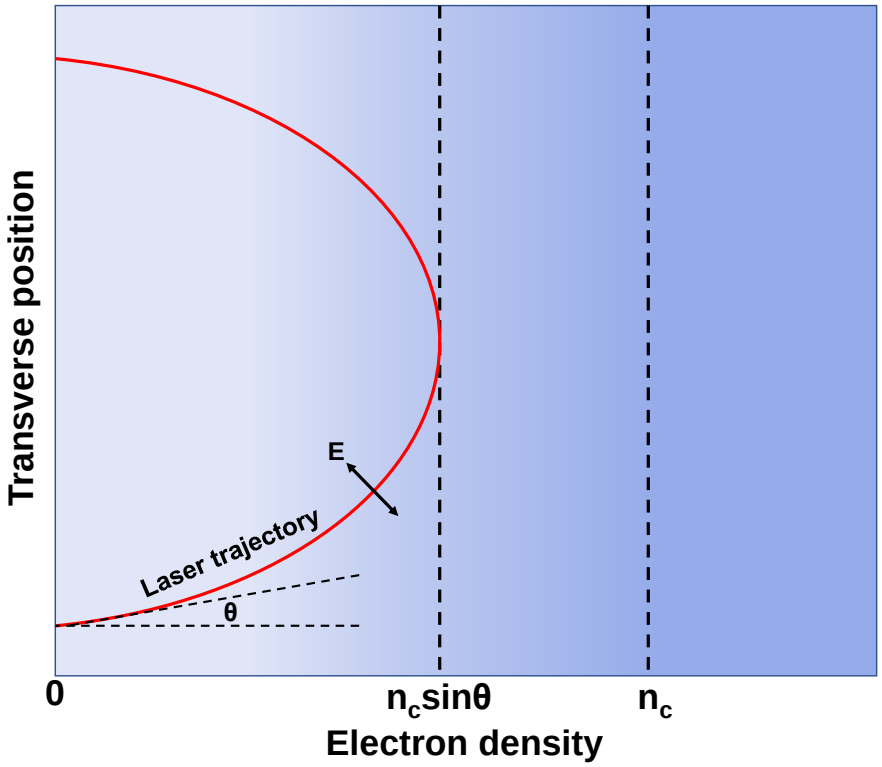

Figure 2.2: An illustration of the resonance absorption mechanism. A long plasma gradient increases from 0 out to overcritical along the horizontal axis. The vertical axis shows the laser trajectory, incident at angle θ, and then reflected by the critical surface. A component of the laser electric field must be parallel to the density gradient for the field to drive density oscillations and deposit energy. This absorption fraction maximises at 20° (Equation 2.72).

larger than the electron's displacement in the electric field. Specifically, we are interested in the longitudinal component of its oscillatory displacement, which we now define as x_{osc}.

$$L >> x_{osc} = \frac{eE}{m\omega^2} \tag{2.59}$$

For small density fluctuations δn:

$$\delta n = (x + x_{osc})n_e - n_e \tag{2.60}$$

Differentiating with respect to x:

$$\frac{\partial n}{\partial x} = \frac{(x + x_{osc})n_e - n_e}{x_{osc}} \tag{2.61}$$

$$\delta n \approx x_{osc} \frac{\partial n}{\partial x} \tag{2.62}$$

By Snell's law, the laser wave is reflected at an angle of incidence characterized by $\sin^2\theta$. To calculate $\mathbf{E}_{\parallel}$ at the critical surface, we first find the magnetic field.

$$\mathbf{B} = \mathbf{B}_{\parallel} exp(\frac{i\omega}{k_{\perp} c}\sin\theta - i\omega t) \tag{2.63}$$

Making the substitution for $\mathbf{B}$ into Ampere's law:

$$\nabla \times \mathbf{B} = \frac{i\omega_L}{c}\mathbf{B}_{\parallel}\sin\theta(\frac{i\omega}{k_{\perp} c}\sin\theta - i\omega t) \tag{2.64}$$

where ω_L is the laser frequency. To determine $B_{\parallel}$ at the critical density, we assume it decays exponentially out from the critical surface, as $\mathbf{B}e^{-\beta}$. For the $\sin^2\theta$ reflection, the Airy function solution is approximately

$$\mathbf{B} \approx 0.9\mathbf{E}_L \left(\frac{cL}{\omega_L}\right)^{1/6}. \tag{2.65}$$

The decay constant of the field β can be found by integrating along the imaginary component of the k-vector.

$$\beta = \frac{1}{c}\int_{L\cos\theta}^{L} (\omega_p^2 - \omega_L^2\cos^2\theta)^{1/2} dz = \frac{2\omega L}{3c}\sin^3\theta \tag{2.66}$$

Evaluating $\mathbf{B}$ at $z = L$:

$$B = 0.9\mathbf{E}_L \left(\frac{cL}{\omega_L}\right)^{1/6} \exp(-\frac{2\sin^3\theta}{3c}) \tag{2.67}$$

To simplify the expression, two variables are introduced, defined as

$$\phi(\tau) = 2.3\tau e^{-2\tau^3/3} \tag{2.68}$$

$$\tau = \left(\frac{\omega_L L}{c}\right)^{1/3} \sin\theta \tag{2.69}$$

These condense into the expression for the electrostatic field at the critical density E_s as a function of laser field E_L.

$$E_s = \frac{E_L}{\sqrt{2\pi\omega_L L/c}}\phi(\tau) \tag{2.70}$$

The oscillations must be damped in order for the electrons to transfer their energy into the plasma. For a damping coefficient ν, the absorbed laser intensity is

$$I_{abs} = \int \nu \frac{E_z}{8\pi} dz = \frac{\nu}{8\pi}\left(\frac{E_L}{\varepsilon}\right)^2 \approx \frac{\omega_L L E_L^2}{8\pi} \tag{2.71}$$

For some absorbed fraction f_A, it is evident that it scales with the ϕ function, as $f_A = \frac{\phi^2(\tau)}{2}$. The maximum absorption depends on the angle of laser incidence, maximizing at

$$\theta = \arcsin[0.8(\omega_L L/c)^{-1/3}] \approx 20^\circ \tag{2.72}$$

From PIC simulations [26, 27], the absorption at this angle maximizes at $\sim$60%, and produces a Maxwell-Boltzmann distribution of hot electrons. In practical units, the temperature of the hot electrons scales as

$$T_{hot} \sim 14(I\lambda^2 T_{cold})^{1/3} \tag{2.73}$$

where T_{hot} and T_{cold} are the hot and background electron temperatures, respectively, in keV. The

intensity I is in 10^{16} W/cm^2, and laser wavelength λ is in μm.

This absorption mechanism is most active for laser intensities of $10^{15} - 10^{17}$ W/cm^2. Collisional absorption begins to dominate at lower intensities, and at relativistic intensities, other mechanisms of collisionless absorption take over as the magnetic field of the laser pulse grows significant. However, first we will investigate another mechanism of non-relativistic absorption, which also requires oblique incidence, but with a sharp density gradient.

Vacuum heating

An obliquely incident laser incident on a plasma with a steep density gradient can deposit its energy via vacuum heating, also known as Brunel absorption [28]. For $\mathbf{E} \cdot \nabla n_e \neq 0$, a capacitor-like electric field arises at the steep gradient, as

$$\Delta E_c = 4\pi e \Sigma \tag{2.74}$$

where ΔE_c is the capacitor-like electric field and $\Sigma = n_e \delta x$, where δx is the small longitudinal displacement of the electrons. Equating the driving electric field (longitudinal component of the laser field) to the capacitor field, we can then solve for Σ.

$$\Sigma = \frac{2E_L \sin\theta}{4\pi e} \tag{2.75}$$

In the vacuum, each electron acquires a longitudinal velocity that is a component of its oscillatory motion, as:

$$v_L = 2v_{osc} \sin\theta \tag{2.76}$$

As these electrons dephase from the laser pulse over the critical surface, the total energy absorbed from the laser pulse can be calculated from the electron velocity.

$$\varepsilon_{tot} = \Sigma \frac{1}{2} m v_L^2 \tag{2.77}$$

Averaging over the laser period τ yields an estimate of the absorbed laser power P_a:

$$P_a \approx \frac{1}{\tau} \Sigma \frac{1}{2} m v_L^2 \tag{2.78}$$

$$P_a = \frac{eE^3}{16\pi^2 m\omega} \tag{2.79}$$

This can then be compared with the time-averaged power of the laser pulse over one cycle:

$$P_L = \frac{cE_L^2 \cos\theta}{8\pi} \tag{2.80}$$

Taking the ratio of the absorbed laser power over the total laser power shows the efficiency of the vacuum heating mechanism to be

$$\frac{P_a}{P_L} = \frac{4a_0}{\pi} \frac{\sin^3\theta}{\cos\theta} \tag{2.81}$$

For laser irradiances of 10^{16} W/cm^2 μm^2 incident on a plasma with density gradients of $L/\lambda \sim 1$, the plasma can absorb 70% of the laser pulse [29]. However, for higher intensities with a short scale length, J×B heating takes over, as described in the following section.

J×B heating

J×B heating is the dominant mechanism of absorption for the interaction of relativistic laser pulses with solid-density plasmas. Hence, it is the primary absorption mechanism responsible for laser-ion acceleration from foils, which necessitates a steep density gradient. The laser pulse must be relativistic because the B-field component of the EM wave must play a significant role in driving the electrons forward into the target. The dephasing of the electrons from the laser pulse

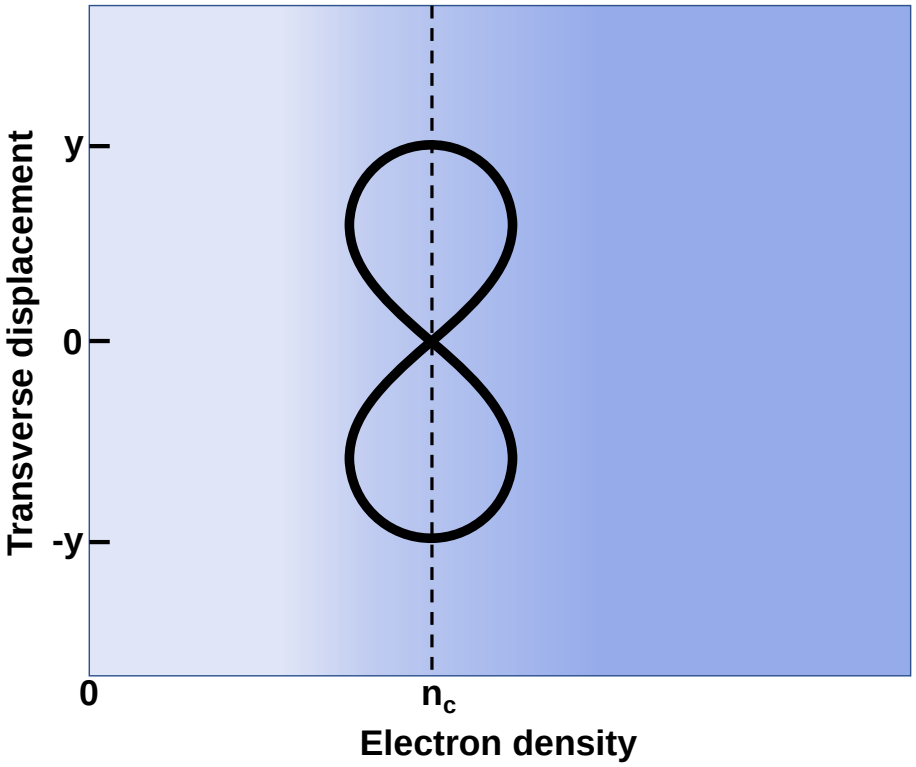

Figure 2.3: An illustration of the J×B heating mechanism. A plasma gradient going from 0 out to solid density represents the front surface of a plasma slab. The critical surface allows for the dephasing of the electrons in a figure-8 trajectory from the laser pulse. The amplitude of the electron's transverse oscillations are represented along the vertical axis.

by the critical surface allows for the energy transfer to occur. The electron is accelerated by the time-dependent ponderomotive force:

$$\mathbf{F}_{pond} = \frac{1}{4} mc^2 \nabla (a_0^2)[1 - cos(2\omega t)] \tag{2.82}$$

The cosine term has an argument of $2\omega t$, meaning that twice every laser cycle, electrons are driven forward. If this forward acceleration happens across the critical surface, the forward-accelerated electrons can escape the laser pulse and continue. A cartoon of this heating mechanism is shown in Figure 2.3.

2.2 Laser-ion acceleration

Short pulse lasers can generate energetic (MeV), picosecond bursts of radiation when incident on solid targets. This radiation can be in the form of electrons, positrons, neutrons, x- and γ-rays, and ions. These sources are of tremendous interest to the ICF community, as both a probe and ignitor for fusion processes, as well as the broader plasma and accelerator physics communities. Typically, these multi-species radiation sources are driven by a high-intensity (>10^{18} W/cm^2) laser pulse incident on a solid foil. Due to the relatively high mobility of the electrons, they are the primary absorber of the laser energy. After the laser couples its energy into the electrons, the electrons can then transfer their energy to generate a variety of sources, including ions, the focus of this work.

The mechanisms of laser-ion acceleration can be broadly classified into three different categories: (i) Coulomb explosion, (ii) surface acceleration, namely target normal sheath acceleration (TNSA), and (iii) volumetric acceleration. Coulomb explosion requires extremely thin (1–10 nm scale) targets or clusters because in order to activate this acceleration mechanism, the laser must fully strip the electrons in the laser spot. Once all the electrons are evacuated from this highly localized area, the ions left behind are mutually repelled by their own space charge field, gaining kinetic energy [30, 31].

On the other hand, for thick, μm-scale targets, surface acceleration dominates. Surface acceleration is best described by the TNSA model, where the laser drives hot electrons through the target. These electrons create an electrostatic sheath field on the rear target surface, which scales as $eE_{sheath} \sim T_{hot}/\lambda_D$, where T_{hot} is the hot electron temperature, and λ_D is the Debye sheath [12]. Although this mechanism is the most commonly observed in experiments, TNSA is not the most efficient acceleration mechanism for ions heavier than carbon ($Z > 6$) [32], unless accompanied by enhancement of other laser-plasma processes. The maximum ion energy produced via this mechanism generally scales as $E_{max} \propto I^{1/2}$ [33, 34], or $E_{max} \propto I$ for ultrashort, tens of fs pulses

[35].

There are several other newly discovered mechanisms that lie between these two extremes, in which the target is volumetrically accelerated. These acceleration mechanisms lead to more favorable scaling of ion energies with laser intensity due to more efficient energy coupling, as well as engaging with a larger volume of the target [33]. These mechanisms include breakout afterburner [4], relativistic transparency acceleration [36], magnetic vortex acceleration [37], radiation pressure acceleration [13], and shock acceleration [38]. We briefly describe a few mechanisms below.

In the relativistically induced transparency (RIT) regime, the relativistic plasma frequency drops due to its inverse dependence on the relativistic γ factor, as $\omega_p^2 = \frac{4\pi ne^2}{\gamma m_e}$. Therefore, the critical density is effectively lowered, allowing the laser to propagate through the plasma. RIT can produce more hot electrons and strengthen the sheath field of TNSA [39, 40], or give rise to additional mechanisms, such as breakout afterburner (BOA). A near-ps laser can trigger this mechanism, in which the onset of RIT allows for the hot electron population to transfer energy to the ions via the relativistic Buneman instability [41, 42]. This co-moving electrostatic potential can accelerate carbon ions to near-GeV energies [4, 43], as the maximum ion energy E_{max} scales linearly with intensity [44].

Radiation pressure acceleration (RPA) can also accelerate the target bulk for intermediate foil thicknesses (10s – 100s of nm), but requires a shorter laser pulse than BOA. A laser of intensity 3×10^{20} W/cm^2, incident on an ultra-thin, high-Z foil will transition from BOA to RPA at the $\approx$360 fs pulse duration [45]. The RPA mechanism requires a short pulse because the target must remain intact for the radiation pressure to drive the target bulk like a laser-piston [13]. Depending on the thickness of the target, RPA can manifest itself as one of two modes. Hole-boring RPA occurs when a laser interacts with a target much thicker than the skin depth, ponderomotively boring a hole in the front surface. It only affects the rear surface if the target is thin enough for the hole-boring front to break through [46]. For target thicknesses on the order

of the skin depth, light-sail RPA can accelerate the ultrathin target bulk as a single slab [47, 48]. For this acceleration mechanism, E_{max} exhibits an even stronger intensity scaling of $E_{max} \propto I^2$ for intensities on the order of $10^{20} - 10^{21}$ W/cm^2, which is typical in most short-pulse laboratory settings.

Sub-picosecond lasers can also generate fast ions via shock wave acceleration (SWA) [49]. A laser pulse, which typically has an intensity profile that is Gaussian in time, can produce ions of different velocities as the intensity profile increases on the target foil. When two plasma populations of a relative drift velocity interact, an electrostatic shock can form, accelerating ions within the target bulk [5]. The cutoff energy for this mechanism scales as $E_{max} \propto I$ for intense laser pulses [49].

For the laser and target parameters studied by the author (detailed in Chapter 3), TNSA is the dominant mechanism of ion acceleration. However, contributions of RPA and SWA are not to be neglected; therefore, it is important that the interplay of mechanisms are clear to the reader. With that, the following sections will describe the analytical models of laser-ion acceleration for TNSA, RPA, and SWA.

2.2.1 Target normal sheath acceleration (TNSA)

For driving ions via the aforementioned TNSA mechanism, the hot electron temperature can be estimated by the ponderomotive potential U_p [12], as

$$T_{hot} \approx mc^2 \left(1 + \frac{2U_p}{mc^2}\right)^{1/2} \tag{2.83}$$

where the ponderomotive potential is, in practical units [50]:

$$U_p[\text{eV}] = 9.33 \times 10^{-14} I[\text{W/cm}^2](\lambda[\mu\text{m}])^2 \tag{2.84}$$

The sheath field is often well above TV/m, which can readily ionize and accelerate

hydrocarbon contaminants. Thus, protons are the most favorably accelerated by this mechanism, and mid-to-high-Z ions are not. However, in-situ target cleaning techniques can provide an avenue to stronger heavy-ion acceleration with the robustness of TNSA. Such techniques include Joule heating, cleaning by a second laser or ion gun, or cleaning via the laser pre-pulse [51]. However, since these techniques are not straightforward to implement, the majority of TNSA studies focus on energetic proton generation.

Since the earliest experiments over 50 years ago, the source of protons in a laser-solid interaction was debated. Gitomer, et al. [52] surveyed many preliminary experiments up to 1986 to show that protons could be a result of vacuum pump oil and water vapor, and measured up to MeV protons with nanosecond lasers up to 10^{16} W/cm^2. However, given the relatively long timescale of the laser pulse, this process is assumed to be hydrodynamic. However, with relativistic laser pulses lasting tens of fs, protons of tens of MeV have been observed, eliminating the possibility that hydrodynamic expansion is the main driver of such energetic ions. The 2001 explanation of Wilks, et al. finally provided a satisfactory explanation of surface acceleration (TNSA), as illustrated in Figure 2.4.

Now we investigate the expansion of protons into the vacuum, as driven by TNSA. Following Mora's model of isothermal expansion [53], we begin by assuming a Maxwell-Boltzmann distribution of electrons.

$$n_e = n_{e0} e^{e\phi/T_e} \tag{2.85}$$

where ϕ is the electrostatic potential, which satisfies the Poisson equation such that

$$\varepsilon_0 \frac{\partial^2 \phi}{\partial x^2} = e(n_e - Z n_i) \tag{2.86}$$

Integrating for the electric field at $x = 0$ (the target surface):

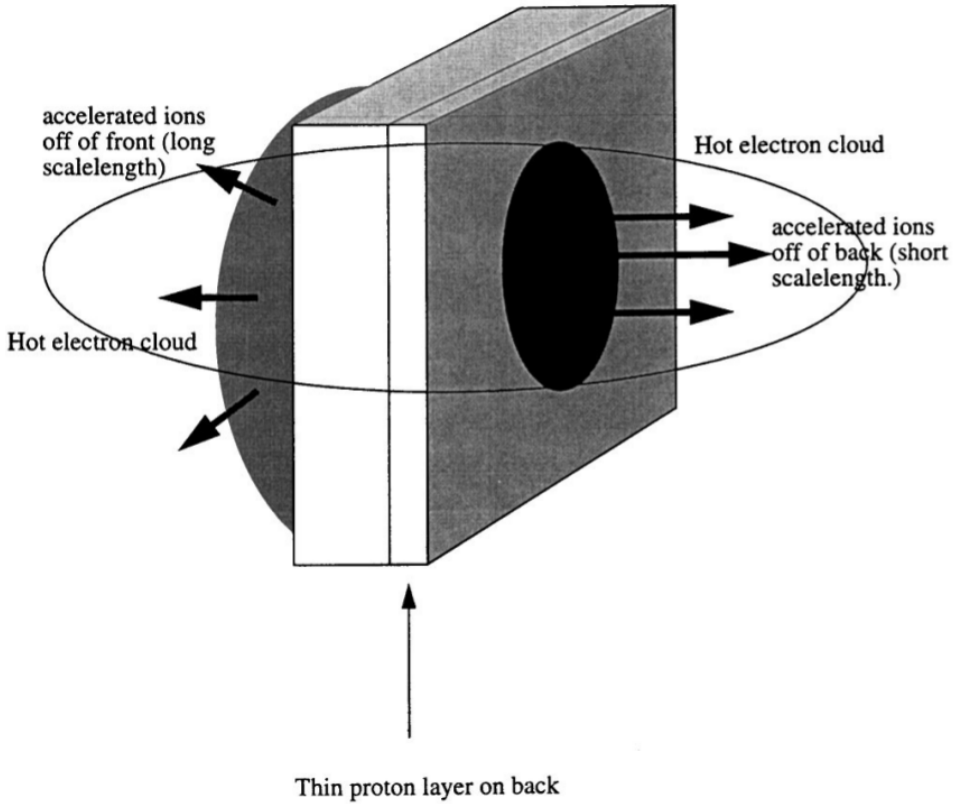

Figure 2.4: Illustration of the target normal sheath acceleration (TNSA) mechanism, showing the source of protons as surface contaminants. Figure courtesy of Ref. [12].

$$E_{front,0} = \sqrt{2/e}E_0 \tag{2.87}$$

$$E_0 = \left(\frac{n_{e0}T_e}{\varepsilon_0}\right)^{1/2} \tag{2.88}$$

During the expansion, the electrons are assumed to stay in equilibrium with the electrostatic potential ϕ. Ion expansion can then be addressed via the continuity equation and equation of motion for ion velocity v_i. The respectively equations are:

$$\left(\frac{\partial}{\partial t} + v_i\frac{\partial}{\partial x}\right)n_i = -n_i\frac{\partial v_i}{\partial x} \tag{2.89}$$

$$\left(\frac{\partial}{\partial t}+v_i\frac{\partial}{\partial x}\right)v_i=-\frac{Ze}{m_i}\frac{\partial\phi}{\partial x} \tag{2.90}$$

There is a self-similar solution for a quasi-neutral plasma, with conditions:

$$n_e=Zn_i=n_{e0}e{-}x/c_st-1 \tag{2.91}$$

$$v_i=c_s+x/t \tag{2.92}$$

where c_s is the ion acoustic speed

$$c_s=\left(\frac{ZT_e}{m_i}\right)^{1/2} \tag{2.93}$$

The self-similar solution E_{ss} then follows to be

$$E_{ss}=\frac{T_e}{ec_st}=\frac{E_0}{\omega_{pi}t} \tag{2.94}$$

which depends on the ion plasma frequency

$$\omega_{pi}=\left(\frac{n_{e0}Ze^2}{m_i\varepsilon_0}\right)^{1/2} \tag{2.95}$$

One requirement of this model is the Debye length must be greater than the self-similar density scale length ($\lambda_D > c_st$). Otherwise, the ions will be shielded from collective motion at this scale, as the local electric fields cannot reach beyond the Debye sphere. This is in qualitative agreement with the above analysis of Wilks, et al. [12].

From the self-similar solution, the ion energy spectra can be obtained. The ion distribution is related to the sound speed as

$$\varepsilon_i = \frac{1}{2} m_i v_i^2 = \frac{1}{2} m_i (c_s + x/t)^2 \tag{2.96}$$

which can be rearranged to show

$$(x/c_s + 1) = \left(\frac{2\varepsilon_i}{ZT_e} \right)^{1/2} \tag{2.97}$$

Assuming a Boltzmann distribution:

$$n_i = n_{i0} \exp \left[- \left(\frac{2\varepsilon_i}{ZT_e} \right)^{1/2} \right] \tag{2.98}$$

The ion distribution with respect to energy can then be found by assuming the plasma expands in space by $c_s t$. The number of ions per surface area, normalized per unit energy is:

$$\frac{dN}{d\varepsilon} = \frac{n_{i0} c_s t}{\sqrt{2\varepsilon_i Z T_e}} \exp \left[- \left(\frac{2\varepsilon_i}{ZT_e} \right)^{1/2} \right] \tag{2.99}$$

To summarize, this model makes several assumptions. Firstly, it assumes a Maxwell-Boltzmann distribution of electrons of a single temperature, which is not always representative of hot electron generation. As such, it shows no dependence on laser parameters, however hot electron generation is a complex topic, and a distribution function of hot electrons cannot yet be analytically estimated from arbitrary laser parameters. Additionally, in this 1-dimensional model, there are no electron losses, which in practice may occur as angular divergence, as well as recirculation into the plasma slab. In addition, the ion acoustic speed is also assumed to be constant and the ions isothermal.

Enhancing TNSA via direct laser acceleration (DLA) of electrons

By improving the transfer of laser energy to electron energy, ion energies and yields via TNSA can be increased. One such avenue is using 3D structures engineered onto the foil

target. These structures can take the forms of channels on the order of the laser spot size, termed "microtubes." Now we investigate analytically, closely following Ref. [54], the role of a pre-formed channel in enhancing electron acceleration. This mechanism is known as direct laser acceleration, or DLA. A channel improves vacuum acceleration of electrons because it introduces a dephasing term given by the ions in the channel. The electrons are readily evacuated from the channel via the ponderomotive force, resulting in a positively charged ion channel. The dephasing rate is given as

$$R = -\frac{1}{\omega}\frac{d\xi}{d\tau} \tag{2.100}$$

where ξ is the normalized phase and τ is the proper time, respectively defined as

$$\xi = \frac{2\pi}{\lambda}(x - ct) \tag{2.101}$$

$$\gamma\frac{d\tau}{dt} = 1 \tag{2.102}$$

where x is the longitudinal position of the electron. Thus the dephasing rate can be rewritten in terms of the longitudinal momentum.

$$R = \gamma - \frac{p_x}{mc} \tag{2.103}$$

The interaction with electrostatic field E^* in the ion channel causes the dephasing rate to evolve as

$$\frac{dR}{d\xi} = \frac{eE^*}{mc} \tag{2.104}$$

As the electron is dragged forward in the ion channel, it spends more time in the laser field, giving it a boost in maximum energy up to $\varepsilon_{max} = \gamma_{max}mc$, where $\gamma_{max} = \gamma_{vac}/R$.

This enhancement in electron acceleration has been observed in both PIC simulation and experiment relative to flat targets. For example, Ji, et al. [55] predicts that with a 40 fs laser pulse of 5.3×10^{21} W/cm^2, maximum electron energies can be doubled. In turn, proton and γ generation are significantly boosted (Figure 2.5). Though PIC simulations are notorious for overestimating the energies and yields of laser-driven radiation sources, nevertheless the author of this PhD thesis observed strong enhancement from the Texas Petawatt Laser for both protons and electrons. In this work, the proton yield was increased by $3\times$, the cutoff energy by 50%, and the electron temperature by 12%. For an in-depth presentation and analysis of these results, see Chapter 5.

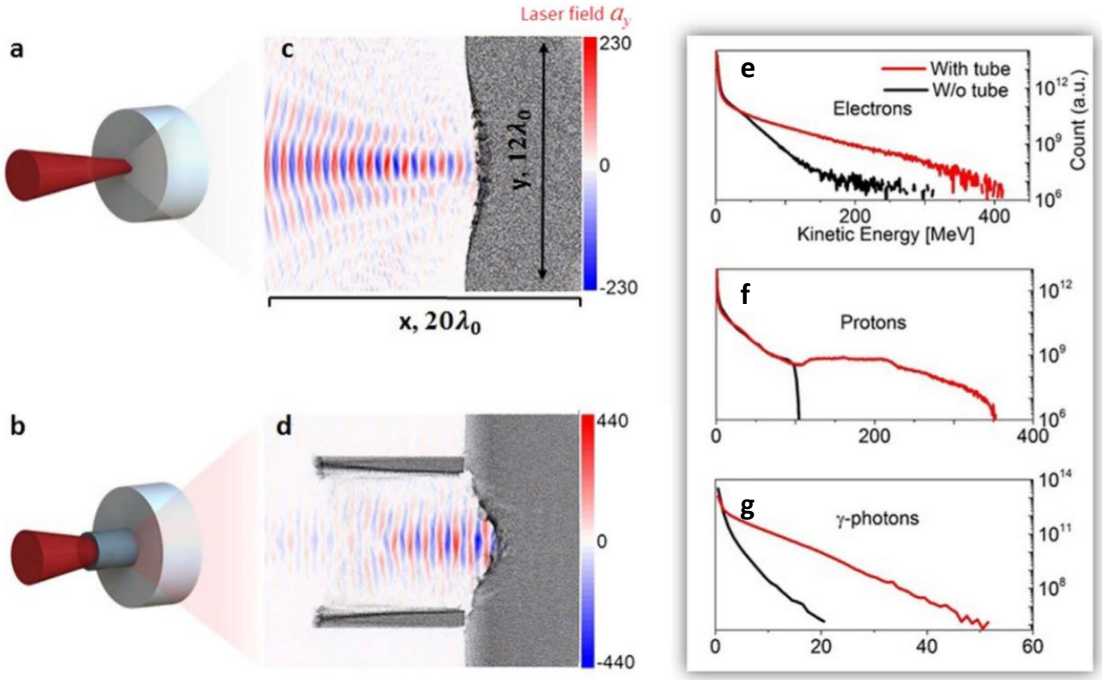

Figure 2.5: Numerical results of source enhancement from flat (a) and microtube (b) CH targets . (c-d) show the respective electric field profiles at 160 fs, and (e-g) show the energy spectra of various particles. Figure modified from Ref. [55].

2.2.2 Radiation pressure acceleration (RPA)

Radiation pressure acceleration, or RPA, uses the reflection of the laser pulse at the critical surface to accelerate ions. To minimize target heating caused by the ponderomotive force (i.e. J$\times$B heating), RPA is most effective when the laser pulse is be circularly polarized. When heating is minimized, the critical surface remains more intact, allowing best reflection of the laser pulse without significant absorption into the target. However, RPA can contribute to the acceleration, though not dominantly, for linearly polarized pulses achievable in the laboratory, of $\sim 10^{20} - 10^{21}$ W/cm^2 (see Chapter 6 for a detailed discussion). RPA is predicted to become significant for linear polarization of intensities $>10^{23}$ W/cm^2, a breakthrough which has just recently been achieved in 2021[24].

As mentioned in the previous discussion of ion acceleration mechanism interplay (Section 2.2), there are two "modes" of RPA. The light-sail (LS) mode requires ultrathin foils, allowing the mass-limited target to sail with the laser pulse. For thicker, μm-scale targets, the hole-boring (HB) mode of RPA takes place. The significant inertia of the target prevents light-sail acceleration, and as such, an ion beam is generated on the front surface of the target and travels inward toward the bulk. This mechanism can either occur in isolation for circular polarization, or, in linear polarization, be used to inject fast ions into a rear sheath field. In the following subsections, we describe each RPA mode analytically.

Light-sail RPA

For the following analysis, we assume a high reflectivity of a laser pulse from a thin foil, closely following Ref. [56]. Since we expect the foil to reach relativistic velocities, we begin with the relativistically correct kinetic energy and momentum.

$$KE = mc^2(\gamma - 1) \tag{2.105}$$

$$p = \gamma mv = \gamma\beta mc \tag{2.106}$$

Under conservation of energy and momentum, respectively:

$$If\Delta t + \frac{mc^2}{\sqrt{1-\beta^2}} = I'f\Delta t + \frac{mc^2}{\sqrt{1-(\beta+\Delta\beta)^2}} \tag{2.107}$$

$$\frac{If}{c^2}c\Delta t + \frac{mv}{\sqrt{1-\beta^2}} = -\frac{I'f}{c^2}c\Delta t + \frac{m(v+\Delta v)}{\sqrt{1-(\beta+\Delta\beta)^2}} \tag{2.108}$$

where I is the incident laser intensity, I' is the reflected laser intensity, f is the cross-sectional area, and Δ represents a small increment. Rewriting as differential equations of motion:

$$I + I' = \frac{mc^2}{f}\frac{d}{dt}\left(\frac{\beta}{\sqrt{1-\beta^2}}\right) \tag{2.109}$$

$$I - I' = \frac{mc^2}{f}\frac{d}{dt}\left(\frac{\beta}{\sqrt{1-\beta^2}}\right) \tag{2.110}$$

Solving for the incident intensity I and the reflected intensity I':

$$I = \frac{mc^2}{2f}\frac{d}{dt}\left(\sqrt{\frac{1+\beta^2}{1-\beta^2}}\right) \tag{2.111}$$

$$I' = -\frac{mc^2}{2f}\frac{d}{dt}\left(\sqrt{\frac{1-\beta^2}{1+\beta^2}}\right) \tag{2.112}$$

For a constant laser intensity, the terminal velocity can be found by integrating over infinite time.

$$\beta = \frac{v}{c} = \frac{(1+2\tau)^2 - 1}{(1+2\tau)^2 + 1} \tag{2.113}$$

where τ is the ratio of the laser energy ε used during time t to the rest energy of the foil.

Mathematically speaking,

$$\tau = \frac{Ift}{mc^2} = \frac{\varepsilon}{mc^2} \tag{2.114}$$

The instantaneous conversion efficiency of the acceleration scheme is found by substituting the terminal velocity (Equation 2.113) into the reflected intensity (Equation 2.112.

$$\frac{I - I'}{I} = 1 - (1 + 2\tau)^{-2} = \frac{d(KE)}{d\varepsilon} \tag{2.115}$$

The total conversion efficiency over the duration of acceleration, up to the terminal velocity is

$$\frac{KE}{\varepsilon} = \frac{1}{1 + 1/2\tau} \tag{2.116}$$

Practically speaking, a relativistic laser pulse must be of a finite duration, and too long a pulse length could allow for target deformation, heating, and eventually destruction of the critical surface. Though it has seen much theoretical and numerical investigation [48, 13, 57], LS-RPA has yet to be fully realized in the laboratory as the dominant mechanism of ion acceleration. This is due to stringent laser requirements, such as a very high contrast and clean pulse, as well as the target requirements, which must be very thin (few-nm) and of high optical flatness to minimize heating. However, signatures of LS-RPA have been identified in experiments, and show that this mechanism enhanced TNSA to achieve the energy record of 97 MeV protons [16].

Hole-boring RPA

Whereas LS-RPA assumes the motion of an intact slab, hole-boring (HB) RPA is akin to the action of a piston into a semi-infinite target. In HB-RPA, the piston is not assumed to interact with the front surface. This interaction would inject HB-RPA ions into a sheath field best described by the TNSA model. For the following analysis, we assume a circularly polarized laser pulse is incident on a semi-infinite slab of hydrogen plasma.

We begin by taking the ratios of reflected intensity to incident intensity (Equations 2.112 and 2.111).

$$\frac{I'}{I} = \frac{1-\beta}{1+\beta} \tag{2.117}$$

Expressing the momentum balance of the plasma surface:

$$\frac{2I}{c}\left(\frac{1-\beta}{1+\beta}\right) = 2(\gamma\beta c)^2 Mn \tag{2.118}$$

where M is the proton mass and n is the ion density. To simplify the expression, the dimensionless parameter $\Xi = \frac{1}{Mnc^3}$ is employed, yielding the quadratic:

$$(\Xi - 1)\beta^2 - 2\Xi\beta + \Xi = 0 \tag{2.119}$$

Taking the root of the quadratic:

$$\beta = \frac{\sqrt{\Xi}}{1+\sqrt{\Xi}} \tag{2.120}$$

The maximum energy of the hole-boring ions can now be calculated. The ions can be reflected from the hole-boring front, meaning they can have up to twice the velocity of βc.

$$\varepsilon_{max} = 2Mc^2 \frac{\Xi}{1+2\sqrt{\Xi}} \tag{2.121}$$

For the sake of consistency with the analysis of LS-RPA in the previous section, the incident laser intensity is fixed. For such a laser pulse of duration t_L, it drives hole-boring for time t_{HB} such that:

$$t_{HB} = \frac{ct_L}{c-\beta c} \tag{2.122}$$

Using the total laser energy expended ε_L, the maximum conversion effiency of the hole-boring acceleration of ions can be calculated. The ratio of energies is most conveniently expressed via the ratio of aerial energy density, though the surface area of the laser pulse and hole-boring ions is assumed the same in this 1D model of acceleration.

$$\frac{KE}{\varepsilon_L} = \frac{\beta c t_{HB} n \varepsilon_{max}}{I t_L} \tag{2.123}$$

The hole-boring velocity (normalized to c), time, and energy, have been defined in terms of Ξ, as seen respectively in Equations 2.120, 2.121, and 2.122. The substitutions eliminate the It_L dependence, yielding a conversion efficiency that depends entirely on the $\Xi = \frac{1}{Mnc^3}$ parameter.

$$\frac{KE}{\varepsilon_L} = \frac{2\sqrt{\Xi}}{1+2\sqrt{\Xi}} \tag{2.124}$$

In the laboratory setting, HB-RPA has seen the most application in driving compact neutron sources. This process is optimized for a circularly polarized laser pulse incident on a thick ($\sim$mm) target. The target is composed of a target material with a high fusion cross-section, such as a deuterated plastic (CD). When the hole-boring deuterons generated on the front surface traverse through the target, they collide with the deuterons of the target bulk, generating neutrons through beam-target fusion. These neutrons, of MeV energies, are spatially and temporally compact like the ion beams that generate them. These have promise for neutron radiography and interrogation of nuclear materials. Example neutron spectra from the T-cubed laser, courtesy of Ref. [58], are shown in Figure 2.6.

2.2.3 Shock wave acceleration (SWA)

A shock is formed when two adjacent plasma slabs have a significant difference in their relative drift velocities. With relativistic laser-plasma interactions, this relative drift can be generated via the hole-boring (HB) mode of RPA. From the reference frame of the shock, there is

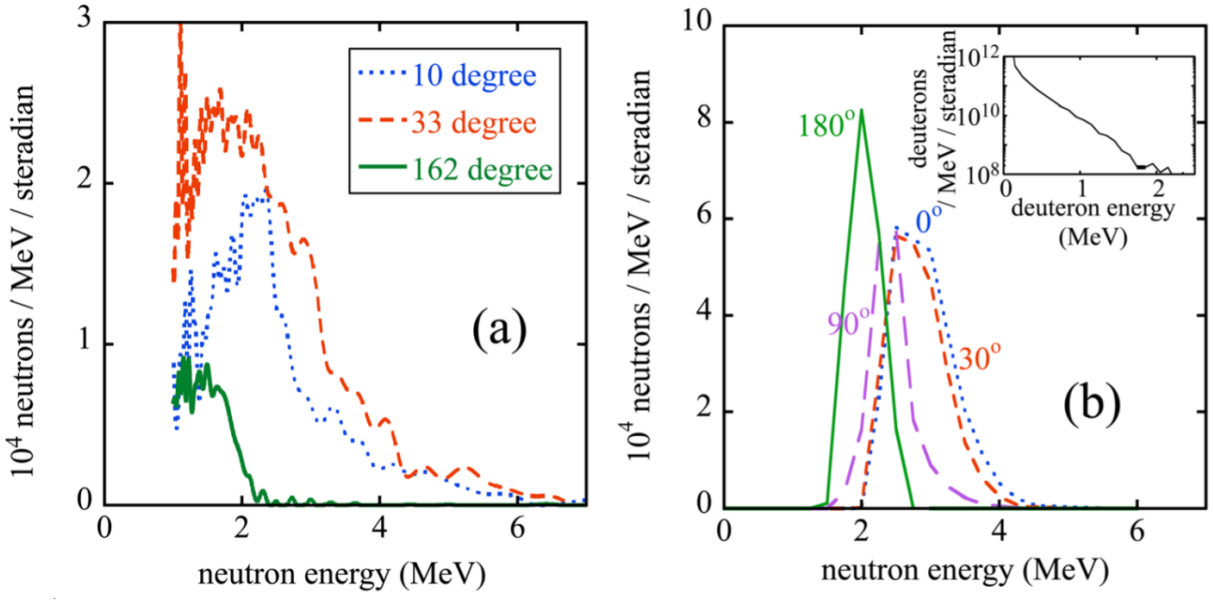

Figure 2.6: Comparison of experimental (a) and numerical (b) neutron spectra from the T-cubed laser incident on 1.5 mm CD. The neutrons are generated via beam-target fusion, in which the deuteron beam was accelerated via HB-RPA. Figure courtesy of Ref. [58].

the convergence of an upstream plasma with a downstream plasma, each with parameters n_{iX}, n_{eX}, and T_{eX}. For the purposes of this analysis and the associated cartoon (Figure 2.7), X=0 and X=1, for the upstream and downstream plasmas, respectively.

In the shock region shown in Figure 2.7, the electrostatic potential increases dramatically from $\phi = 0$ to $\phi = \Delta\phi$. In the lab frame, where the upstream plasma is stationary, the solution to the Vlasov equation is

$$f(x_0, v_{e0}) = \frac{2n_{e0}}{v_{th0}\sqrt{2\pi}} e^{\frac{-(v_0 - v_{sh})^2}{2v_{th0}^2}}. \tag{2.125}$$

The electrons of the upstream plasma, as represented by the density n_{e0}, are streaming into the downstream plasma with velocity v_{sh}. The downstream plasma electrons are assumed to be a flattop Maxwellian [59], with the distribution function

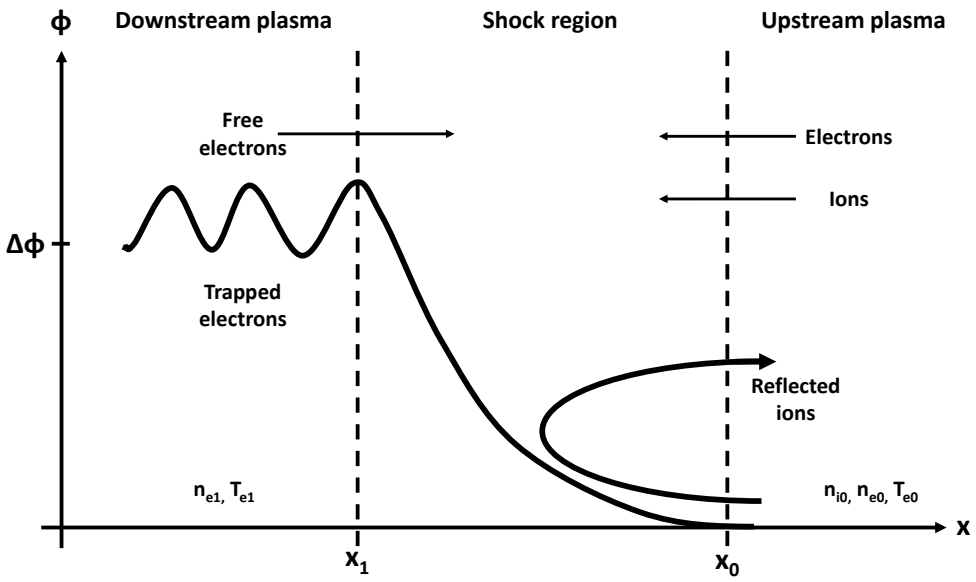

Figure 2.7: Cartoon of shock formation from the reference frame of the shock. Note that the electrostatic potential from the downstream plasma potential can reflect ions from the upstream plasma, accelerating them to up to twice the shock velocity.

$$f(x_1, v_{e1}) = \frac{2n_{e1}}{v_{th1}\sqrt{2\pi}} e^{-\frac{v_1^2}{2v_{th1}^2} + \frac{e\Delta\phi}{k_B T_{e1}}}. \tag{2.126}$$

Respectively integrating Equation 2.125 and Equation 2.126 yields the density of the electrons streaming from upstream to downstream (Equation 2.127) and vice versa (Equation 2.128).

$$n_0' = n_{e0} e^{\varphi} \mathrm{Erfc}(\sqrt{\varphi}) \tag{2.127}$$

$$n_1' = n_{e0}\Gamma e^{\varphi/\Theta} \mathrm{Erfc}(\sqrt{\varphi/\Theta} + \frac{4}{\sqrt{\pi}} n_{e0}\Gamma\sqrt{\varphi/\Theta}) \tag{2.128}$$

In this set of equations, $\varphi = \frac{e\phi}{k_B T_{e0}}$, $\Theta = T_{e1}/T_{e0}$, $\Gamma = n_{e1}/n_{e0}$, and Erfc() is the comple-

mentary error function. To find the complete electrostatic potential, the ion density must first be determined before Poisson's equation can be applied. From the conservation of mass and energy,

$$n_i = n_{i0}/\sqrt{1-2\varphi/M^2} \tag{2.129}$$

where Mach number $M = v_{sh}/c_{s0}$, for upstream sound speed $c_{s0} = \sqrt{k_B T_{e0}/m_i}$. Assuming quasineutrality $n_e 0 = n_{i0} = n_0$, Poisson's equation (Equation 2.130) can then be solved. The solution comprises of three terms [49], with the ion pressure term (Equation 2.131) being of greatest interest to us here. Ion reflection from the shock front will occur when the electrostatic potential across the shock exceeds the kinetic energy of the upstream ions, which can be written as the inequality $e\phi > \frac{1}{2} m_i v_{sh}^2$.

$$\frac{1}{2}\lambda_D^2 \left(\frac{\partial \varphi}{\partial x}\right) + \Psi(\varphi) = 0 \tag{2.130}$$

$$P_i(\varphi, M) = M^2(1 - \sqrt{1-2\varphi/M^2}) \tag{2.131}$$

Solving for φ in this condition leads to the so-called critical value of the shock, namely $\varphi_{cr} = M_{cr}^2/2$. Due to the complex dependence of M_{cr}, it must be solved numerically, as a function of Θ and Γ [49]. However, for the limiting cases of low Mach number shocks, ion reflection will occur for a steep density and low temperature gradients, implied by $\Gamma >> 1$ and $\Theta \sim 1$. For a simple case, one can assume the upstream ions to be initially at rest, and uniform electric field $E_{sh} = \phi/\lambda_D$ driven by the shock. The reflection time τ of the ions in the shock regions is on the order of

$$\tau \sim m_i v_{sh} \lambda_D/(e\phi) \tag{2.132}$$

Assuming a Mach number of order M_{cr}, $e\phi = \frac{1}{2} m_i v_{sh}^2$; therefore the reflection time depends on

the Mach number, as $\tau \sim 2M_{sh}/\omega_{p,i}$

Though shock waves from laser-matter interactions are a complex process and difficult to describe analytically, it is clear that laser-plasmas can meet the required shock conditions. There is strong experimental evidence of the shock wave acceleration (SWA) of ions from relativistic laser pulses [60, 61, 62]. With the shock conditions satisfied, an approximately uniform electric field forms, allowing a relativistic laser pulse can drive quasi-monoenergetic ions.

Chapter 3

Experimental and numerical methods

3.1 The Texas Petawatt (TPW) laser system

The Texas Petawatt (TPW) laser is an Nd:glass laser capable of operating up to 120 J and 140 fs at best compression, easily reaching intensities in excess of 10^{21} W/cm^2 after final focus. With a tightly focused laser spot of $\sim$5 μm, this laser is ideal for studying relativistic laser-solid interactions across a broad parameter space, such as with scanning laser energy and pulse duration. The laser begins as a seed pulse from a Ti:sapphire oscillator, with a 100 fs pulse duration, 16 nm FWHM spot size, and wavelength of 1058 nm. After passing through a stretcher, the 270 pJ seed pulse is injected into the optical parametric chirped pulse amplification (OPCPA) stages. The first two stages are composed of commercial 10 Hz Nd:YAG lasers, operating with 1 J of energy at 532 nm for an 8 ns pulse length. After propagating through beta-barium borate (BBO) crystals for a wavefront correction, a third OPCPA stage is reached. This stage is a 2.5 Hz laser of the same wavelength, with 4 J and a 4 ns pulse length. The laser pulse, now at 1 J, is ready for the rod amplification stage. The rod amplifier stage is composed of Nd:glass with a radial group delay lens to compensate for the mismatch between the phase and group velocities. The laser is then output at 18 J, with a peak fluence of 1.5 J/cm^2 to limit damage to the optics

[63, 64].

The laser pulse then passes through the disk amplifiers, reaching >200 J. This stage is a primary limiter of the laser's hourly repetition rate, as the disk amplifiers are air-cooled. Entering the compressor, the laser pulse sees a series of dielectric gratings with a total conversion efficiency of 85% [63]. At best compression, the laser pulse duration is 140 fs, with a corresponding peak power of approximately 1 PW. As it is important for many experiments, the laser is of moderately high contrast, with of 5×10^8 beyond 100 ps [65]. To reach this contrast, the laser was largely refurbished in 2015 with off-axis parabola (OAP) mirrors replacing all large lenses beyond the OPCPA stages [66], as they are a source of internal reflections and thus pre-pulses. The contrast of the laser system was measured on Thursday March 4, 2021, shortly before the start of the author's campaign the following Monday. This measurement is plotted in Figure 3.1.

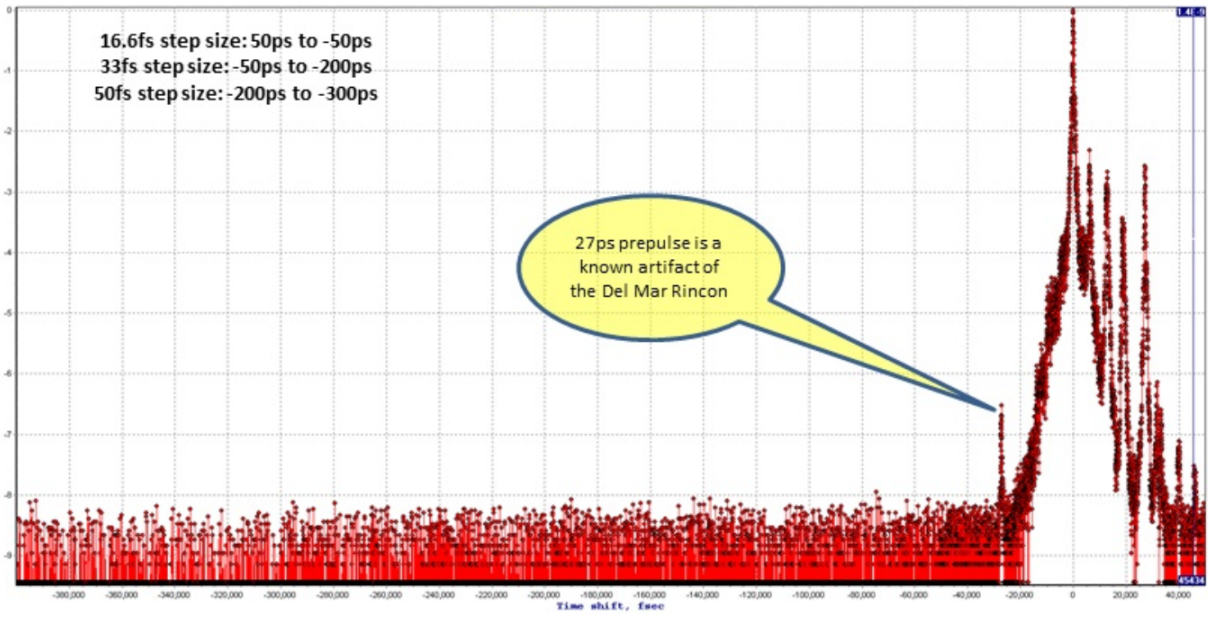

Figure 3.1: Contrast measurement of TPW shortly before the author's campaign. The contrast beyond 100 ps is 5×10^8. Figure courtesy of Ref. [64].

The TPW laser can be directed into two target areas: Target Chamber 1 (TC1) and Target Chamber 2 (TC2). The geometry of TC1 is conducive to high-intensity solid target shots, as either an f/3 or f/1.1 OAP is available for the final focus. Each OAP can produce a respective

peak intensity of 2×10^{21} and 2×10^{22} W/cm^2 [65]. Due to the higher intensities available, TC1 was chosen for the work of the author.

TC2 has a fixed focusing geometry with an f/40 OAP, yielding a FWHM spot size of 60 µm. Due to the long interaction region, the target area is ideal for studying processes such as laser-wakefield acceleration (LWFA), high-harmonic generation (HHG), cluster fusion, and magnetized shocks, albeit with a lower intensity of 10^{18} W/cm^2 [65, 67]. A diagram of the entire facility, identifying the location of each Target Area, is shown in Figure 3.2.

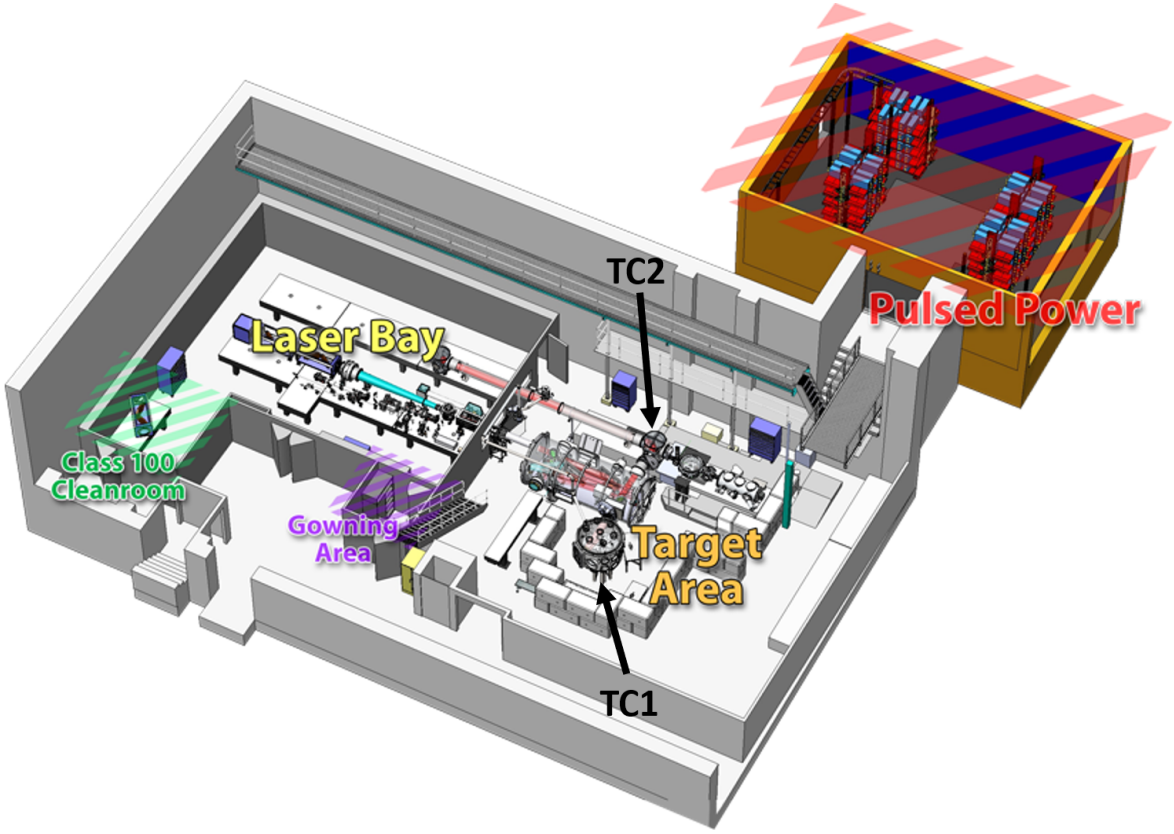

Figure 3.2: 3D rendering of the TPW facility. Note the concrete radiation shield around TC1, where the work of the author was conducted. Figure modified from Ref. [64].

3.1.1 Plasma mirror (PM) contrast enhancement

To enhance the contrast on TPW, there has been a multi-year history of employing plasma mirrors in TC1. A plasma mirror (PM) effectively functions as an ultrafast optical switch. A glass slab with an anti-reflective (AR) coating will largely transmit laser prepulses. However, when the leading edge of the main pulse arrives, the slab is rapidly ionized to densities of order critical. After each PM, $\sim 70\%$ of the laser energy is reflected, with a factor of ~ 100 boost in contrast.

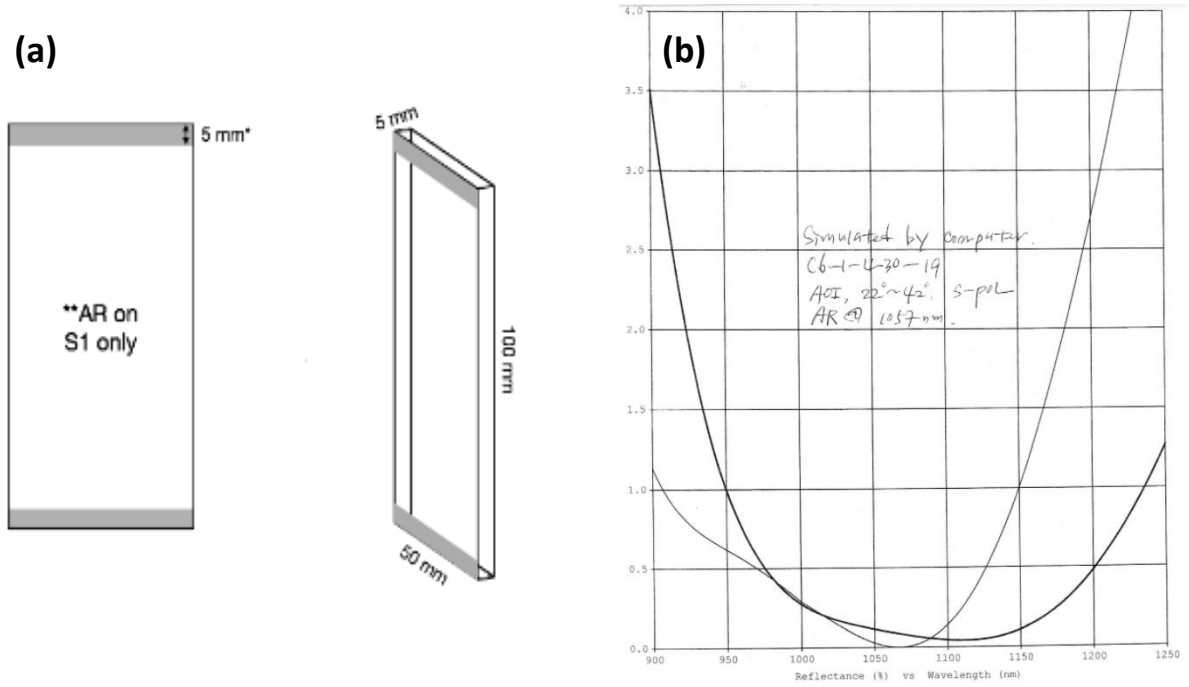

Figure 3.3: (a) Diagram of the plasma mirror fielded on TPW. The laser was inciden on the AR coated side, and 5 mm Al strips on the top and bottom eased alignment. The large surface area of the PM allowed it to withstand 6 shots. (b) Reflectivity curves as a function of wavelength for 22° incidence (bold line) and 42° incidence (not bold).

For the ultrathin (100 nm) targets used in Section 4.2, a double plasma mirror was considered necessary. However, difficulties in alignment led to lower shot rates, prompting the adoption of a single PM for future campaigns. For a recent LaserNetUS campaign, SLAC National Accelerator Laboratory collaborated with the TPW facility to develop a PM capable of reflecting 6 high-intensity shots. The substrate was BK7 glass, with dimensions of 50×100

mm. The large dimensions were chosen so it could be mounted on a translation stage to shorten the turnaround time between shots. The PM was also specifically designed to reflect the main pulse to the TCC (target chamber center) of TC1. As such, it had an AR coating optimized for $32^\circ \pm 10^\circ$. The top and bottom 5 mm were coated with aluminum, as the reflective bands streamline alignment. A diagram of the PM, along with the associated reflectivity vs angle, is displayed in Figure 3.3. Reflectivity measurements were also performed by the facility, showing good agreement with the typical $\sim 70\%$ rule-of-thumb (Figure 3.4).

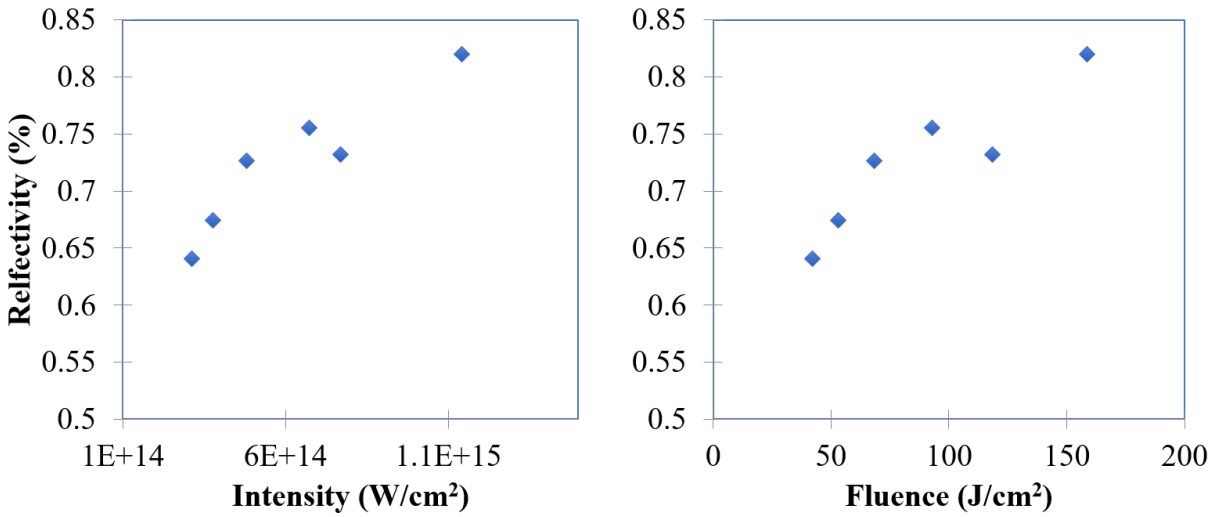

Figure 3.4: Reflectivity measurements conducted at TPW at approximately 30°, as a function of laser intensity and fluence. The PM was moved on a translation stage for the intensity/fluence scan, and reflectivity was calculated with a calorimeter before and after the PM.

3.2 Diagnostics

The charged particle and x-ray spectrometers fielded by the author are described below. The detection media (i.e. imaging plates) used in each diagnostic are described in greater detail in Section 4.1.

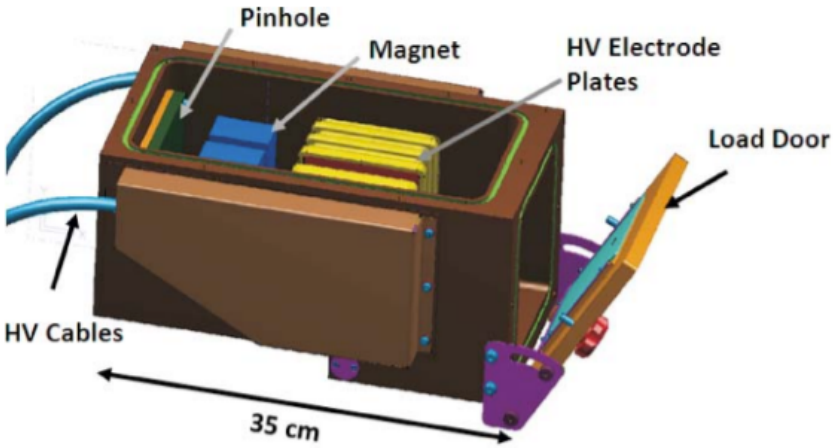

Figure 3.5: CAD model of a typical Thomson Parabola with parallel plates. The load door is for inserting the ion detector, such as an imaging plate. Image courtesy of Ref. [68].

3.2.1 The Thomson Parabola (TP) ion spectrometer

The Thomson Parabola (TP), named after J.J. Thomson, uses a combination of DC electric and magnetic fields to separate charged particles, typically ions, via their charge-to-mass (q/m) ratio and disperse each species in energy. A typical geometry is shown in Figure 3.6, where the ions go through a magnetic field followed by an electric field after being collimated by the pinhole. Simple variations in this design, such as wedge shaped electrodes and overlapping E & B regions have been introduced [69, 70], but for the purposes of deriving an analytical model, the common case of two sets of parallel plates is treated.

Equations of motion in a Thomson parabola

When the particle first enters, it will encounter the magnetic field stage, which drives a gyration via $\mathbf{v}\times\mathbf{B}$ motion, as:

$$x(t) = r_{gyro} sin(\omega_c t) \tag{3.1}$$

where the gyroradius $r_{gyro} = v_0/\omega_c$ and the cyclotron frequency is $\omega_c = qB/m$. The duration of

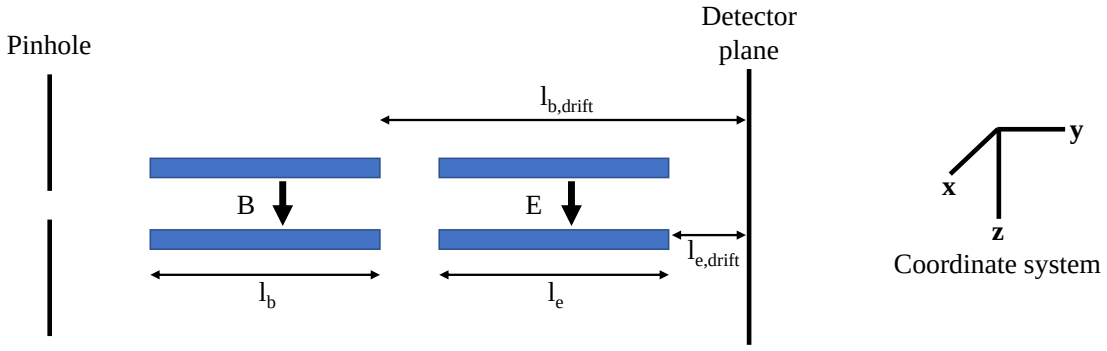

Figure 3.6: Cross-sectional sketch of the TP geometry. This figure defines the coordinate system and dimensions used to determine the ion equations of motion in this section.

gyration occurs for the time the particle takes to traverse the face of the magnet, of length l_b (Equation 3.2). The associated magnetic deflection in the x-direction follows in Equation 3.3

$$t_{gyro} = \frac{1}{\omega_c} arcsin\left(\frac{l_b \omega_c}{v_0}\right) \tag{3.2}$$

$$x_1 = \frac{v_0}{\omega_c}[1 - cos(\omega_c t_{gyro})] = \frac{v_0}{\omega_c}\left[1 - \sqrt{1 - \left(\frac{l_b \omega_c}{v_0}\right)^2}\right] \tag{3.3}$$

In the limit of $\left(\frac{l_b \omega_c}{v_0}\right)^2 << 1$, which is reasonable for MeV ions, one can take the first order of the series expansion:

$$x_1 = \frac{v_0}{\omega_c}\left(\frac{l_b \omega_c}{v_0}\right)^2 \tag{3.4}$$

After passing through the parallel magnetic plates, the final velocities are:

$$v_{x1} = v_0 sin(\omega_c t_{gyro}) = l_b \omega_c \tag{3.5}$$

$$v_{y1} = v_0 sin(\omega_c t_{gyro}) = v_0 \left[1 - \left(\frac{l_b \omega_c}{v_0}\right)^2\right] \tag{3.6}$$

After exiting the B-field, the particle continues to drift freely. The time drifting in the y-direction (Equation 3.7) and amount of x-deflection can then be calculated between the B-field and E-field (Equation 3.8). The latter equation can be added to Equation 3.4 to get the total drift $x = x_1 + x_2$

$$t_{b,drift} = l_{b_drift}/v_{y1} \tag{3.7}$$

$$x_2 = v_{x1} t_{b,drift} = \frac{l_b l_{b,drift} \omega_c}{v_0} \left[1 + \frac{1}{2}\left(\frac{l_b \omega_c}{v_0}\right)^2\right] \tag{3.8}$$

$$x = x_1 + x_2 = \frac{l_b l_{b,drift} \omega_c}{v_0} \left[1 + \frac{1}{2}\left(\frac{l_b \omega_c}{v_0}\right)^2\right] + \frac{v_0}{\omega_c}\left(\frac{l_b \omega_c}{v_0}\right)^2 \tag{3.9}$$

The deflection from the electric field can be independently calculated before it is added to the B-field deflection. For a uniform E-field of length l_e, a particle will spend t_e passing through the E-field region.

$$t_e = l_e/v_{y1} = \frac{l_e}{v_0}\sqrt{1 - \left(\frac{l_b \omega_c}{v_0}\right)^2} \tag{3.10}$$

Taking the first order series expansion:

$$t_e = \frac{l_e}{v_0}\left[1 + \frac{1}{2}\left(\frac{l_b \omega_c}{v_0}\right)^2\right] \tag{3.11}$$

This corresponds with the deflection distance in z, and the corresponding v_z:

$$z_1 = \frac{qE}{2m} t_e^2 \approx \frac{qE}{2m}\left(\frac{l_e}{v_0}\right)^2 \left[1 + \left(\frac{l_b \omega_c}{v_0}\right)^2\right] \tag{3.12}$$

$$v_{z1} = \frac{qE}{m}t \tag{3.13}$$

After exiting the E-field region, the particle takes time $t_{e,drift}$ to drift freely to the detector.

$$t_{e,drift} = l_{e,drift}/v_{y1} = \frac{l_{e,drift}}{v_0}\left[1 - \left(\frac{l_b\omega_c}{v_0}\right)^2\right]^{-1/2} \tag{3.14}$$

$$t_{e,drift} \approx \frac{l_{e,drift}}{v_0}\left[1 + \frac{1}{2}\left(\frac{l_b\omega_c}{v_0}\right)^2\right] \tag{3.15}$$

The drift in this same region, which occurs in the time $t_{e,drift}$ is:

$$z_2 = v_{z1}t_{e_drift} = \frac{qE}{m}\frac{l_e l_{e,drift}}{v_0^2}\left[1 + \frac{1}{2}\left(\frac{l_b\omega_c}{v_0}\right)^2\right]^2 \tag{3.16}$$

$$z_2 \approx \frac{qE}{m}\frac{l_e l_{e,drift}}{v_0^2}\left[1 + \left(\frac{l_b\omega_c}{v_0}\right)^2\right] \tag{3.17}$$

The total deflection due to the E-field, both inside and out of the E-field region, is:

$$z = z_1 + z_2 = \frac{qEl_e}{mv_0^2}\left[\frac{l_e}{2} + l_{e,drift}\right]\left[1 + \left(\frac{l_b\omega_c}{v_0}\right)^2\right] \tag{3.18}$$

Recall Equation 3.9 to see that the particle deflection due to the B-field is proportional to $x \propto 1/v_0$, with the above equation for E-field deflection, where $z \propto 1/v_0^2$, when neglecting the higher-order terms. Now that it is evident that each ion species will make a distinct trace, parabolic in ion energy, on the detector plane. The parabolic trace is of the form $z = Ax^2$, where

$$A = \frac{m}{q}\frac{2E}{B^2}\frac{l_e}{l_b^2}\frac{l_e/2 + l_{e,drift}}{(l_b/2 + l_{b,drift})^2} \tag{3.19}$$

This form assumes that the vertex of the parabola is conveniently chosen to be the "zero-order spot", where non-deflected x-rays propagate directly to the pinhole. This is equivalent to

the location on the detector where ions of infinite energy would be incident. From this form, it is immediately evident that particles of a high q/m ratio will make a "broader" parabolic trace. Therefore, protons, which are consistently accelerated in laser-foil interactions, will make a discernible trace in the parabola. Heavier ions, which can occupy multiple charge states, will be distributed in energy in a more "narrow" parabola. The analysis procedure of the this diagnostic is summarized in the following subsection.

Extracting ion energy spectra from the TP diagnostic

Once the detector has been digitized (ex: scanned imaging plate), one can employ the TP dispersion derived above to take parabolic lineouts. Either one can write their own script, or, alternatively, use the publicly available code TP-o-matic. During his tenure at Los Alamos National Laboratory, Dr. Daniel Jung developed and generously released this open-source MATLAB code. An example shot from TPW incident on a 1 μm Ag foil was imported into the code (Figure 3.7).

Here, TP-o-matic was set up with the relevant TP parameters, which then create the parabolic trace of the selected ion species. The broad parabolic proton trace has been fitted here, with the smaller traces of Carbon-6+ and Carbon-5+ also evident. The background subtraction tool can be used to create a separate parabolic lineout outside of the trace, which the code automatically subtracts with the "Spectrum" button. The projection corresponding to the line-width and horizontal binning are automatically calculated from the other parameters, but can be manually adjusted if desired. Further details of the end product of TP analysis can be seen in the ion acceleration experiment described in Section 5.

3.2.2 Electron, proton, positron spectrometer (EPPS)

The electron, proton, positron spectrometer (EPPS) is a magnetic spectrometer optimized for detecting electrons and positrons from laser-solid interactions, but can also detect protons

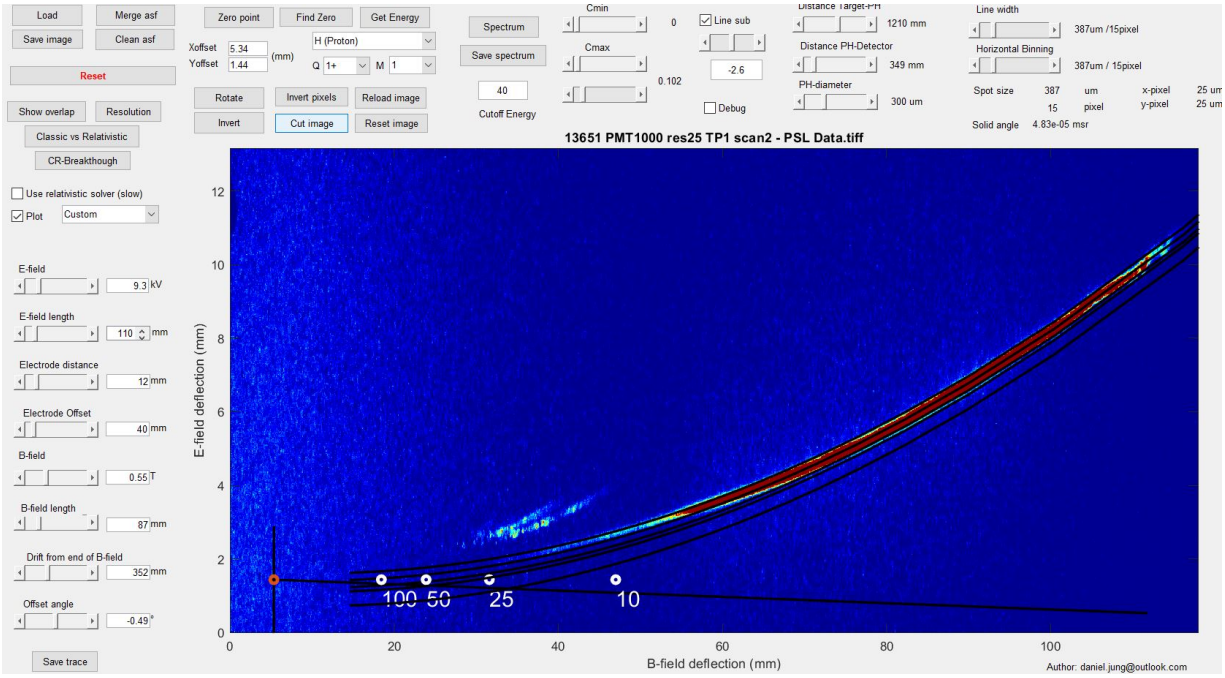

Figure 3.7: Analysis of Thomson Parabola data conducted with the open-source TP-o-matic program. The fit being shown is of a proton trace, with a background subtraction trace slightly below. The ion beam was generated by TPW incident on a 1 μm Ag foil. The interpretation of TP data from this experiment is discussed in detail Section 5.

since they occupy the same deflection plane as electrons. Its design was released by Lawrence Livermore National Laboratory in 2008 [71], with its small footprint making it easy to field in compact geometries. Several versions exist of varying magnetic field strength. On the low end, they are optimized for measuring electrons of 10's – 100's of keV, or on the high end, beyond 100 MeV. Examples of two versions of EPPS, compared with an older scintillator-based spectrometer, are shown in Figure 3.8.

The EPPS has two terminals in which an IP can be inserted, one for positive particles, and one for negative particles. Once the IP is digitized, a lineout can be taken along the IP, and then the neighboring background can be subtracted by an identical lineout. Thus, a plot of signal vs IP position can be generated, as shown in Figure 3.9. After taking this lineout, the position axis can be converted to energy via a proprietary calibration, and the PSL axis can be converted to absolute counts via a peer-reviewed calibration, such as that of Ref. [72]. As the EPPS is of a

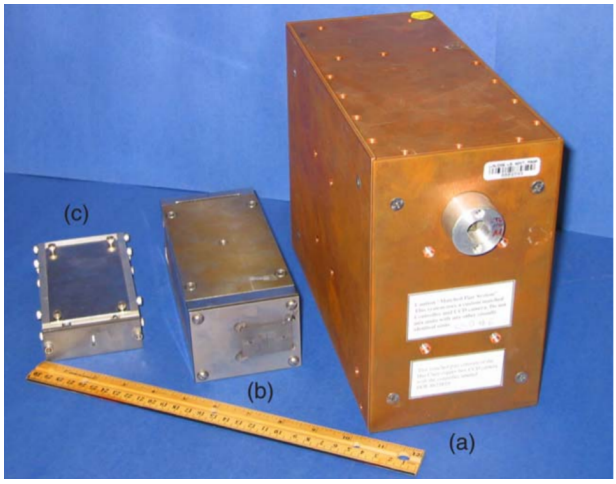

Figure 3.8: Comparison of three electron spectrometers developed at LLNL. The scintillator-based spectrometer (a) is significantly larger than the high-field (b) and low-field (c) magnetic spectrometers. Image courtesy of Ref. [71].

proprietary design, cross-sectional diagrams and detailed magnetic field measurements are not available for public release.

3.2.3 Dual-Channel Highly Ordered Pyrolitic Graphite (DCHOPG) x-ray spectrometer

As its name indicates, the DCHOPG spectrometer [73] has two channels, one optimized for measuring Cu K_α ($\sim$8 keV) in the first diffraction order, and the other for Ag K_α ($\sim$22 keV) in the second diffraction order. The path of the x-rays is as follows. First, they are collimated by the entrance slits, which are covered by a 50 μm aluminized mylar shield for blocking visible light and protecting the delicate crystals from debris. A lead block shields the direct line of sight from TCC as an additional redundancy, as shown in Figure 5.5. The x-rays, now collimated by the slits, reach their respective crystals. Graphite was chosen for the crystal material to optimize the signal-to-noise ratio (SNR), as in this regime, graphite is $\sim 10\times$ more reflective than KAP or PET crystals, and $\sim 3\times$ more reflective than LiF [74]. Each crystal reflects onto imaging plates (IPs) housed parallely in a cassette, that can be removed for IP replacement. The geometry of the

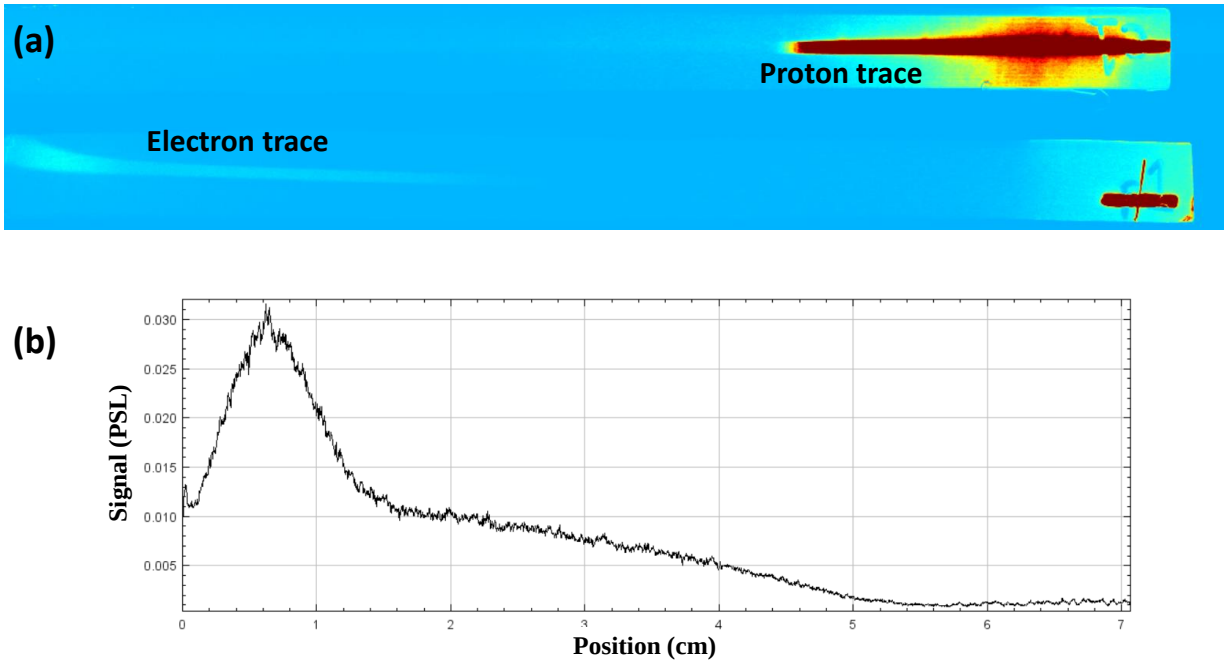

Figure 3.9: (a) False-color image of IPs scanned from high-dispersion EPPS, fielded on TPW incident on a 1 μm Ag foil. (b) Lineout of the electron trace prior to background subtraction. The horizontal axis can be converted to electron energy via a proprietary calibration to construct the energy spectrum.

entire system yields spectral ranges of [7.5, 10.5] keV for the Cu channel, and [19.0, 26.6] keV at the second order for the Ag channel. The entire diagnostic is shielded by thick lead plates (1.27 cm) to further increase the signal-to-noise ratio (SNR). The typical SNR is approximately 200 for the Cu channel, and 1000 for the Ag channel.

The DCHOPG is designed to be placed exactly 14.25 cm away from TCC. To ease alignment, it comes with a so-called "pointer" of this exact length, which is a narrow cone that mounts to the front of the diagnostic. This pointer can then be removed after alignment, and has no role during the actual experiment. After each shot, the IP can then be scanned, generally under the following settings: Latitude = 5, Resolution = 50 μm, Sensitivity = 4000, and Byte = 16. After the image is scanned and digitized, the IP can then be analyzed as follows. The distance H from TCC normal to the crystal is:

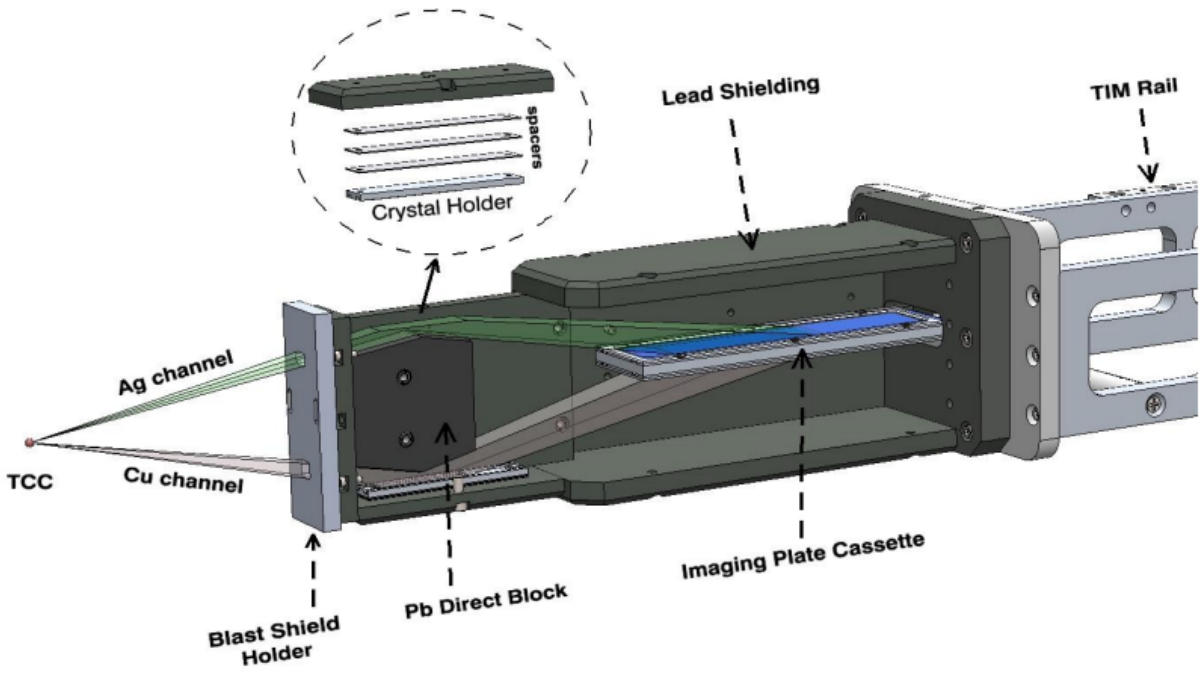

Figure 3.10: 3D rendering of a cutaway of the DCHOPG spectrometer. Image courtesy of Ref. [73].

$$H = \frac{\Delta L_{\alpha\beta}}{2(cot\theta_{\alpha} - cot\theta_{\beta})} \tag{3.20}$$

where $\Delta L_{\alpha\beta}$ is the distance between the K_{α} and the K_{β} lines, and θ is the Bragg angle, defined in practical units as:

$$\theta = arcsin\left(\frac{1240n}{2d_{nm}\varepsilon_{ev}}\right) \tag{3.21}$$

where d_{nm} is the crystal spacing in nm, ε_{eV} is the photon energy in eV, and n is the order of diffraction. The distance from the K_{α} line to TCC along the center (IP) axis is defined as:

$$L_{\alpha} = 2Hcot\theta_{\alpha} \tag{3.22}$$

Converting to energy units:

$$\varepsilon_{eV}(x) = \frac{1240n}{2d_{nm}} \frac{\sqrt{(L_\alpha + x)^2 + 4H^2}}{2H} \tag{3.23}$$

A background continuum can then be fit and subtracted, such as with a higher-order polynomial. Example results are shown from the TPW experiment using the Ag channel, comparing line emission from flat and structured Ag targets (Figure 3.11). In summary, the DCHOPG revealed that structures engineered on the front surface ("3×5" microtubes) reduced target heating, leading to K_α emission at 22.1 keV. Without the structures, the targets were ionized to a He-like state, emitting at 22.7 keV. A more detailed interpretation of these results is discussed in Section 5.

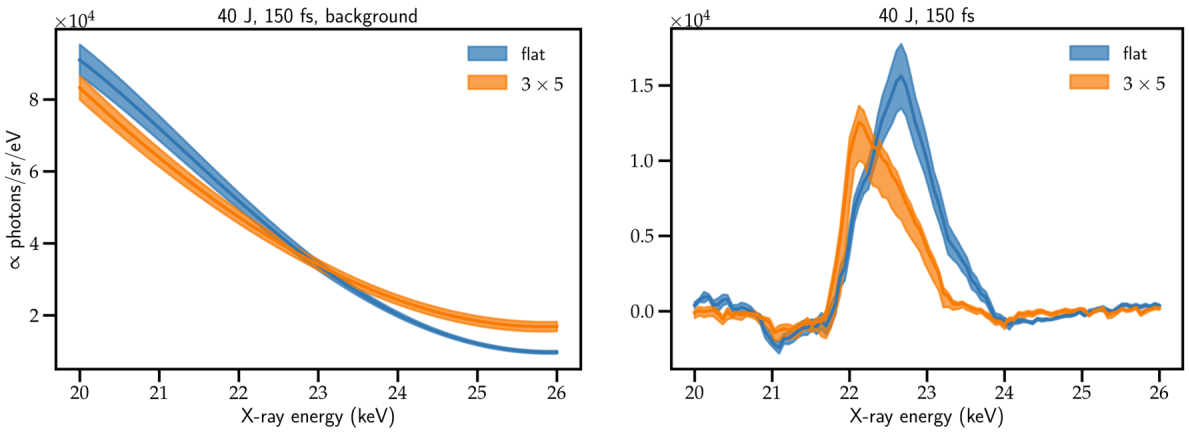

Figure 3.11: Example data from a TPW campaign on flat Ag foils and structured "3x5" targets on a Ag substrate. The left figure shows a polynomial fit to the background continuum, and the right figure shows the cleaned spectra with the background subtracted. The error bands represent the standard deviation among all shots. See Section 5 for a detailed interpretation of these results.

3.3 Advanced target fabrication

Use of structured targets is motivated by improved absorption and conversion efficiency of the laser pulse into secondary radiation. Many such targets have been fabricated in addition to

the microtube targets fielded by the author, such as nanowires [14] and foams [75]. There are many avenues to preparing such targets, including chemical, etching, and additive manufacturing processes. Two common processes in the field are described below, which have both been used to manufacture the author's targets.

3.3.1 Additive manufacturing

Microtubes on Ag foil targets were fabricated via a multistep approach, reliant on the additive manufacturing technology known as 2 photon polymerization (2PP). First, 300 μm thick silicon washers with a 1 mm inner diameter and 3 mm outer diameter were laser machined, then glued to a 1 micron thick Ag foil. Individual washer and foil assemblies were then separated using laser machining for mounting on adhesive Gel-Pak substrates.

The raw materials for 2PP were then prepared by mixing the acrylate monomers, Dipentaerythritol Penta/Hexa Acrylate and Bisphenol A ethoxylate diacrylate, in a 40:60 mass ratio. This ratio was carefully chosen so the index of refraction of the monomer blend matches that of the objective lens of the laser required to drive 2PP [76]. Subsequently, a sensitive 2PP initiator [77] was dissolved at a concentration of 0.2% by mass. This photosensitive monomer mixture was dispensed on top of the foil assembly and placed in a custom 2PP system.

The main components of the system include a Ti:sapphire femtosecond pulsed laser, a high-speed shutter, and an oil immersion objective for focusing the laser, all with a high degree of axial control. The oil immersion objective is immersed directly into the monomer solution, in which the Ag substrate and washer sit at the bottom. Microtubes are fabricated, directly onto the Ag substrate, via laser scanning multiple layers of hexagonally close packed arrays of circles. This process results in a submicron resolution in each cartesian dimension. After the desired structure is complete, the uncured monomer is removed via several rinses in ethanol and then the microtube array is dried in air. After drying, $\sim$20 μm holes were laser-drilled in the Ag foil, above and below the microtube array, to ease alignment. After completion, a sacrifical target can

be imaged via scanning electron microscopy to confirm the target parameters.

3.3.2 Electroplating

Structured targets, such as nanowires, can also be grown via electroplating. An anodic aluminum oxide (AAO) membrane forms the template for growing such wire arrays. AAO is self-organizing on the nanoscale when it is anodized in an acidic environment. By adjusting the pH, anode voltage, and choice of acid, the pore diameter and pore density can be tuned [78]. Since AAO membranes habve commercial application in sensing and filtering, they are readily available off-the-shelf with pore diameters of $10-200$ nm, and porosities of $10-40\%$.

Once the desired AAO membrane has been obtained, a thin chromium film, of order 10 nm, is gently layered onto said membrane. A submicron foil, such as Au or Ni, follows, which becomes the substrate upon which the wires are grown. The foil also forms the electrical contact for the electroplating process. This entire template is then placed in a generic Watts Bath solution, with electrically conductive tape connected to the foil substrate. When a voltage is applied across the foil and solution, the positive ions in the solution diffuse into the bottoms of the pores. As they deposit in the bottoms of the pores, wires the begin to grow, restricted to the pore radius. By terminating the voltage at a calibrated time, the wire length can be controlled. For the purposes of laser-plasma experiments, the wires are generally $\sim$10 μm long.

To free the wire array and substrate from the AAO template, the template must be sacrified and dissolved in a solution of 4M NaOH. After dissolving, the array is dried in a supercritical bath of carbon dioxide, which prevents surface tension of the fluid from warping the wires into bunches. After completion, a sacrifical target can be imaged via scanning electron microscopy to confirm the target parameters.

3.4 The FLASH code

Though now broadly applicable to dense laboratory plasmas, the FLASH code was originally developed to model astrophysical thermonuclear flashes [79]. More specifically, it was built to study the physics of stellar interiors, novae and supernovae, and x- and γ-ray bursts. As an Eulerian code, the mass flows between cells, as opposed to a Vlasov code which tracks phase space evolution, or a PIC code which steps through physical kinetics as constrained by Maxwell's equations (see Section 3.5). Since it is an Eulerian hydrodynamic code, it numerically solves the following conservation equations [80]:

$$\frac{\partial \rho}{\partial t} + \nabla \cdot (\rho \mathbf{u}) = 0 \tag{3.24}$$

$$\frac{\partial}{\partial t}(\rho \mathbf{u}) + \nabla \cdot (\rho \mathbf{u}\mathbf{u} + \mathbf{P}) = \rho \mathbf{g} \tag{3.25}$$

$$\frac{\partial}{\partial t}(\rho E_m) + \nabla \cdot (\rho E_m \mathbf{u} + \mathbf{P} \cdot \mathbf{u}) = \rho \mathbf{g} \cdot \mathbf{u} \tag{3.26}$$

where $\mathbf{u}$ is the velocity, E_m is the energy, ρ is the mass density, and $\mathbf{g}$ is gravitational acceleration. The code also accounts for radiative transfer, relating the energy E to flux $\mathbf{F}$:

$$\frac{\partial E}{\partial t} + \nabla \cdot \mathbf{F} = -c\mu(E - aT^4) - \nabla \cdot (E\mathbf{u}) - \nabla \cdot (p_r \mathbf{u}) - \mathbf{u} \cdot \frac{\mathbf{F}}{c\lambda_{mfp}} \tag{3.27}$$

where μ and a are the radiation coupling terms, T is the temperature, p_r is the pressure, and λ_{mfp} is the mean free path.

The code is computationally efficient not only because it takes advantage of parallel processing, but because of the adaptive mesh refinement technique. This technique means that the resolution can evolve with the simulation, depending on where high resolution is needed, for computational efficiency. Though FLASH is not suitable for explicitly modeling ion acceleration

with sub-ps laser pulses, it can be used to study target evolution before the main pulse arrives. Even after a plasma mirror, the laser pre-pulse cannot be neglected, so FLASH can be used to study the hydrodynamic expansion of a target driven by a laser pre-pulse. As detailed in Chapter 5, this process was essential for determining the optimum laser configuration for a microtube target fabricated according to Section 3.3. Now that the context of FLASH in laser-ion acceleration has been established, details of the FLASH AMR structure are as follows.

3.4.1 Adaptive mesh refinement

Adaptive mesh refinement (AMR) is useful for processes that have micro- and macro-physics that span dramatically different spatial scales. The AMR type in FLASH is known as "block-structured", meaning there are grids and subgrids that can be of arbitrary shape and rotation, and even overlap. Each block as $nxb \times nyb \times nzb$ cells, which can be refined by halving a block along each dimension to create a subgrid. Figure 3.12a shows a single block, which is defined by the user in the initial conditions of the simulation. "Guard cells", required to be four layers thick, surround the spatial boundary to smooth steep gradients, and are filled in via interpolation. These blocks can then be assembled in a set, which covers a fixed domain. The set of parent blocks can split off into daughter blocks, with the same number of cells and a higher resolution to compensate (Figure 3.12b).

Across the boundaries of each cell, all fluxes must be conserved, as summed up through all four boundaries of a given cell. These fluxes then update the cell's local flow variables, allowing the mesh to adapt if necessary. The mesh will not necessarily evolve with each timestep. To compensate for the smaller spatial scale of a finer mesh, the timesteps are proportionately shorter.

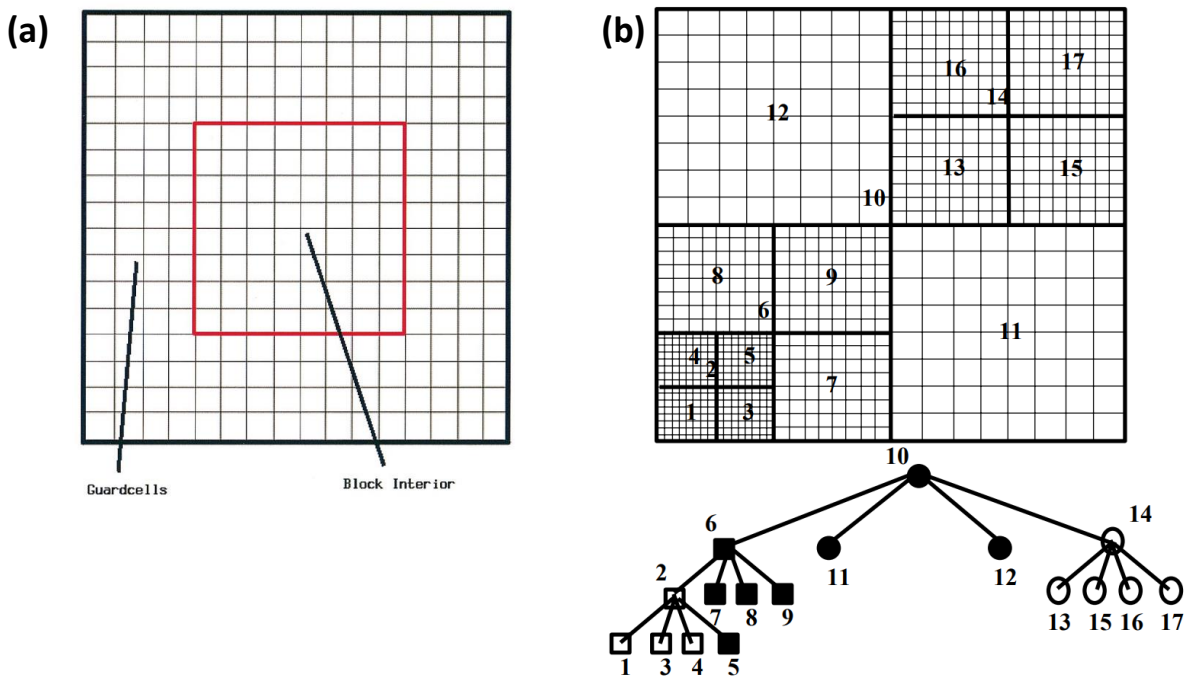

Figure 3.12: (a) A typical block surrounded by guard cells, which are always 4 layers thick to ensure jumps can be interpolated. (b) The organization of parent blocks split into daughter blocks, outlined by the tree below. Figure adapted from Ref. [79].

3.4.2 Radiation hydrodynamic modeling

3.5 Particle-in-cell (PIC) modeling

In certain regimes, particle-in-cell modeling has advantages over other plasma simulation models. The fluid model, for example, describes the macroscopic behavior of the plasma, while the Vlasov model differentiates the phase space to track and evolve the plasma kinetics. Particle-in-cell modeling, on the other hand, is advantageous for the study of nonlinear and non-equilibrium plasmas by coupling Maxwell's equations with the relativistic equations of motion. Due to the computational demands of PIC simulations, macroparticles represent a large collection of electrons or ions. The entire simulation domain is split into a lattice, where the lattice size must be smaller than the characteristic Debye length of the system. In each mesh of the lattice, the electric and magnetic field is calculated numerically to determine the relativistic motion of

the macroparticles. Due to the computational demand of such techniques, PIC simulations are generally limited to a few hundred μm domains, and a few ps in duration. As it pertains to the work of the author, which focuses on high-intensity, sub-ps lasers, PIC modeling is satisfactory to evaluate the physical processes at play.

3.5.1 Basic principles

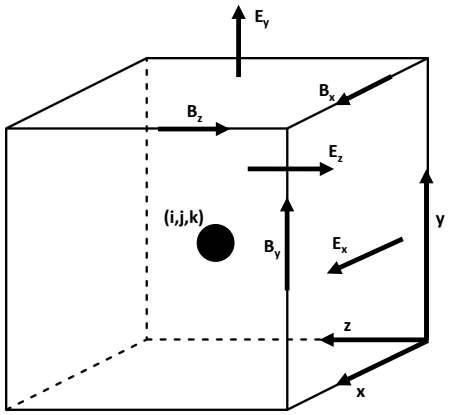

Figure 3.13: A single element of the Yee staggered grid, the Maxwell solver typical of PIC modeling.

Two coupled solvers form the core of PIC modeling: (i) the particle pusher, a solver in which EM fields drive particle motion and then calculates the evolving currents, and (ii) the field solver, which determines Maxwell's equations on the lattice. To solve Maxwell's equations numerically, the finite-difference time-domain (FDTD) method is employed. To do so, the E and B fields are oriented on what is known as a Yee staggered grid [81], as illustrated in Figure 3.13. The grid is staggered to ease the implementation of second order derivatives, such as the local change in E_y along a movement in x:

$$\left(\frac{\partial E_y}{\partial x}\right)_{i,j,k} = \frac{E_{y_{i+1,j,k}} - E_{y_{i,j,k}}}{\Delta x} \tag{3.28}$$

This equation is sufficient up to the second order calculation of $B_{z_{i,j,k}}$. In this example, $\left(\frac{\partial E_y}{\partial x}\right)_{i,j,k}$ updates B_z and ensures $\nabla \cdot B$ is conserved, as required by Maxwell's equations.

As the PIC code advances, first the fields increment by one half of the timestep:

$$\mathbf{E}^{n+\frac{1}{2}} = \mathbf{E}^n + \frac{\Delta t}{2}\left(c^2 \nabla \times \mathbf{B}^n - \frac{\mathbf{J}^n}{\varepsilon_0}\right) \tag{3.29}$$

$$\mathbf{B}^{n+\frac{1}{2}} = \mathbf{B}^n - \frac{\Delta t}{2}\left(\nabla \times \mathbf{E}^{n+\frac{1}{2}}\right) \tag{3.30}$$

The particle pusher (Equation 3.33) then updates the current value, assigning it to the variable $\mathbf{J}^{n+1}$. Consequently, the fields are updated by another half step, from $n+\frac{1}{2}$ to $n+1$. To ensure a realistic solver, it important that the timestep is restricted to $\Delta t < \Delta r/c$ to satisfy the Counrant-Friedrichs-Lewy (CFL) condition, where $r^2 = x^2 + y^2 + z^2$ [82].

$$\mathbf{B}^{n+1} = \mathbf{B}^{n+\frac{1}{2}} - \frac{\Delta t}{2}\left(\nabla \times \mathbf{E}^{n+\frac{1}{2}}\right) \tag{3.31}$$

$$\mathbf{E}^{n+1} = \mathbf{E}^{n+\frac{1}{2}} + \frac{\Delta t}{2}\left(c^2 \nabla \times \mathbf{B}^n - \frac{\mathbf{J}^{n+1}}{\varepsilon_0}\right) \tag{3.32}$$

The solver known as the particle pusher calculates the relativistically correct equation of motion for each particle, as governed by the Lorentz force (Equation 3.33). The particle momentum is, of course, directly related to the velocity as $\mathbf{p}_a = \gamma_a m_a \mathbf{v}_a$, with $\gamma_a = [(\mathbf{p}_a/m_a c)^2 + 1]^{1/2}$. A second order update to the particle position follows (Equation 3.34), and then the process begins again.

$$\mathbf{p}_a^{n+1} + \mathbf{p}_a^n + q_a \Delta t \left(\mathbf{E}^{n+\frac{1}{2}}\mathbf{x}_a^{n+\frac{1}{2}} + \mathbf{v}_a^{n+\frac{1}{2}} \times \mathbf{B}^{n+\frac{1}{2}}\mathbf{x}_a^{n+\frac{1}{2}}\right) \tag{3.33}$$

$$\mathbf{x}_a^{n+\frac{3}{2}} = \mathbf{x}_a^{n+\frac{1}{2}} + \Delta t \mathbf{v}_a^{n+1} \tag{3.34}$$

3.5.2 Atomic processes

When a relativistic (>10^{18} W/cm^2) laser pulse interacts with matter, the matter becomes highly ionized. Following ionization by the laser field, free charged particles can then collide, driving the dynamics behind collisional ionization. Collisional ionization becomes important for heavy (Z > 6) ion accelerations, as light ions (Z $\leq$ 6) are fully ionized by relatively modest lasers of $I = 6.4 \times 10^{18}$ W/cm^2 [83]. This is well below the typical laboratory intensity of today, of $10^{20} - 10^{21}$ W/cm^2. The specific mechanisms for field and collisional ionization, as pertinent to relativistic laser-matter interactions, are detailed below.

Field ionization

When a single atom is irradiated by an electromagnetic field, there is a the probability that the field will assist the electron in tunneling out of the potential well. This is best modeled by the work of Ammosov, Delone, and Krainov [84], and is often referred to by the shorthand "ADK" in the literature. The probability of ionization by the laser field, determined over the irradiation time Δt, is described by

$$R = 1 - e^{-W_F \Delta t} \tag{3.35}$$

where R is the ionization cross-section, and W_F is the tunnel ionization rate. In the limiting cases, it is immediately evident that with very small background electric fields, the probability for electron tunneling is infinitesimal. However, for an infinitely high laser field, the probability saturates to 1. For the ADK model, W_F is defined as

$$W_F = \omega_A C_{n,l}^2 \bar{U} \frac{(2l+1)(l+m)!}{2^m m!(l-m)!} \left(\frac{2\bar{E}_0}{\bar{E}} \right)^{2n^*-m-1} e^{\bar{E}_0/\bar{E}}$$

$$C_{n^*,l^*}^2 = \frac{2^{2*}}{n^*\Gamma(n^*-l^*)\Gamma(n^*+l^*+1)}$$

The atomic frequency is defined as $\omega_A = me^4/\hbar = 4.13 \times 10^{16}$ s^{-1}, the principal quantum number $n^* = Z(2\bar{U})^{-1/2}$, and the Hartree potential is represented by $\bar{U} = U/E_H$, with E_H = 27.4 eV, which is the normalized ionization potential. l is the azimuthal quantum number, and l^* is its effective representation for effective principal n_0^*, defined as $l^* = n_0^* - 1$. Γ is conventional shorthand for the gamma function, defined as $\Gamma = \int_0^\infty x^n e^{-x} dx$. Use of this formula is standard for ionization by relativistic laser fields, as is implemented in a wide variety of PIC simulations, including EPIC [85], EPOCH [86], OSIRIS [87], SMILEI [88], and VLPL [89].

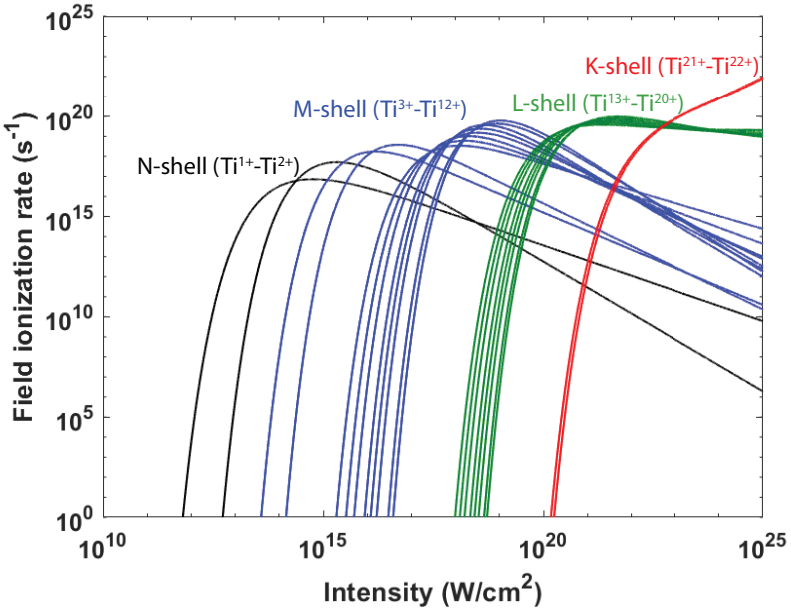

Figure 3.14: Field ionization rate vs laser intensity as predicted by the ADK model. The approximate ionization threshold for a few hundred fs laser is as follows. N-shell: 6.8×10^{12}, M-shell: 2.5×10^{14}, L-shell: 6.0×10^{18}, and K-shell: 1.1×10^{21} W/cm^2.

Figure 3.14 shows the ADK model calculated for titanium, showing field ionization rate as a function of laser intensity. With the typical laboratory lasers of today, ($\sim 10^{20} - 10^{21}$ W/cm^2), it is evident that heavy ions such as titanium will not be fully ionized. Therefore, it is worth investigation of the role of collisional ionization, as it may play a role in the ionization and acceleration dynamics in certain cases.

Collisional ionization

For a mid-Z or high-Z material, the many bound electrons suggest that collisional ionization may not always be negligible in laser-ion acceleration. To most accurately model these phenomena, collisional processes must be implemented in particle-in-cell simulations. Two such methods have been performed in the literature. Firstly, collisional ionization can be accounted for by averaging plasma parameters in each cell. By calculating the cell-averaged electron density, energy, and velocity, the PIC code can calculate the average ionization state of each cell induced by electron impact ionization [45].

Particle pairing is a more comprehensive method, yet it demands approximately double the computational resources required by the simulation. In this method, information is assigned to each particle in the PIC simulation, such as quantum number, atomic potential, and ionization state. As such, three kinds of pairs form per cell via a Monte Carlo calculation: (i) electron-electron, (ii) ion-ion, and (iii) electron-ion. Electron-ion collisions dominate the collisional ionization of ions, as electrons provide a direct energy transfer of laser pulse energy, and thus hold much more kinetic energy. The analytical model for ionization cross-section via the impact of energetic electrons is known as the binary-encounter Bethe (BEB) model (see Ref. [90] for a detailed derivation spanning many pages). The cross-section σ_{BEB} has a highly nonlinear relationship with normalized kinetic energy $t = W/B$, where W is the free electron kinetic energy, and B is the bound energy.

$$\sigma_{BEB} = \frac{4\pi a_B^2 N (R/B)^2}{t + \frac{1}{n(q+1)}} \left[\frac{ln(t)}{2} \left(1 - \frac{1}{t^2} \right) + 1 - \frac{1}{t} - \frac{ln(t)}{t+1} \right] \tag{3.36}$$

The Bohr radius is $a_B = 5.29 \times 10^{-11} m$, the Rydberg energy is $R = 13.6$ eV, N is the number of bound electrons, n is the principal quantum number, and q is the net charge of the ion. The BEB model has been experimentally validated, with an example shown in Figure 3.15 [91]. In this experiment, a small DC accelerator drove an electron beam into an off-axis neutral CH beam, which was directed into a magnetic spectrometer [92]. The spectrometer was thus able to determine the ionization state generated by electrons of a tunable energy, with the model in close agreement within the error bars of the data. Similar studies have extended these comparisons to high-Z atoms [93, 94], with the BEB model demonstrating sufficient validity. In the EPIC code, which has been employed in this dissertation due to its capability to study collisions, the collisional ionization rate is calculated as $W_{ln} = n_e \sigma_{BEB} |v_e| \Delta t_c$. The velocity of the incident electron is defined as v_e , and Δt_c is the mean collision time.

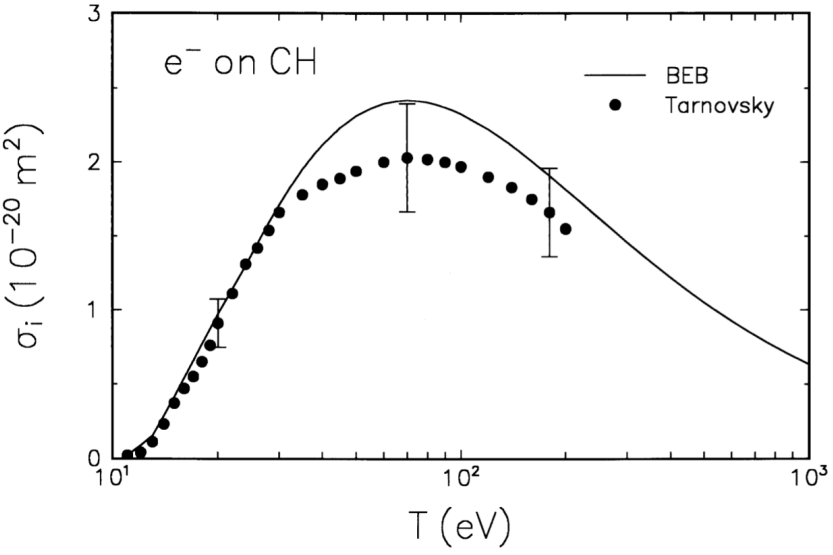

Figure 3.15: A comparison of the analytical BEB model with experimental data, as determined by Tarnovsky, et al. in 1996 [92]. Figure courtesy of Rudd, et al. (1997) [91].

Chapter 4

The calibration of solid-state detectors to energetic ions

4.1 Common ion detectors in short-pulse experiments

A variety of solid-state detectors are available for detecting MeV ions from a laser-plasma interaction, with the choice of detector having various trade-offs. Due to their ease of use and resistance to electromagnetic pulses (EMP), imaging plates (IP) are arguably the most common choice. An IP consists of several layers: (i) an active layer, (ii) a plastic polymer support layer, and (iii) a magnetic layer for attachment to the image plate scanner. On some IP types, there may be an additional layer of mylar to protect the active layer. The compositions of the most common IP configurations are summarized in Table 4.1 [72]. The "TR" type, named for its original purpose of tritium detection, lacks a protective layer that would otherwise stop heavier ions from reaching the active layer. The downside is that the lack of protection enables it to damage easily, so it must be handled with great care. The "MS" type, or "Multipurpose Standard," has the most robust protective layer. The "SR" type, or "Super Resolution," can be used for high-resolution applications, at the tradeoff of increased cost. For the purposes of laser-ion acceleration, either

Table 4.1: The composition of the three most common IP types: TR, MS, and SR. The material properties are split into three tables: chemical composition (above), material density ρ (middle), and layer thickness d (below).

Layer	TR	MS	SR
Protective	None	C_2H_2O	C_2H_2O
Active	$BaFBr_{0.85}I_{0.15}$	$BaFBr_{0.85}I_{0.15}$	BaFBr
Support		C_2H_2O	
Magnetic		$ZnMn_2Fe_5NO_{40}H_{15}C_{10}$	

Layer	ρ_{TR} (g/cm^3)	ρ_{MS} (g/cm^3)	ρ_{SR} (g/cm^3)
Protective	None	1.66	1.27
Active	2.85	3.31	3.10
Support	1.66	1.66	1.27
Magnetic	2.77	2.77	3.10

Layer	d_{TR} (μm)	d_{MS} (μm)	d_{SR} (μm)
Protective	None	9	6
Active	50	115	120
Support	250	190	188
Magnetic	160	160	160

MS or SR types are sufficient for studying light ion acceleration ($Z \leq 6$), while TR is superior for heavy ion acceleration due to the absence of the protective layer.

IPs have a multitude of advantages, including their high dynamic range, on the order of 10^5, allows them to detect a wide range of particle species over a wide range of energies. They are also erasable, and can be re-used for many years if appropriately cared for. After an IP is irradiated, the active layer becomes excited, with energy stored as phosphorescence, with its maximum intensity decaying to 50% over 3 hours. After the IP is scanned (usually after a characteristic time of 30 minutes in the literature), the IP can then be erased by placing it under a bright white light source for tens of minutes.

The scanning procedure digitizes the energy stored as phosphorescence into an image

with pixel units of PSL, or photostimulated luminescence. While scanning, the input software requires an input of 6 parameters, which are important to note for converting from pixel counts to PSL. The function for PSL conversion is as follows:

$$PSL = \left(\frac{Res}{100}\right)^2 \frac{4000}{S} 10^{L(\frac{Q_L}{2^D-1}-\frac{1}{2})}$$

where PSL is the number of luminescent photons in a pixel; Res is the resolution, or pixel size, in μm; S is the scanner sensitivity; L is the latitude; Q_l is the pixel value; and D is the reading dynamic. The choice of input parameters varies with each diagnostic and experimental conditions, and will be explicitly stated for each diagnostic that uses an IP as the detection medium.

Though IP signal can be reported in PSL, to better understand the laser-plasma interaction, it is recommended to calibrate the PSL into particle number. Two common methods of doing such are (i) using a conventional accelerator with tunable charge and energy to excite the active layer [68, 72], or (ii) using a CR-39 track detector. When energetic ions are incident on a layer of CR-39, they break up the chemical bonds and make a permanent track in this detector. This track can then be enlarged by immersing the detector in a strong base, such as NaOH. Such procedures have been successful for the calibration of image plates to many species of ions [95, 96, 97, 98]. CR-39 can be used on its own as an ion diagnostic, yet it is not always feasible to do so due to the significant chemical hazards and the time required to analyze a single shot. The specific procedure for CR-39 analysis, and its ability to calibrate IPs, has been conducted by the author and is detailed in Section 4.2.

Radiochromic film (RCF) is, like CR-39, a single use plastic detector, though it detects the deposited dose via a different mechanism. A film contains an active layer reacts to ionizing radiation via a chemical reaction in the polymer. This effect is visible by eye, with the film blackening for stronger doses. On proton acceleration experiments, the films are assembled in a stack configuration to measure both the energy and spatial distribution of the beam. RCF is not

Table 4.2: The composition of the two types of RCF fielded by the author on experiments: HD-v2 and EBT-3. The material properties are split into three tables: chemical composition (above), material density ρ (middle), and layer thickness d (below).

Layer	HD-v2	EBT-3
Protective	$C_{0.455}H_{0.364}O_{0.181}$	$C_{0.455}H_{0.364}O_{0.181}$
Active	$C_{0.279}H_{0.590}O_{0.117}N_{0.001}Li_{0.006}Cl_{0.006}Na_{0.005}Al_{0.003}$	$C_{0.291}H_{0.568}O_{0.071}N_{0.070}$
Protective	None	$C_{0.455}H_{0.364}O_{0.181}$

Layer	ρ_{HD} (g/cm^3)	ρ_{EBT} (g/cm^3)
Protective	1.35	1.35
Active	1.20	1.08
Protective	None	1.35

Layer	d_{HD} (μm)	d_{EBT} (μm)
Protective	97	120
Active	8	15
Protective	None	120

suitable for measuring the spectra of heavier ions since they are easily stopped by the aluminum foil that typically holds the stack together. In the author's experiments, two types of RCF were fielded: HD-v2 amd EBT-3, henceforth referred to as HD and EBT. It is advantageous to have the first portion of the stack be HD, because it is less sensitive, boasting a dynamic range of 10 – 1000 Gy. EBT, on the other hand, is less sensitive, so it should be placed at the high energy end of the stack. When assembled into a stack, the RCF layers can be separated by metal filters to expand the spectral range of the stack. An example stack, shown in Figure 4.1, can detect protons up to 70.5 MeV, with the help of nickel filters. After the shot, the films can then be scanned for digitization and analyzed for energy and angular distribution.

Although these diagnostics are insensitive to EMPs, their analysis requires a multi-staged digitizing and analysis procedure to characterize a laser-driven ion beam. In addition, cycling the vacuum to replace these diagnostics often takes 30-60 minutes, which limits the shot turnaround

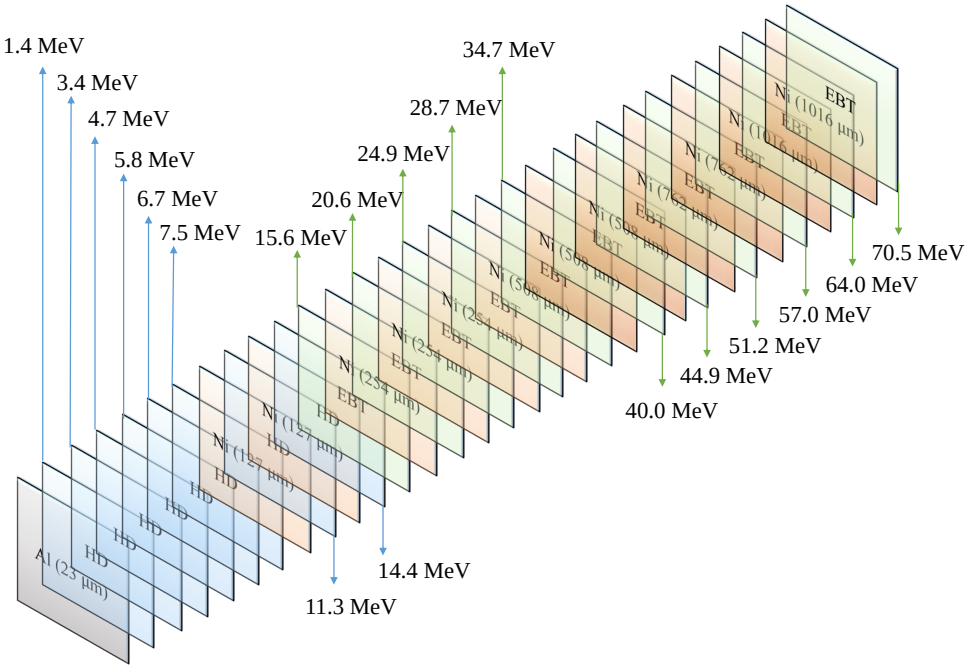

Figure 4.1: Sketch of the RCF stack composition, as fielded on TPW. The stack was wrapped in heavy duty aluminum foil, as represented by the 23 µm filter on the front of the stack. Each layer of RCF is labeled by its breach energy, indicating a spectral range of [1.4, 70.5] MeV.

time as Petawatt lasers grow in repetition rate. Hence, microchannel plates [99] and scintillators [100] have become increasingly popular in short pulse experiments.

4.2 Determining the IP response to heavy ion beams

4.2.1 Experimental setup and methods

The Texas Petawatt Laser system, as described in Section 3.1, was used to create the laser-driven ion source with ultrathin targets. Due to the these sensitive targets, it was necessary to field double plasma mirrors, enhancing the laser contrast from 10^{-9} to 10^{-13} beyond 100 ps. Without this high laser contrast, the prepulse from the laser would destroy the ultrathin 100 nm target. The 1 μm wavelength laser directed 50 J on target, with a FWHM intensity of 5×10^{20} W/cm^2. The calibration was conducted with a Thomson Parabola (TP) ion spectrometer, which

functions as discussed in Section 3.2.1.

Two Thomson parabolas (TP) [69], one along target normal and one 11° off axis, were employed to study rear acceleration mechanisms, and a third measured the front acceleration for this calibration of the imaging plates with CR-39. IP detectors are often calibrated for ions with CR-39 track detectors [95, 97, 98, 101]. When incident on this plastic, energetic ions create a track of broken polymer chains within the bulk. The particle tracks can be etched to tens of microns with a strong base, and then viewed under an optical microscope. Particle track size is a function of etching time, etching solution concentration, and temperature. It is important not to over-etch because the tracks can overlap and become difficult to distinguish [102].

To measure the deposited dose of titanium ions on the IP, a CR-39 track detector with periodic slots was superimposed upon the IP. The detector has slots and spacing of each 1 mm, allowing for a direct comparison of deposited dose to PSL signal from the shadow of the CR-39 (Figure 4.2).

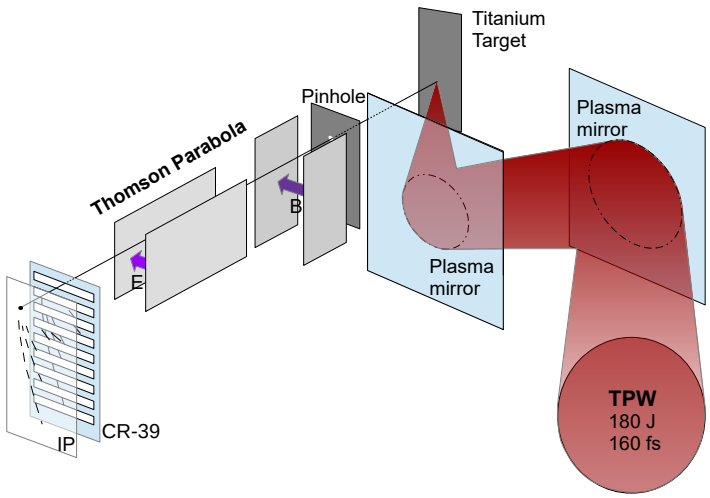

Figure 4.2: Diagram of the experimental setup corresponding to the front Thomson Parabola. Double plasma mirrors enhanced the laser contrast by 10^4. Figure not to scale.

The front TP shown in Figure 4.2 was used for the calibration shot. After the shot, the CR-39 was etched in 6.25M NaOH solution for three hours at 75°C, to get a titanium track diameter of $\sim$17 μm, as observed under an optical microscope at 40x magnification (Figure 4.3).

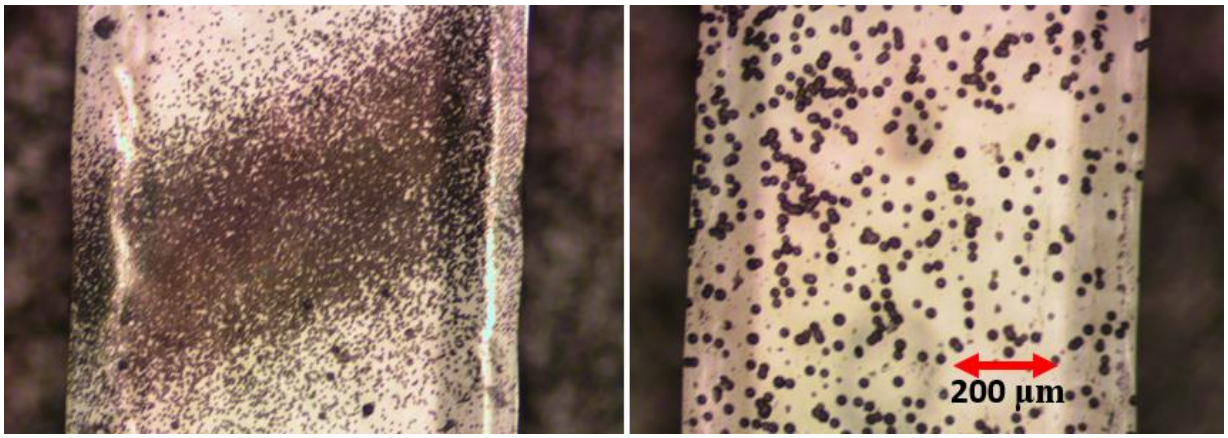

Figure 4.3: Comparison of proton (left) and titanium (right) ion tracks after etching.

Each IP was scanned approximately 30 minutes after each shot, with a General Electric Typhoon FLA 7000 IP scanner. The scanner settings are as follows: 25 μm resolution, Latitude 5, Sensitivity 4000, and PMT 500 Volts. After scanning, the calibration shot IP was analyzed to determine the ion species and their corresponding energy spectra. A linear interpolation was employed to find the average PSL value best corresponding to each slot of CR-39, and this value was matched with the ion number per solid angle. The ions were counted from microscope images following the etching procedure.

The Thomson parabola spectrometer separated the protons, carbons, and titanium ions, creating parabolic traces on the CR-39 and IP stack (Figure 4.2). The titanium ions were counted under a microscope, and corresponded to a PSL value that was calculated from the average PSL on each side of the CR-39 detector. The resulting calibration from this analysis, conducted with Ti^{10+}, Ti^{11+}, and Ti^{12+} (Figure 4.4) displays a charge-independent relationship of PSL_{30}/#Ti-ions vs incident ion energy. Though stopping power is proportional to the square of the charge species, IP response is not charge dependent as long as the same amount of energy is deposited in the

50 μm active layer. This charge independence is expected to hold for all other ionization states of titanium, which is consistent with the BAS-TR IP calibration for energetic carbon ions [95]. Because conducting the calibration requires averaging absolute dose and PSL counts over a fixed area, a small uncertainty arises in the PSL response data. Additionally, some of the etched ion tracks largely overlapped, resulting in a small uncertainty in deposited dose. This same calibration procedure was conducted for 53 MeV carbon ions, deposited on one slot of CR-39, to support the published BAS-TR IP calibration for carbon ions [95]. There is good agreement between the published IP response function for carbon and the datum determined from this analysis, as represented in Figure 4.8.

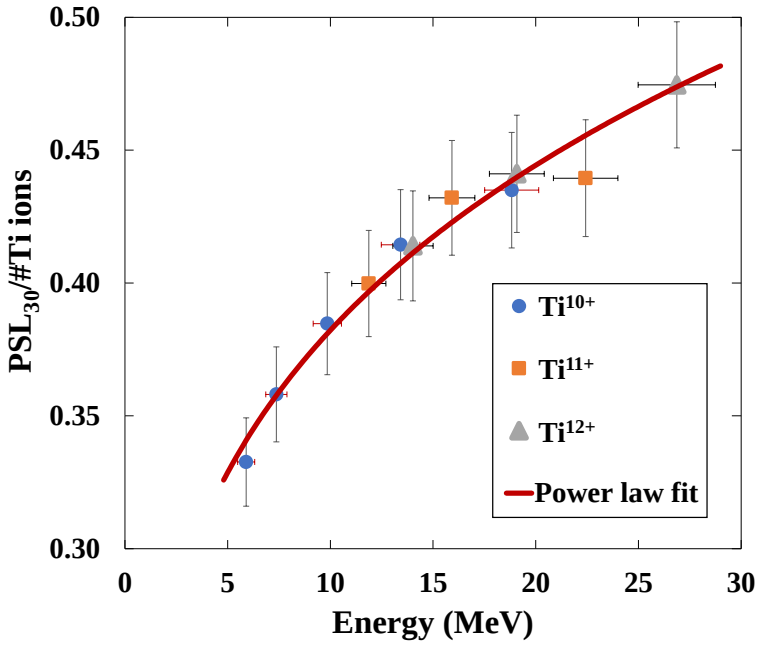

Figure 4.4: IP response to energetic titanium ions. The data are best fit by the power model $PSL_{30}/ion = aE^b$ where E is in MeV. Plotted below is the fit with all three charge species, demonstrating charge independence. The corresponding fit parameters and coefficients of determination are shown in Table 1.

The titanium data demonstrate a power law relationship that is limited to extrapolation for titanium ions between 4.8 and 161 MeV. Figure 4.5 illustrates simulations conducted using

Table 4.3: Titanium calibration curve fit parameters. The fit is of the form $PSL_{30}/ion = aE^b$, where E is in MeV.

Species	a	b	R^2
Ti^{10+}	0.2240	0.2315	0.9815
Ti^{11+}	0.2821	0.1459	0.8488
Ti^{12+}	0.2376	0.2101	0.9999
Combined species	0.2317	0.2174	0.9722

Stopping and Range of Ions in Matter (SRIM) [103], which indicate that 4.8 MeV titanium ions have an average penetration depth of 4.97 μm in the active layer. This depth is just below the grain size of 5 μm. With a penetration depth less than the grain size, the imaging plate response becomes highly statistical [95]. Additionally, SRIM calculations determined that titanium ions exceeding 161 MeV have a high probability of penetrating the 50 μm active layer. A calibrated spectrum, plotted within these limits, is shown in Figure 4.6.

This empirical response function allows for the calculation of the IP sensitivity to titanium ions, in units of PSL/MeV. Hidding's model of IP response to radiation[104] assumes that the response $R(E)$ is proportional to the energy deposited, as

$$R(E) = \alpha E_{dep}(E) \tag{4.1}$$

where α is the sensitivity in PSL per units of energy deposited. This is valid at high energies for low-Z ions when the stopping power is approximately constant. However, a more accurate model (Bonnet's model) accounts for variation in stopping power, as well as the absorption of the PSL photons inside the active layer of the IP:

$$R(E) = \alpha \int_0^T \frac{dE}{dx} exp(-x/L)dx \tag{4.2}$$

where T is the thickness of the active layer, and L is the absorption length of the PSL

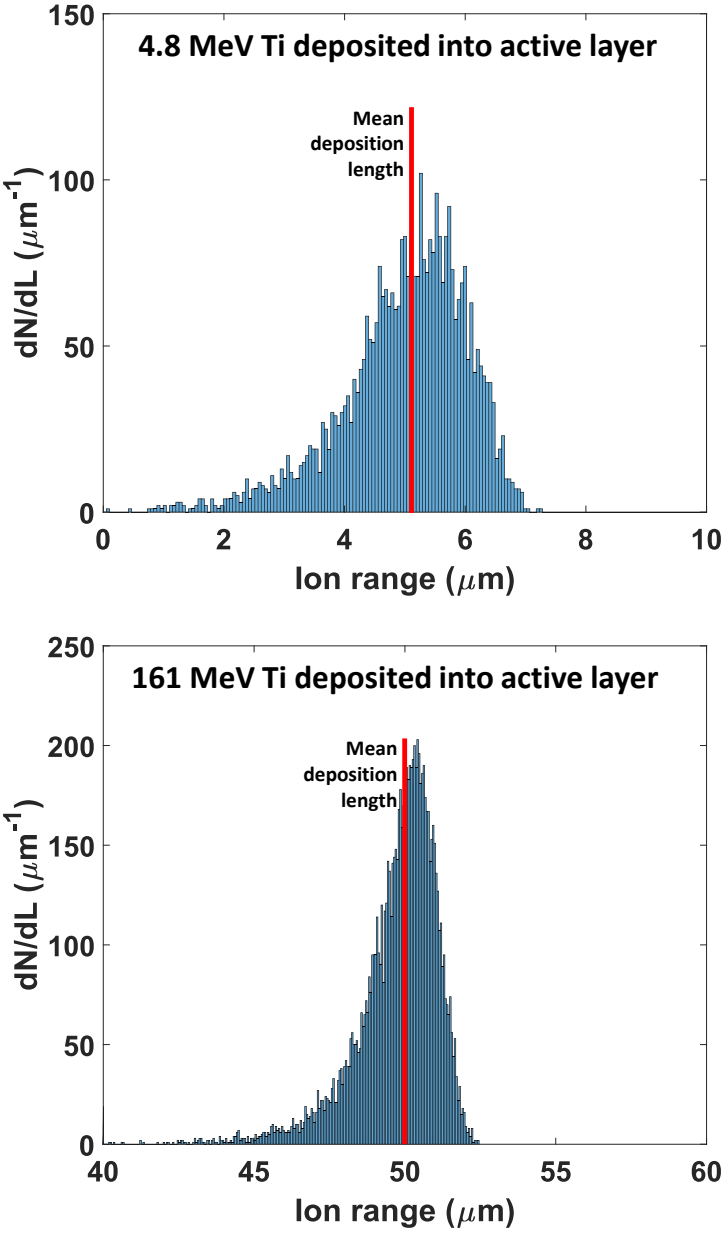

Figure 4.5: Simulations deposited 10,000 mono-energetic titanium ions into the BAS-TR IP, indicating the limitations of the calibration curve. In the top figure, 4.8 MeV titanium ions are deposited in the active layer. At this energy, the PSL signal becomes highly statistical because the range is smaller than the 5 μm grain size [95]. The lower figure illustrates the calibration's high bound of 161 MeV, as at this energy, the ions fully penetrate the 50 μm active layer.

photons [101]. The simulation package SRIM [103] produced simulated stopping power values within the IP active layer. These tabulated data cover the full range of energies valid for the IP

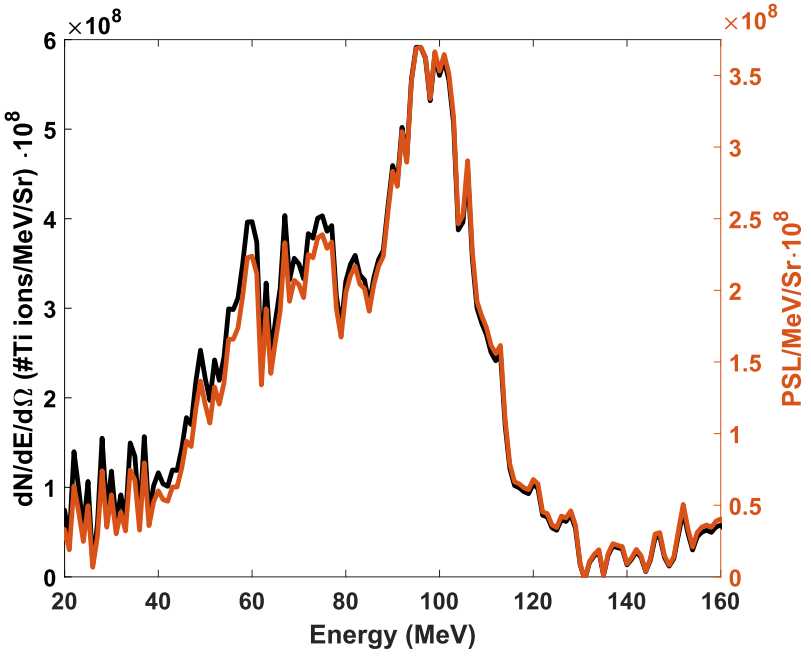

Figure 4.6: Energy spectrum of Ti^{12+} accelerated from the rear side of a 60 nm titanium foil. The black curve displays the applied calibration, and the red curve shows the uncalibrated spectrum in units of PSL.

response function.

In the energy regime of this calibration (4.8 to 161 MeV), the titanium ions do not penetrate the active layer, yielding a sensitivity that depends strongly upon the stopping power. Hence Hidding's stopping-power independent model is a very loose approximation of IP response, with a sensitivity $\alpha = 0.0227 \pm 0.0174$ PSL/MeV. Implementing Bonnet's model reveals far greater precision, yielding $\alpha = 0.0037 \pm 0.0008$ PSL/MeV. The uncertainty was determined from the standard deviation in averaging the tabulated values of α.

According to Bonnet's model, the IP response to protons is twice as sensitive as that to titanium [101, 72]. For protons, Hidding's and Bonnet's model produce sensitivities within the same order of magnitude. However, this is not the case for heavier ions such as titanium, as the Bethe's stopping power formula is proportional to the square of the charge state [105]. The large disagreement between Hidding's and Bonnet's models is reconciled by the increased role of stopping power for heavier ions. Bonnet's studies also indicate an IP quenching effect dependent

upon stopping power [106]. This quenching effect agrees with the calculations presented here. Particles with greater stopping power have a lower IP sensitivity, similar to the response of an organic scintillator [107].

These models are visualized in Figure 4.7, implying that Hidding's model cannot be soundly applied to energetic ions in the mid-Z regime. Bonnet's model does more closely approximate the empirical fit, but has a peak that is not predicted by the SRIM calculations of stopping power. This peak originates instead from Bonnet's prediction that PSL photons generated deep within the active layer are absorbed before they can escape. However, this model is still a weak fit to the data (R^2 = 0.5348), while the empirical model appears to be a better representation of IP response (R^2 = 0.9722). Studies of higher energy titanium ions is warranted to determine the energy where the titanium response function begins a decreasing trend.

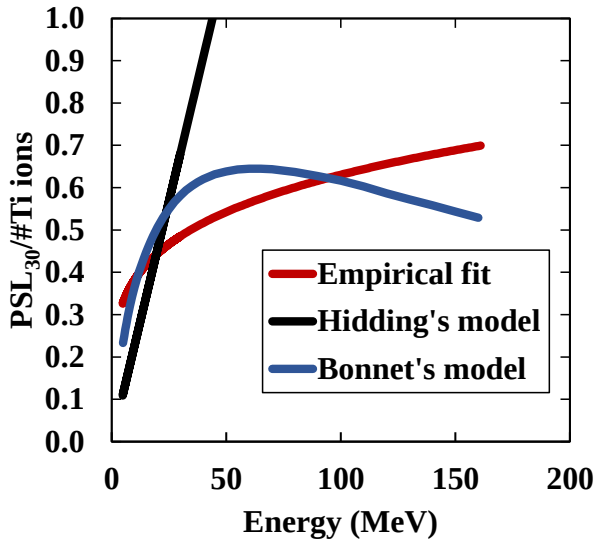

Figure 4.7: Hidding's and Bonnet's models compared against the empirical IP calibration curve fitted in Figure 4.4. Hidding's linear fit model proves to be a poor representation, whereas Bonnet's model demonstrates a more accurate trend. Note that Bonnet's model predicts a peak in IP response due to the absorption of PSL photons within the active layer.

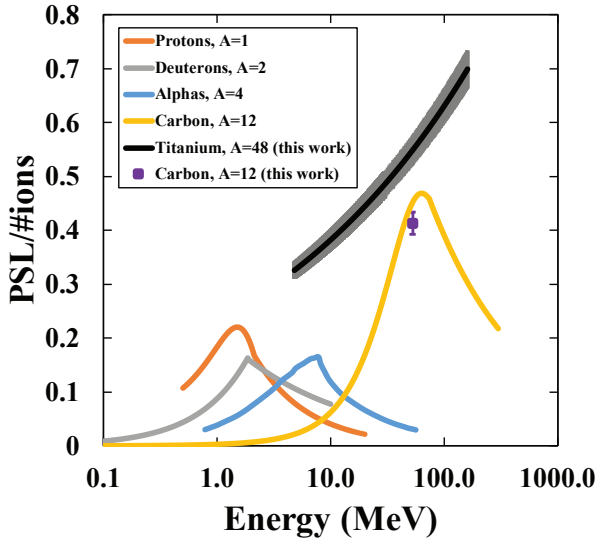

Figure 4.8: BAS-TR IP response curves for ions of varying atomic mass A. Each low-Z calibration shows the peak representing the ion fully penetrating the active layer [95, 97, 98, 106]. The titanium calibration, shown with error bands in its full theoretical range of validity, does not show this peak because no ions were accelerated into the necessary energy domain (>161 MeV). An additional carbon calibration point from this experiment is included.

4.3 Comparison of established IP calibrations

Once the ions fully penetrate the active layer, the depth of the Bragg peak will exceed the thickness of the active layer. Hence, the ions will deposit exponentially less energy into the active layer as incident ion energy increases. Figure 4.8 illustrates this effect in comparing the IP response curves of protons [97], deuterons [98], alpha particles [106], carbon [95], and titanium. The IP response curve for titanium is plotted in its full range of validity as determined by the deposition length simulations executed in SRIM.

All IP-calibrated ion species have a value corresponding to the peak energy deposited in the IP [97, 98, 106, 95]. There is a general trend of the peak PSL/ion/amu value decreasing with increasing atomic mass units A. Using the peak value from previous calibrations (visualized in Figure 4.8), the distribution of peak PSL response for low-Z ions fits the power model $PSL_{30}/ion/amu = aE^b$. This relationship is strengthened with the inclusion of the PSL_{30}/ion/amu value that corresponds with 161 MeV titanium, as shown in Table II. This latter relationship,

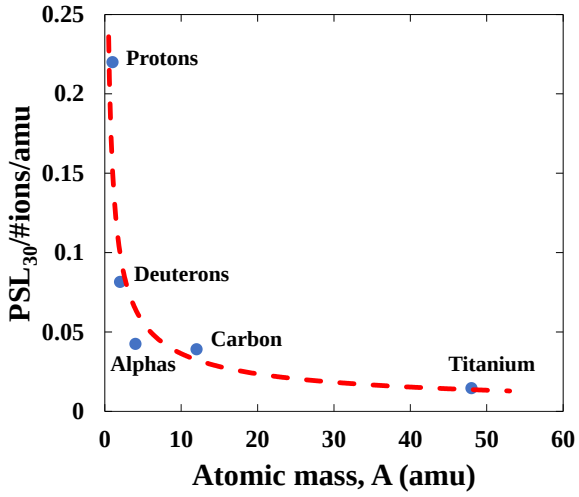

Figure 4.9: IP response vs atomic mass unit A for the maximum energy deposited. The maximum energy deposited, represented by the blue points, directly corresponds to the maximum PSL signal, as represented by the response function peaks in Figure 4.8. This peak occurs for each ion when the Bragg peak depth is equivalent to the thickness of the active layer [97, 98, 106, 95]. According to SRIM calculations, energetic titanium ions reach this depth in the active layer when they reach 161 MeV. The data are best fitted by a power law (dashed line) $PSL_{30}/ion/amu = 0.1531A^{-0.6244}$.

Table 4.4: Fit parameters for IP response vs atomic mass unit A. The fit is of the form $PSL_{30}/ion/amu = aA^b$.

Species	a	b	R^2
Previous calibrations [97, 98, 106, 95]	0.1599	-0.6769	0.8075
Previous calibrations + this work	0.1531	-0.6244	0.9049

plotted in Figure 4.9, indicates that the titanium calibration presented in this paper aligns strongly with this power law decay trend.

4.4 Summary

The BAS-TR IP has been absolutely calibrated to energetic titanium ions using three charge states, spanning in energy from 6 to 27 MeV. The IP response is independent of charge state, and depends solely on the amount of energy deposited within the IP. An empirical power law

fit, valid from 4.8 to 161 MeV, can convert the PSL_{30} signal to absolute number of titanium ions. The uncertainty in PSL for the fitted response function is small, at only ~7%. This calibration provides quantitative measurements of ion energy spectra, allowing for further study in the laser-acceleration of mid-Z ion beams.

Established low-Z calibrations, coupled with the results in this paper, correspond to a power fit law for peak PSL signal vs atomic mass. From raw IP spectra, absolute spectra of various ions can be roughly approximated, within a factor of 2, using this function. Additional IP calibrations, especially with mid-Z or high-Z ions, would strengthen this empirical relationship. This power law also indicates a decreased sensitivity per nucleon with increasing atomic mass, in agreement with Bonnet's IP model applied to titanium ions. In turn, high-Z ions are predicted to exhibit similar IP response functions.

4.5 Acknowledgements

Chapter 4 contains a partial reprint as it appears in J. Strehlow, P. Forestier-Colleoni, C. McGuffey, M. Bailly-Grandvaux, T. S. Daykin, E. McCary, J. Peebles, G. Revet, S. Zhang, T. Ditmire, M. Donovan, G. Dyer, J. Fuchs, E. W. Gaul, D. P. Higginson, G. E. Kemp, M. Martinez, H. S. McLean, M. Spinks, H. Sawada, and F. N. Beg. "The response function of Fujifilm BAS-TR imaging plates to laser-accelerated titanium ions." *Review of Scientific Instruments* 90, 083302 (2019). The dissertation author is the primary investigator and author of this paper. This material is based on work supported by the Air Force Office of Scientific Research (AFOSR) under Award Number FA9550-14-1-0282, and by the Department of Energy, National Nuclear Security Administration (NNSA) under Award Number DE-NA0003842. The authors also acknowledge the support from the technical staff of the Texas Petawatt Laser at the University of Texas, Austin.

Chapter 5

A laser parameter study on proton generation from microtube targets (TPW)

Laser-ion acceleration from μm-thick targets lies in the robust regime of target normal sheath acceleration (TNSA). TNSA can be enhanced with target structures that improve the coupling of laser energy to hot electrons, as electrons are the mediator for accelerating ions with lasers. Many types of structures have seen success in improving the conversion efficiency and temperature for laser-driven electrons, in both PIC simulations and experiments. These include carbon nanotubes [108], nanowires [109, 110, 111, 112], nanoplates [113], foams [75], cones [114], and microtubes [55, 115, 116], all of which are superimposed upon flat foils. Targets with non-protruding structure, such as layered foils [117] and microchannel slabs [118] have also been observed to improve hot electron generation. As electrons are the mediator for energy transfer into the target, similar structures are of interest for a wide variety of applications, including atomic physics [119, 120], THz emission [121], neutron generation [122, 123, 124], x-ray and γ-ray emission [125, 126], positron generation [127], and QED studies [128, 129]. However, the focus of this work is the performance of structured targets in enhancing laser-ion acceleration. Experimental studies have been done to optimize the ion energy and yield from nanospheres [130],

nanowires [110, 131], snow targets [132], layered foils [117], foams [133, 134], and microtubes [14]. Various microstructures are predicted to improve the general TNSA scaling law from $E_{max} \propto I^{1/2}$ to a more favorable linear scaling, $E_{max} \propto I$. [114, 135]. In addition, experiments show that the proton yield relative to unstructured foils is usually increased by a few hundred percent [130, 110].

A complication of structured targets is that they are not readily available, and have to be custom-fabricated, as described in Section 3.3. In summary, fabrication techniques include lithography, electroplating, and 2-photon polymerization (2PP), a form of 3D printing. In addition, the contrast requirement is quite high for structured targets, demanding techniques such as plasma mirrors or frequency doubling crystals. Even minor prepulses with contrasts of 10^{10} have been shown to mitigate the effect of structured targets for ion generation, and accounting for the preplasma has been shown to be critical in ensuring the best match with supporting PIC simulations [131, 136].

Here we extend upon previous microstructure target studies with a laser parameter study on a fixed target geometry. Previous investigations with the ALEPH laser (45 fs, $I = 3 \times 10^{21}$ W/cm^2, 10 J) show that optimized microtube targets can improved proton cutoff energy and conversion efficiency by tens of percent, relative to flat foils. However, with the PHELIX laser, operating at a similar intensity but over $10\times$ the pulse length, only an enhancement in conversion efficiency was measured [14]. With such a long pulse length and high intensity, the short tube was optically shuttered before it could perform optimally, behaving similar to a flat foil with a preplasma. Here we present a comparison of flat vs microtube targets under 3 laser cases: (I) 450 fs, $I = 4 \times 10^{20}$ W/cm^2, 82 J; (II) 140 fs, $I = 4 \times 10^{20}$ W/cm^2, 28 J; and (III) 140 fs, $I = 2 \times 10^{21}$ W/cm^2, 82 J. A direct comparison with fixed energy, pulse length, and intensity reveals that the full energy configurations, I and III, show no benefit of using the microtube targets over flat foils. However, Configuration II accelerates three times as many protons, with an increase in proton cutoff energy from 15 to 25 MeV. A 12% improvement in hot electron temperature is also

Table 5.1: The Texas Petawatt Laser was tuned to three different configurations. The parameters were carefully chosen, within the capabilities of the facility, to make a direct comparison of target performance as a function of laser intensity, energy, and pulse duration.

Config.	Intensity (W/cm^2)	Energy (J)	Pulse duration (fs)
I	4×10^{20}	82	450
II	4×10^{20}	28	140
III	1×10^{21}	82	140

observed.

5.1 Experimental setup and results

The following data were gathered from the Texas Petawatt Laser, in the sub-picosecond, highly relativistic ($\sim 10^{20} - 10^{21}$ W/cm^2) regime. The experimental setup, as illustrated in Figure 5.1, is as follows. A laser pulse of $\lambda_0 = 1.057$ μm reflects off an f/3 off-axis parabola, focusing down to a FWHM spot size of 5.6 μm on target, after reflecting off a plasma mirror. The plasma mirror is a borosilicate slab, with an anti-reflective coating optimized for laser normal incidence on target. The plasma mirror enhances the laser intensity contrast to $\sim 10^{10}$ beyond 100 ps, essential to preserving the integrity of the plastic microtubes 3D-printed onto the 1 μm Ag foils. The microtubes were fabricated via the 2-photon polymerization (2PP) technique, described in Section 3.3, and have a 3 μm inner diameter, 5 μm height, and 0.35 μm wall thickness. A single tube dimension was chosen to guarantee good statistics for each set of laser parameters studied ($\sim$ 10 data samples for each spectrometer), and this particular dimension was shown to have exemplary performance by previous studies of the authors [14]. To benchmark the performance of the microtubes, Ag flat foils were studied under identical laser conditions. To measure the proton energy spectra from the target rear, two Thomson Parabola ion spectrometers were fielded at 0° and 20° from target normal. The EPPS was placed in-between at 8°. In addition, a Radiochromic film (RCF) stack was placed 4 cm from target normal for several shots on each configuration, to

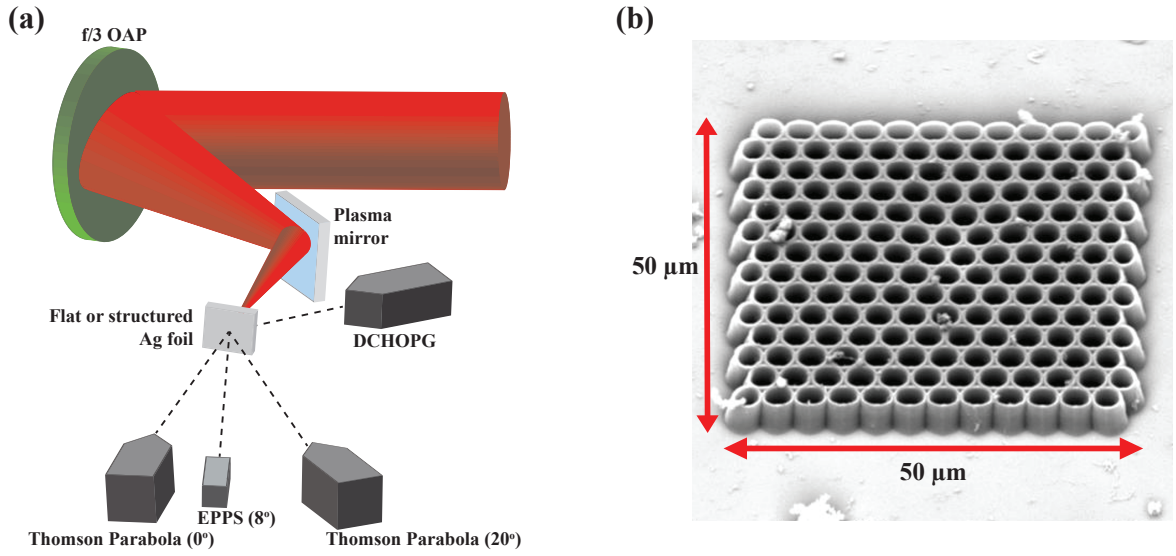

Figure 5.1: (a) Sketch of the experimental setup with the Texas Petawatt Laser, not to scale. After the plasma mirror, the laser is normally incident onto the the front surface, either directly onto a 1 µm flat Ag foil, or the microtube array. A Thomson Parabola (TP) ion spectrometer is placed along target normal, with the EPPS placed off-axis. (b) SEM image of a 3×5 microtube array 3D printed on a 1 µm Ag foil. The large array size relative to the laser spot size eases alignment, and guarantees the laser will hit the array.

study the proton beam enhancement closer to the target than is feasible with the higher-resolution Thomson parabola. The forward hot electron spectra were sub-sampled from an electron, proton, positron spectrometer (EPPS) [71]. Each spectrometer dispersed the charged particles onto imaging plates, which have an active layer sensitive to incident radiation. The imaging plates were scanned with a General Electric Typhoon FLA 7000 IP scanner. The scanner digitizes the image into units of photostimulated luminescence (PSL), which can be converted to absolute numbers of electrons [137] and protons [72].

Figure 5.2 shows the averaged results for each laser case for flat and microtube targets, from both TPs and the EPPS. Each spectrum is an average over all these cases, with the translucent bands representing the standard deviation. The second row of the figure, labeled Configuration II, indicates the laser parameters at which the microtube targets most strongly outperform the flat foils. The proton cutoff energies increase by approximately 50% along target normal (Figure 5.2b), whereas there is no statistically significant difference between the microtube and flat targets

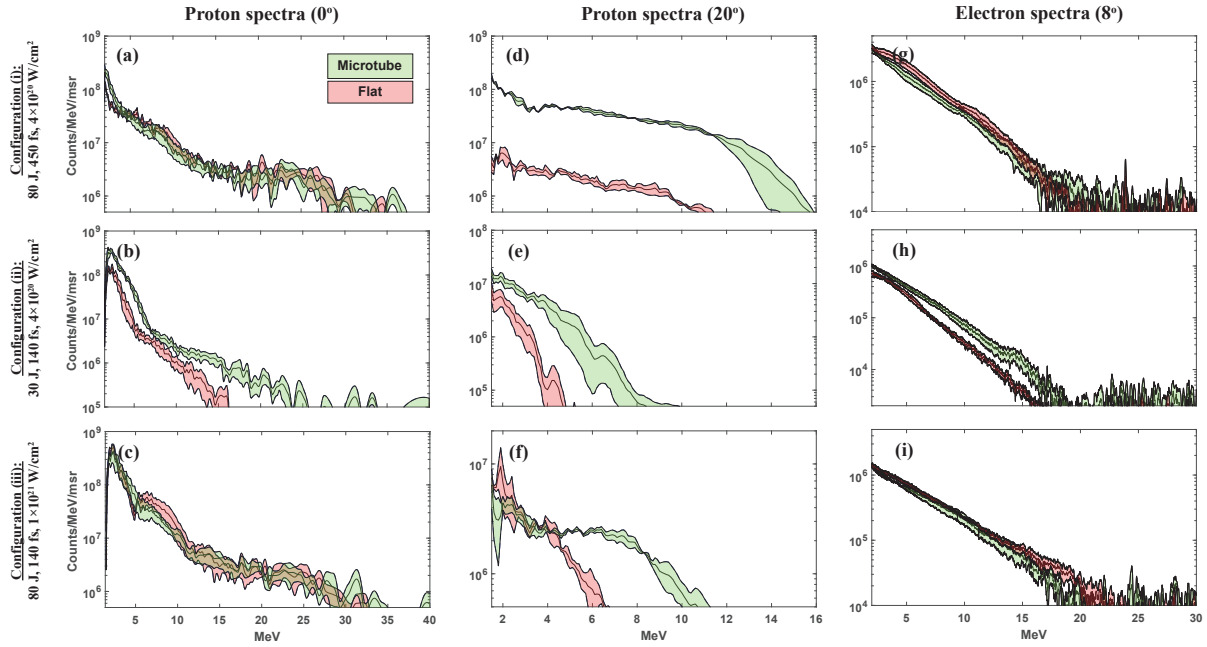

Figure 5.2: Experimental spectra for each laser configuration, showing the protons captured at 0° (a-c) and 20° (d-f), and the electrons at 8° (g-i). The width of each spectrum represents the error bands, as averaged over $\sim 5-10$ shots over each case. Key takeaways from the spectra are summarized in Table 5.2.

when the laser is operating at full energy (Figures 5.2a&c). The relative energetic (>1.5 MeV) proton yield also increases by a factor of 3 across all diagnostics. This is in agreement with the Maxwell-Boltzmann fit to the RCF spectra (Figure 5.3b), where only a mild average yield enhancement ($\sim$10s of percent) was seen on the full energy shots (Figure 5.3a&c). This mild yield increase, however, is consistent with the higher fluxes observed on the 20° TP (Figures 5.2d&f). The extracted proton cutoff energies and yields from each diagnostic are summarized in Table 5.2.

Though there are more protons captured at 20° with microtube targets, this does not necessarily correspond with a higher divergence. The RCF data show that with microtube targets, in addition to a cutoff energy boost, the transverse beam profile may also be modified. As plotted in Figure 5.4a&c, for the full energy configurations, the FWHM beam profiles remain virtually identical, with overlapping error bands. However, for the lower energy configuration of Figure

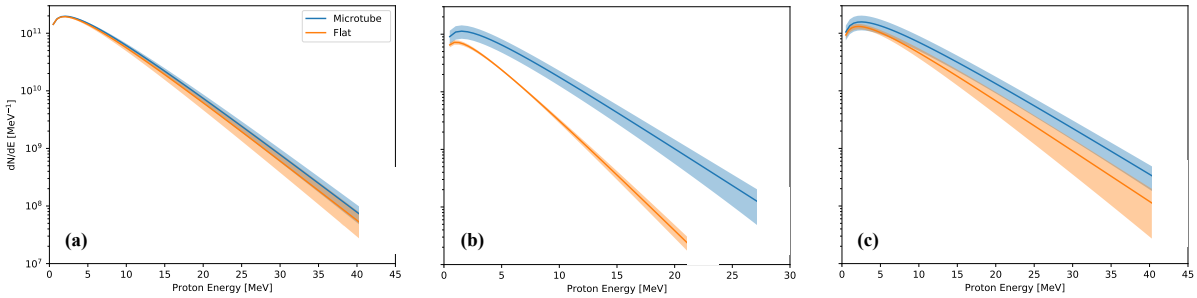

Figure 5.3: Maxwell-Boltzmann fit to the RCF spectra, with error translucent error bands representative of the standard deviation. Configurations (i), (ii), and (ii) correspond to Figures (a), (b), and (c), respectively. Cutoff energies and yields are compared with the Thomson parabola data in Table 5.2.

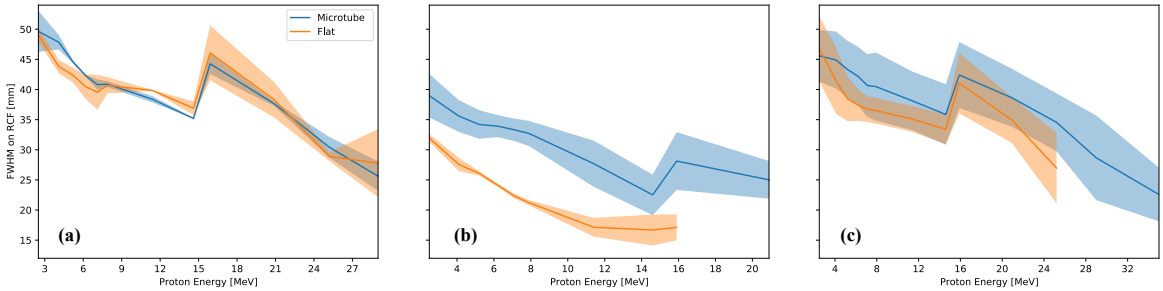

Figure 5.4: Axially-averaged transverse spread (FWHM) of the proton beam, as measured by the RCF stacks. Configurations (i), (ii), and (ii) correspond to Figures (a), (b), and (c). Configuration (ii) indicates that microtubes increase the beam spread by ∼50%.

5.4b, there is a dramatic shift in the beam profile. Relative to flat foils, microtubes increase the beam spot by $\sim 50\%$ for this configuration.

The electron spectra from each laser configuration occupy a similar trend (Figures 5.2g-i). The spectra from the full energy configurations (Figures 5.2g&i) overlap in error bands, though the 140 fs pulse case has a higher electron temperature than the longer pulse case ($T_{e,avg}$ = 4.40 MeV vs $T_{e,avg}$ = 3.64 MeV). The spectra from Configuration II, however, show a 12% increase in T_e (3.15 vs 2.81 MeV), with no overlap in the error bands. All temperature measurements were extracted via a least-squares regression, with excellent fits of $R^2 > 0.99$. This electron enhancement with microtube targets provides direct evidence that a pre-formed channel can improve the coupling efficiency of the laser energy to hot electrons.

Table 5.2: (Above) Summary of proton cutoff energy enhancement E_{max}, as measured by the three ion diagnostics. Due to considerable overlap in the error bands of the proton spectra, there is no measurable difference in E_{max} for the full energy shots, Configurations I and III, along target normal. Configuration II, with the laser energy attenuated to 28 J, shows good agreement in proton energy enhancement between the 0° TP and RCF. Here, the average spectra show a $\sim 50\%$ improvement in E_{max} for the microtube targets relative to flat foils. (Below) Relative energetic (>1.5 MeV) proton yields as measured by each diagnostic, as determined by the spectral average. Configuration II shows a $\sim 3\times$ enhancement in proton yield across all diagnostics.

Config.	$E_{max,tube}/E_{max,flat}$ (0°)	$E_{max,tube}/E_{max,flat}$ (20°)	$E_{max,tube}/E_{max,flat}$ (RCF)
i	~ 1	1.43	~ 1
ii	1.56	1.79	1.38
iii	~ 1	1.62	~ 1

Config.	Y_{tube}/Y_{flat} (0°)	Y_{tube}/Y_{flat} (20°)	Y_{tube}/Y_{flat} (RCF)
i	1.21	19.64	1.07
ii	2.90	3.25	2.61
iii	0.88	1.32	1.42

The Dual-Channel (DC) spectrometer with two HOPG crystals (DCHOPG), described in detail in Chapter 3, was used to extract the average ionization state of the bulk Ag foil. The spectra measured by this diagnostic shows that the energy of the line emission depends on the target type, and not across the range of laser parameters studied here. With direct laser irradiation of the foil, the Ag can reach a Helium-like ionization state, emitting a spectral peak which centers on 22.7 keV. Comparisons with atomic physics simulations (Figure 5.5 and 5.3) suggest that flat targets reach an average ionization state of Ag^{30+}. When the laser irradiates microtube targets, however, the microtube interaction prevents the laser from reaching the Ag substrate directly. In this case, the 22.1 keV emission detected by the DCHOPG is characteristic of Ag K_α, and the Ag substrate becomes Helium-like, reaching Ag^{45+}. This data is further compared with published spectra from the X-Ray Data Booklet (XRDB) [138] in Table 5.3, also showing excellent agreement.

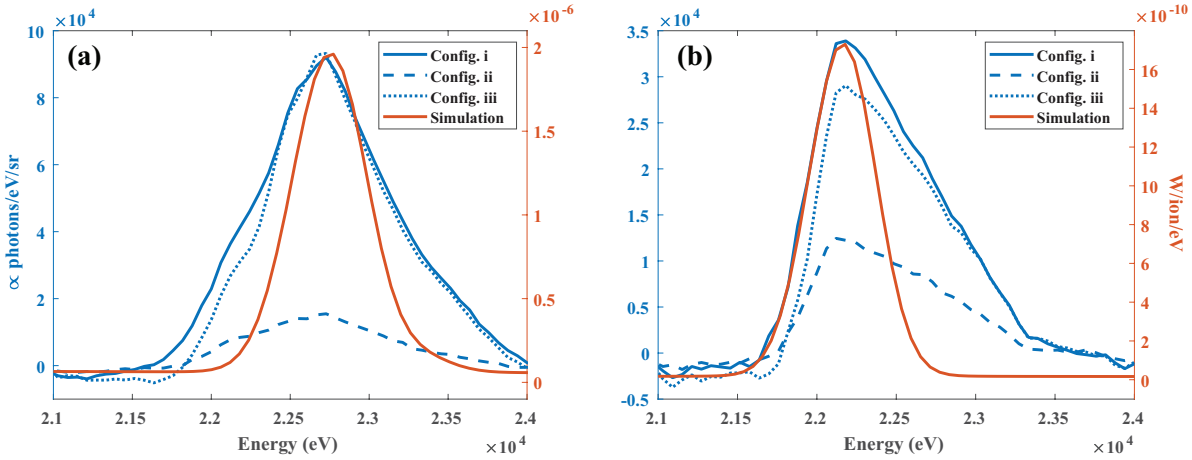

Figure 5.5: Experimental data (blue lines) from the DCHOPG for (a) flat foils and (b) microtube targets. The red lines were generated via atomic physics simulations for Helium-like Ag, plotted in (a), and Ag K_α, plotted in (b). See Table 5.3 for additional comparisons with published Ag spectra. Laser configuration ii (dashed line) has ∼1/3 of the energy of configurations i iii, resulting in the lower x-ray yield observed here. See Table 5.1 for the specific details of the laser configurations.

Table 5.3: Comparison of the Ag emission line peaks from this experiment, the X-Ray Data Booklet (XRDB) [138], and atomic physics simulations. The above row matches data from the flat targets, and the microtube target data are matched below. Flat foils reach Helium-like ions (Ag^{45+}), while the direct interaction with microtubes prohibits such high ionization.

	Config. I	Config. II	Config. III	XRDB	SNL sim.
ε (keV)	22.73	22.73	22.73	22.61 ($2p^3P_1$); 22.85 ($2p^1P_1$)	22.77 (Ag^{45+})
ε (keV)	22.18	22.12	22.18	22.16 ($K_{\alpha 1}$)	22.18 (Ag^{30+})

5.2 Supporting simulations

5.2.1 Initial conditions

To evaluate the role of a tube pre-expansion by the laser prepulse on-target performance, we performed 2D FLASH radiation hydrodynamic simulation of a microtube target. The microtubes have an inner diameter of 3 μm and a height of 5 μm and are attached on a 1 m thick Ag foil. The simulations are performed in 2D cylindrical geometry, using the equation-of-state and multi-group opacity tables from PROPACEOS [139]. The prepulse intensity pulse shape is calculated from the laser intensity contrast measured by the facility with a third-order autocorrelator. The reflectance of the plasma mirror anti-reflective coating is calculated using manufacturer curves and has been evaluated to 0.07% with the s-polarized laser at $\lambda_0 = 1.057$ μm and with an incidence angle of 30° on the plasma mirror. FLASH uses an Adaptative Mesh Refinement (AMR) and the coarsest/finest mesh size used is 0.1 μm/0.006 μm in both directions, respectively. The time step is constrained by a Courant-Friedrich-Lewy (CFL) limit of 0.4. The laser deposition is realized through a 3D ray-tracing projection on the cylindrical domain and the laser spatial profile is Gaussian with an FWHM spot diameter of 5.6 m and is focused onto the foil's front surface at (r,z)=(0,0).

The density profile created during the FLASH simulation was then imported into EPOCH for the 82 J laser case, as the preplasma of the 28 J case was observed to be classically transparent. The simulation domain is of the size (L_x, L_y) = (15.0, 45.0) μm , where x is the laser propagation direction, and y is the transverse direction in which the laser electric field is polarized. The number of computational cells is (N_x, N_y) = (4500, 1600), corresponding to a cell size of $\Delta x = \Delta y = 0.01$ μm. At the left-hand boundary of the 1 μm Ag foil ($x = 15$) μm, where the 1.057 μm wavelength laser, injected from the left, focuses to a FWHM spot size of 5.6 μm. The Ag foil is initialized with ionization Ag^{30+}, at a solid density of $60n_c$, with 400 particles/cell. The CH microtubes are fully ionized with a density of $46n_c$, at 100 particles/cell. The rear surface has a 60 nm thick

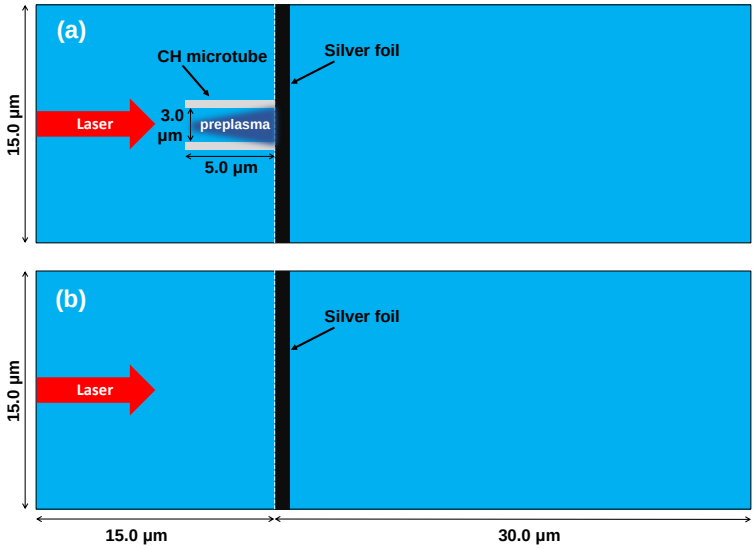

Figure 5.6: Diagram of the 2D simulation domain in EPOCH, with microtube targets (a) and flat targets (b). FLASH simulations were used to generate a preplasma profile inside the microtubes, which were then imported into EPOCH for the over-critical (82 J) case.

layer of H contaminants, with a density of $3n_c$ and 400 particles/cell. The laser and microtube are both centered in y of the simulation box, which has open boundaries in all directions. The microtube is of 3 μm inner diameter, 5 μm in height, and has walls 350 nm thick, corresponding to physical measurements of the microtube targets. The laser intensity, energy, and pulse duration were varied, corresponding to the parameters of Table 5.1, for both microtube and flat targets.

5.2.2 Modeling the laser-plasma interaction

To investigate the role of microtubes in enhancing electron and proton generation, a combination of both radiation-hydrodynamic (rad-hydro) and particle-in-cell (PIC) simulations are advantageous. After the plasma mirror, the TPW laser is a high-contrast system ($\sim 10^{10}$), yet the attenuated prepulse is still not eliminated. To determine the role of the laser prepulse, the rad-hydro code FLASH [79] was executed for both the 28 J and 82 J laser cases, as the magnitude of the TPW prepulse depends solely on the main pulse intensity. For the optimum laser case of

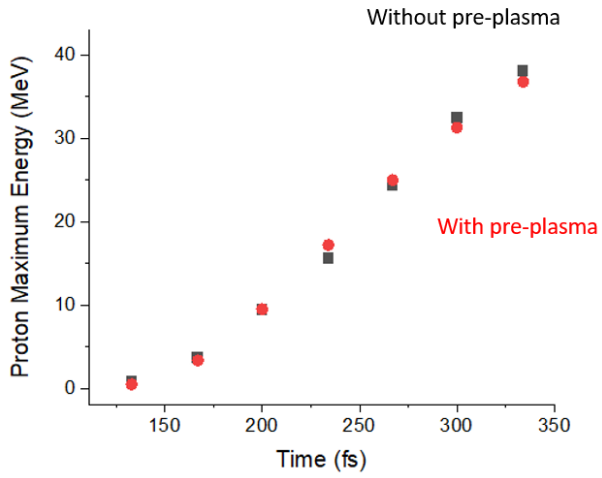

Figure 5.7: Evolution of maximum proton energy vs time for two cases of Configuration II (140 fs, $I = 4 \times 10^{20}$ W/cm^2, 28 J). The difference in proton acceleration with and without the preplasma profile is negligible.

28 J, the prepulse produces an undercritical preplasma inside the microtube, whereas for the 82 J laser, the preplasma is overcritical. The transparent preplasma was thus not necessary to account for in PIC for the optimum laser case of 28 J, 140 fs, and a case was run with the preplasma to confirm (Figure 5.7). Figure 5.8 summarizes the results calculated in EPOCH [86] for the optimum laser case. The longitudinal electric fields, which are responsible for accelerating the rear-surface protons via the TNSA mechanism, are higher by a factor of 2 for the microtube case (Figure 5.8a-b). This same enhancement factor was also observed in a similar numerical study of Snyder, et al. for a laser 10$\times$ the intensity [140]. The electrons, dragged out of the tube walls, provide the primary source of enhancement [115, 116]. With tube structures, the electron temperature increases by nearly a factor of 3, from 2.34 MeV to 6.85 MeV. The tube structures also improve the laser coupling to the population of electrons originating from the flat substrate only, increasing this sub-sample of the electron temperature by 85%. However, electrons originating from the tube walls dominate the total accelerated population by orders of magnitude, as shown by the overlap of the black and orange lines in (c). These lines have near-identical temperatures, within 4% of each other, of $T_{hot} \approx 7$ MeV. All fits were extracted

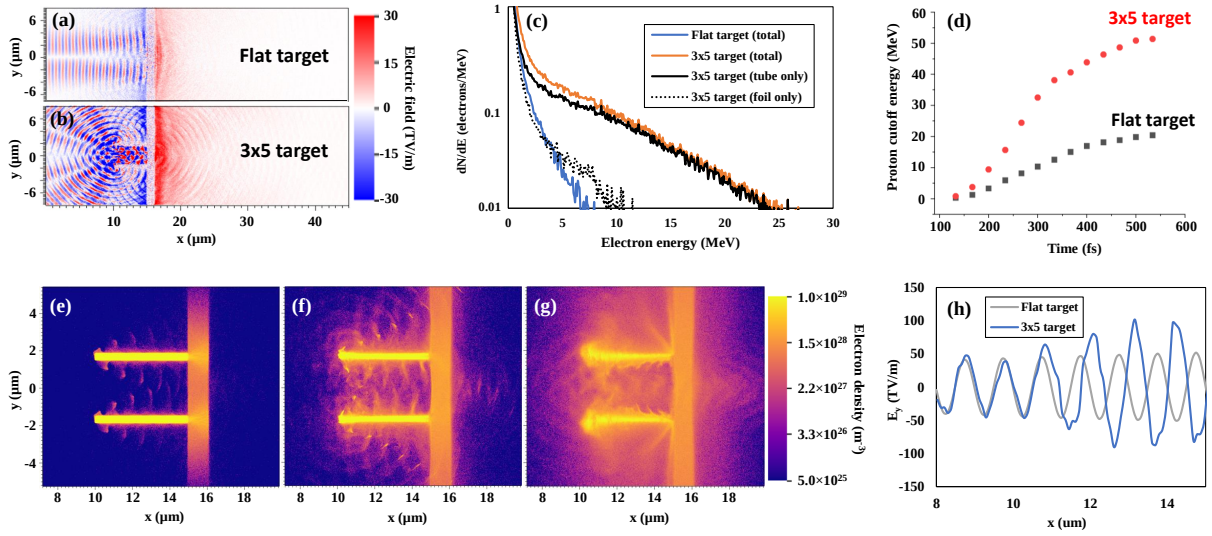

Figure 5.8: Comparison of flat and microtube (3×5) targets for the optimum laser case (28 J, 140 fs). The longitudinal electric field in the flat foil (a) is outperformed by the microtube target (b), shown at approximately laser peak arrival at 233 fs. This stronger electric field is indicative of dramatic increase in the acceleration of electrons from microtube targets (c). The distribution of forward-accelerated electrons from the foil is similar, regardless of whether a target structure is in place. Microtubes provide an additional source of hot electrons that dominates the energy spectrum. (d) shows that as the simulation progresses, the maximum proton energy doubles relative to flat targets (e-g) show the evolution of extraction from the microtube walls, respectively at 110, 220, and 330 fs. The laser field also self-focuses up to a factor of 2 in the microtube, shown here at 266 fs (f).

with the least-squares method, with coefficients $R^2 > 0.97$. The correlation between E_x and T_{hot} agrees with the Wilks' scaling of $eE_x \sim T_{hot}/\lambda_D$, where λ_D is the Debye sheath [12]. As a result, as the simulation progresses, protons accelerated from the rear surface of microtube targets gain double the maximum energy relative to flat foils (Figure 5.8d). The simulation was not successful in predicting the $3\times$ increase in accelerated proton yield, instead calculating that the yields were nearly identical. This indicates that the contaminant layer was fully depleted, and was not perfectly representative of the experiment. Contaminant layers have proven difficult to characterize [141], and estimates range from a few nm [142] to 1 μm [143], and can vary significantly depending on material adhesion and environmental factors [52].

The evolution of the electron density map (5.8e-g) gives a qualitative picture of the tube's

role in providing electrons. 110 fs into the simulation, as the laser pulse is ramping up, periodic structures emerge from the tube walls (e). These structures of periodicity $\sim \lambda_0$ result from laser fields strong enough to disrupt the Langmuir oscillation within the dense plasma [144, 115]. These features continue to grow as the laser peak reaches the target (f). As the laser pulse ramps down 330 fs into the simulation, the tube walls are largely disrupted, forming an overcritical channel (g). Before the channel becomes overcritical, however, the plasma expanding from the tube walls causes the laser to focus, doubling the laser field (h). For the peak intensity of the laser interaction around ∼200-300 fs, the narrowing channel (f) and doubling laser field (h) are consistent with the so-called "depletion regime" identified by Ji, et al. in their 3D numerical study on lensing effects in microtubes [55]. Lasers of intensities $10^{20} - 10^{21}$ W/cm^2 fall into the heart of the depletion regime, meaning the focusing effect of the microtube can drop as low as a factor of $\sim 2\times$ according to their numerical study. A $2\times$ laser field amplification was observed here, corresponding to a $4\times$ increase in intensity. The discrepancy is likely a result of the constraint of 2D simulations, as well as a shorter pulse duration (40 fs) propagating through a much longer tube (120 μm). For three dimensions, in the focusing regime of $\gtrsim 10^{22}$ W/cm^2, which was not accessed here, the intensification factor is predicted to exceed $3\times$, increasing logarithmically with input intensity. For this experimental study, however, lying in the depletion regime suggests that the lensing effect is only a minor contributor to enhancing proton acceleration.

For the TPW laser facility, the intensity profile of the laser prepulse depends solely on the main pulse intensity. The FLASH code predicts that for the 82 J laser, the preplasma is overcritical and causes the central microtube to behave like a closed shutter (Figure 5.9a). EPOCH simulations were executed for a main pulse of 140 fs, 10^{21} W/cm^2, corresponding to Configuration III of the experiment. With this laser pulse, two cases were studied in EPOCH to compare the role of the preplasma inside the microtube for high energy pulses. Without the preplasma (Figure 5.9b), electrons sourced from the microtube dominate the hot electron population. This behavior is similar to optimum case, where the pulse length is the same but the energy is attenuated to

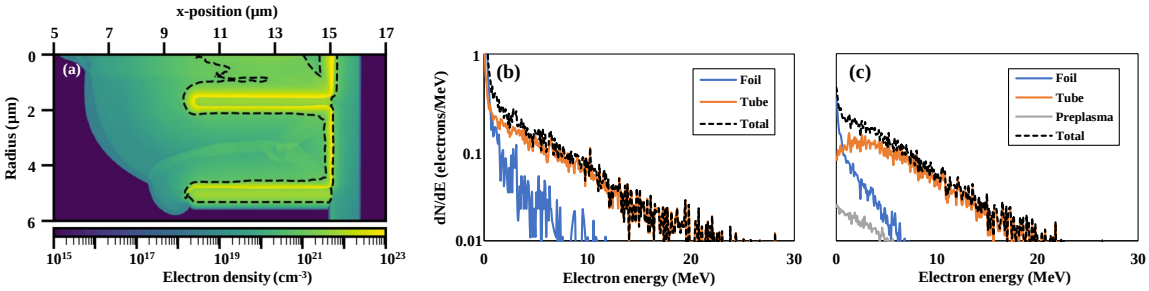

Figure 5.9: The role of the preplasma for structured targets at high drive energy (82 J). (a) shows the density profile generated by the prepulse, with a contour (dashed line) indicating the overcritical region. These data were extracted 3 ps before the peak of the main pulse arrives. (b) and (c) compare the spectra of forward-accelerated electrons without and with the preplasma, respectively, from each target component. Tube structures are the dominant source of hot electrons. The over-critical preplasma in (a) reduces the total number of electrons accelerated >100 keV by ∼50% (c). The density profile of (a) was assumed to be cylindrically symmetric for the EPOCH simulation.

28 J (5.8c). Though this preplasma does not change this qualitative behavior, the number of accelerated electrons is dramatically reduced. The energy spectra of 5.9c show that the electron counts from the tube (orange line) break from an exponential spectrum below 7 MeV. Integrating over the total electron counts (black lines), the preplasma decreases the number of accelerated electrons >100 keV by ∼50%. Though the preplasma provides an additional source of electrons (grey line), those electron counts are nearly two orders of magnitude too small to contribute on the same scale as the tubes. In effect, the simulations indicate that the 82 J laser pulse is interacting with an overcritical plasma slab of 6 μm in thickness. Hence, the 450 fs laser case was not executed in EPOCH, as it has a slightly lower intensity of 4×10^{20} W/cm^2. For classical TNSA with scaling $E_{max} \propto I^{1/2}$, [34] this is not predicted to result in a stronger interaction.

This work is closely related to previous experiments that the author has assisted with on the ALEPH and PHELIX laser facilities [14]. However, the goals of these experiments were to find an optimized target geometry for fixed laser parameters. The intensities of these lasers is on the order of TPW at best compression ($\sim 10^{21}$ W/cm^2), but they respectively have FWHM pulse durations of 45 fs and 500 fs. For the 45 fs laser case, the microtubes enhance proton

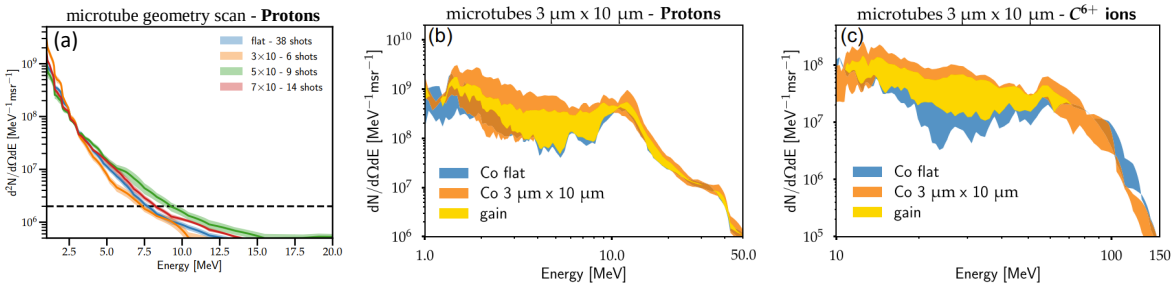

Figure 5.10: Microtubes enhance ion acceleration relative to flat foils along the target normal direction. The ALEPH laser (a) produced solely protons above the detection threshold (dashed line), while PHELIX, with its 10× greater energy and pulse duration, produced protons (b) as well as carbons (c). Figure modified from Ref. [14].

production more modestly than TPW, with cutoff energies increasing by ∼20% and conversion efficiencies by ∼40% (Figure 5.10a). This smaller enhancement suggests that longer pulse durations are necessary to take full advantage of electron extraction from the channel. However, if the pulse duration approaches 500 fs, no increase in cutoff energy is measured (Figure 5.10b-c), in agreement with the TPW results presented here.

5.3 Summary

The laser-acceleration of protons from microtube targets was investigated experimentally for three laser cases, shedding light on the interplay of laser intensity, pulse duration, and energy. For the laser parameters studied (Table 5.1), it was found that the from the low energy laser case (28 J), microtube targets outperformed flat foils in maximum proton energy by 50%, and energetic proton yield by ∼3×. When the laser was at full energy (82 J), the proton energy and yield showed no statistically significant dependence on pulse duration (140 or 450 fs), intensity (4×10^{20} or 1×10^{21} W/cm^2), or target type. FLASH simulations indicate that despite the presence of a plasma mirror, the highest intensity laser case drives an overcritical preplasma, shuttering the microtube from the main pulse. For the longer pulse case (450 fs at 4×10^{20} W/cm^2), microtube performance is also limited, as the microtube is shuttered during the main

pulse interaction [14]. For intensities of 4×10^{20} W/cm^2, the preplasma is low enough density to be classically transparent. According to the simulations, for a sufficiently short pulse (140 fs), the sheath field and electron temperature are more than doubled, as is the proton cutoff energy. Though the trend is in qualitative agreement with experimental results, the 2D PIC simulations overestimate the experimental electron temperature and cutoff energy enhancement (12% and 50%, respectively). The simulations were also not able to capture the $\sim 3\times$ increase in proton yield, likely because the contaminant layer is difficult to characterize. The main source of proton enhancement is driven by additional hot electrons accelerated from the tube walls, while light intensification is a minor contributor. For the highest intensity laser case ($I = 1 \times 10^{21}$ W/cm^2, 140 fs, 82 J), including the preplasma decreases number of hot electrons >100 keV by 50%. The other high energy laser case, with its pulse stretched to 450 fs, was not simulated as the tube shuttering effect at $\sim$500 fs pulse lengths was studied extensively in Bailly-Grandvaux, et al. [14] The experimental results presented here are consistent with this reference, and support that optimizing the microtube geometry for these pulse lengths is a topic of future study.

For sufficiently high intensity laser pulses $\gtrsim 10^{20}$ W/cm^2, numerical and experimental results on structured target enhancement begin to diverge. For a variety of numerical studies on laser-driven radiation sources [55, 115, 124], microstructured targets of a fixed geometry consistently outperform flat targets for arbitrarily high laser intensities. Approximating a high contrast laser pulse to be of infinite contrast may hold for lasers $\lesssim 10^{20}$ W/cm^2, but in reality, higher intensity pulses are accompanied by increasingly damaging prepulses. The experimental study presented here suggests that for higher intensity laser pulses, the optimum microstructure geometry should be modified to continue the trend of superior performance of structured targets. Future experiments are of interest to determine the modified target geometries necessary as intensities beyond 10^{22} W/cm^2 become more widely available.

Many applications benefit as structured targets become further optimized. As demonstrated in this work, under the right conditions, microtube targets can dramatically increase proton

production. This energy and yield enhancement is of great utility for dense plasma physics. For example, larger fluxes provide more protons per energy bin, which is advantageous when injecting a proton beam into an energy selector. This shows promise for laser-driven injectors for radiofrequency accelerators [145], as well as providing higher resolution data-sets for warm dense matter stopping power studies [146]. Higher proton fluxes also directly benefit neutron generation for nuclear science and national security applications, as energetic protons can be converted into neutrons via a "catcher" material, such as lithium or beryllium [147, 148].

The MeV electrons from laser-solid interactions can also produce intense sources of MeV photons, or γ-rays, when injected into a high-Z substrate [149]. Increasing the electron population via microtube targets is a promising avenue towards increasing the conversion efficiency of γ-ray sources, which has been predicted though simulations for microtubes [55] and observed experimentally for nanowire targets [111]. Recent progress in target fabrication includes microtube targets filled with relativistically transparent foams, which have already been shown to improve the generation of hot electrons and betatron photons relative to flat targets [15]. A study directly comparing proton, electron, and γ generation from hollow and foam-filled microtubes is a topic of future investigation, as discussed in Section 7.

5.4 Acknowledgements

Chapter 5 contains a partial reprint of a manuscript in preparation for submission to *Scientific Reports*, as J. Strehlow, M. Bailly-Grandvaux, J. Kim, S. Bolanos, H. Smith, A. Haid, E.L. Alfonso, C. Aniculaesi, H. Chen, T. Ditmire, M.E. Donovan, B.M. Hegelich, T. Ma, H.S. McLean, H.J. Quevedo, M.M. Spinks, and F.N. Beg. “A laser parameter study on enhancing proton generation from microtube foil targets.” The dissertation author is the primary investigator and author of this work. This work is supported by the DOE NNSA under Award Numbers DE-NA0003842 and DE-NA0003525; by Triad National Security, LLC, for the DOE NNSA

under Contract No. 89233218CNA000001; and by the DOE Office of Science, Fusion Energy Sciences under Contract No. DE-SC0021125, the LaserNetUS initiative at the Texas Petawatt Laser facility.

Chapter 6

A pulse length study on heavy ion acceleration from ultrathin foils

In this chapter, through PIC simulations, we compare the acceleration of laser-driven titanium ions from ultrathin titanium foil targets from lasers of two different pulse durations, 140 fs and 650 fs. The intensity, a critical ion energy scaling parameter, is fixed to 6.0×10^{20} W/cm^2. The laser is normally incident on the foil target. We consider foil thicknesses ranging from 10 – 500 nm, to determine the optimum target thickness for generating energetic titanium ions. If it is too thin, the target becomes transparent to the laser before the laser field ramps up to its peak intensity. With thicker foils, the cutoff energy trends indicate the transition into the TNSA regime, generating titanium ions with even lower energies than those accelerated from the thinnest targets studied. Observing this transition via a thickness scan has been investigated on a wide variety of solid targets in the transparency regime, including cryogenic hydrogen jets [40] and ultrathin foils [43, 150, 151, 152, 153, 154, 155, 156].

For both laser optima, irrespective of collisions, we show that the mechanisms of energetic ion generation remain the same. Though TNSA is dominant, it is enhanced by brief stages of hole-boring radiation pressure (HB-RPA) and shock wave acceleration (SWA), whose mechanisms are

described in detail in Section 2.2. When the target goes transparent, RPA and SWA inject fast ions into the rear sheath field typical of TNSA. Including binary collisions in the PIC simulation plays a negligible role for the 140 fs laser, but enhances the ion beam generated by the 650 fs laser. The longer laser-plasma interaction gives enough time for collisional ionization to generate $20\times$ the population of Ti^{21-22+}, and increases the maximum ion energy by $\sim 15\%$. Collisional ionization also raises the electron density within the plasma, delaying target transparency and decreasing the optimum thickness by 50 nm.

6.1 Simulation conditions

In simulations of heavy ion acceleration, accurate modeling of the ionization processes is essential, since the interaction is initiated from the neutral state (or lower charge states due to the laser prepulse). These processes act on different time scales depending on the mechanism of ionization, for example the ionization via the laser field, or impact ionization via sufficiently energetic electrons. The acceleration mechanisms are further complicated by, and critically depend on, the generation of ions of various q/m ratios.

As discussed in Section 3.5, the Extended Particle-in-Cell (EPIC) code [85] has the capabilities needed to understand the interplay of these complex processes. The dominant ionization process is field ionization, based on the model proposed by Ammosov, Delone, and Krainov (ADK) in 1987 [84]. With the ADK model, EPIC calculates the ionization rate based on the local electric field within each cell, including the electrostatic and electromagnetic component. EPIC can also account for impact ionization through binary collisions, based on the binary-encounter Bethe (BEB) model [90]. When two charged particles occupy the same cell, they can transfer their energy through collisions, which is executed by particle pairing methods within the cell [157, 158]. When a charged particle of sufficient energy encounters a bound electron, impact ionization allows for this electron to be freed. The scattering angle is determined by the Spitzer

thermal theory [159], changing the particle trajectory and contributing to the plasma evolution. EPIC can self-consistently analyze both the ionization dynamics and acceleration dynamics of heavy ions throughout the laser-plasma interaction. EPIC can run with only field ionization, or with field and collisional ionization both included.

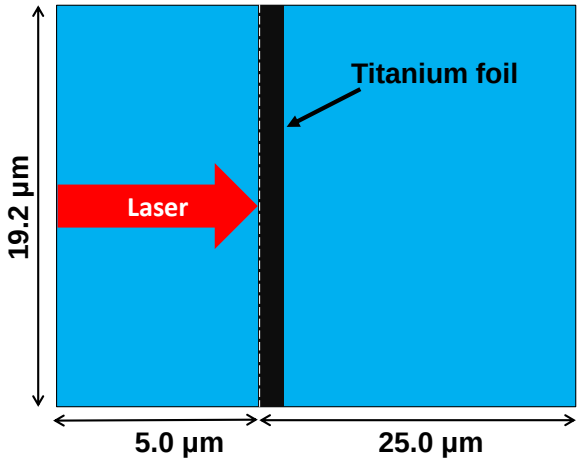

Figure 6.1: Sketch of the 2D simulation domain used in the Extended Particle-in-Cell code (EPIC). The left boundary of the target is set at $x = 5.0$ µm. The $I = 6.0 \times 10^{20}$ W/cm^2 laser centered on the target at normal incidence.

The simulation domain, sketched in Figure 6.1, has open boundaries in all directions, with dimensions (L_x, L_y) = (30.0, 19.2) µm. In this setup, x is the laser propagation direction, and y is the transverse direction in which the laser electric field is polarized. The number of computational cells is defined as (N_x, N_y) = (6000, 3840), and the size of each computational cell is $\Delta x = \Delta y = 0.005$ µm. A p-polarized laser is injected from the center of the left boundary, and propagates in vacuum until it reaches an ultrathin titanium foil positioned normal to the laser axis. At this point, the 1.0 µm wavelength laser is focused to a 5.0 µm FWHM spot size. The laser pulse has a peak intensity of $I = 6.0 \times 10^{20}$ W/cm^2, which corresponds to $a_0 = 0.85(\frac{I(\lambda[\mu m])^2}{10^{18}[W/cm^2]})^{1/2}$ = 20.82 [160]. The temporal laser profile is a Gaussian distribution of the form $exp[-4(t - t_{peak})^2/\tau^2]$, where t_{peak} is the time for the laser intensity to rise to its peak value, and τ is the 1/e pulse duration. τ is set to 168 fs or 781 fs for each laser case. t_{peak} is

equal to the FWHM pulse duration, and the respective energies are 120 J and 550 J. By fixing the intensity but varying the pulse duration, the effect of pulse duration on titanium acceleration can be studied. The laser is assumed to be of high contrast, therefore a laser pre-pulse is not considered. For ultrathin, mid-Z foils, the laser contrast must be $> 10^{10}$ in order to preserve the integrity of the target upon the arrival of the main pulse [32]. A lower contrast can cause pre-expansion of the target, lengthening the sharp gradient required for classical TNSA [161], and dampening the onset of volumetric acceleration mechanisms such as RPA [16] and SWA [62].

The flat titanium foils range from 10 – 500 nm in thickness, with a 10 nm CH contaminant layer on the rear surface. Although naturally present in uncleaned targets, the front surface contaminant layer can be removed with target cleaning practices and the engineering of contaminant layers [141]. A cleaned front surface allows for direct exposure of the titanium foil to the laser, preventing the generation of a low-Z plasma in front of the mid-Z foil. The target is at solid density, with titanium at 5.64×10^{22} atoms/cm^3 (400 particles/cell), and C and H are of equal density and population, at 4.60×10^{22} atoms/cm^3 (150 particles/cell). In this paper, the focus is on the acceleration of titanium ions. We will address the acceleration of impurities in future publications. The left boundary of the target is set at $x = 5.0$ μm, and the right boundary varies with target thickness. The timestep of the simulation is $\Delta t = 0.1\Delta_{x,y}/c$, which satisfies the Counrant-Friedrichs-Lewy (CFL) condition [82].

For these laser parameters, the titanium target is not readily field-ionized. Figure 3.14 of Section 3.5 shows the field ionization rate for titanium across 15 orders of magnitude of laser intensity. There are $\sim 10^{19}$ ionization events/sec for L-shell titanium (Ti^{13+}-Ti^{20+}), eight orders of magnitude higher than that of K-shell titanium (Ti^{21+}-Ti^{22+}). The laser field can ionize the N, M, and L-shells, but is not sufficiently large to ionize the K-shell. Therefore, titanium makes for an interesting test case, where collisions can be toggled on and off to determine the roles of field and collisional ionization in titanium ion beam generation.

For each laser pulse duration, a target thickness scan was executed in order to determine

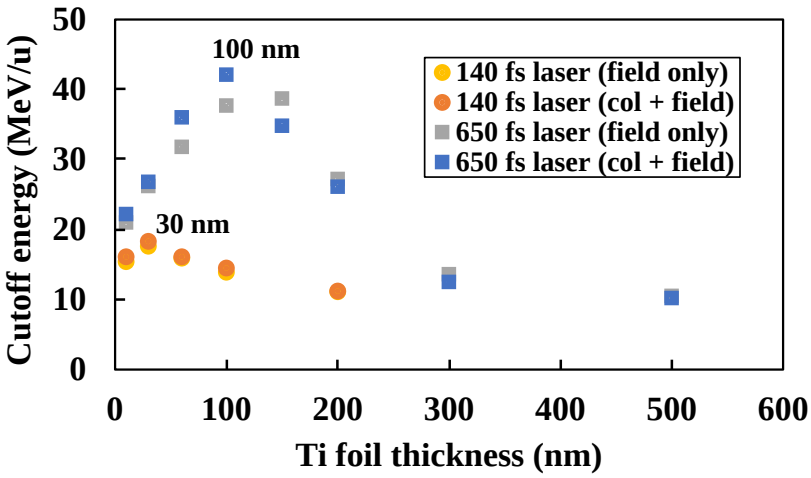

Figure 6.2: Titanium cutoff energies per nucleon as a function of target thickness, with the optimum thicknesses labeled for cases where both field and collisional ionization were included in the simulation. At the optimum thickness, the target transparency onset occurs at or near to the peak of the laser pulse. Thinner targets become transparent too early, and thicker targets favor the TNSA mechanism. Collisions play a larger role in the 650 fs laser-plasma interaction because the longer interaction time allows for more collisions to occur. These data were extracted at the end of the simulation: at 333 fs for the 140 fs case, and 1.0 ps for the 650 fs case.

the optimum thickness for maximizing titanium ion energy, as shown in Figure 6.2. The optimum thickness exists because electrons can be the most efficiently heated in the target bulk when the laser peak incidence is concurrent with target transparency [40, 150, 151, 152, 153, 154, 155, 43, 156]. Although the intensity is the same for both the 140 and 650 fs lasers studied here, the difference in pulse duration is responsible for the difference in optimum thickness. A shorter laser pulse will ramp up to its peak faster, and therefore the target must be thinner in order to go transparent earlier in time. If the target is too thin — $<$ 30 nm for the 140 fs laser, and $<$ 100 nm for the 650 fs laser — it becomes transparent too early for the peak of the laser pulse to heat the target bulk. For targets thicker than these optima, the delay or even elimination of target transparency favors the less efficient TNSA mechanism. For the 140 fs laser pulse, collisions do not affect the optimum thickness: it remains 30 nm regardless of whether or not collisions are included. However, there is a slight shift in the 650 fs laser optimum, as collisions have more time to occur during the longer laser-plasma interaction, increasing the ion charge. For a given target

thickness, the collisional case will go transparent slightly later in time, as the contributions of collisional ionization increase the electron density. The optimum target thickness is 150 nm with field ionization only, and 100 nm when collisional ionization is included. Though this shift is the most pronounced for the thickness optima, it affects all target thicknesses, favoring collisions in the transparency regime ($\leq$ 100 nm), and damping in the TNSA regime ($>$ 100 nm). In general, the 650 fs laser generates higher energy titanium than the 140 fs laser, as the longer laser pulse has more energy because the intensity and spot size are fixed laser parameters. In the following section, we analyze the mechanisms responsible for optimum titanium acceleration. Leading up to transparency, hole-boring RPA is followed by SWA. These two mechanisms cause the TNSA sheath field to act on pre-accelerated titanium, maximizing the titanium energy, in a scheme known as enhanced TNSA [4].

6.2 Determining the mechanisms of titanium acceleration

For both laser pulse durations, TNSA emerges as the dominant titanium ion acceleration mechanism. However, there are brief stages of other acceleration mechanisms that enhance the TNSA process. The laser drives these intermediate stages of ion acceleration regardless of whether collisional processes are included. In both cases, it is evident that the target transparency onsets around the time the laser peak hits the target (defined here as t' = 0 fs). Additionally, regardless of pulse duration, the sequence of acceleration mechanisms is the same, as determined via 1D lineouts along the laser axis. The extraction region is a rectangle bounded in x by the limits of the simulation domain, 0 to 30 μm. The y-boundary is $\pm$2.5 μm from the laser axis, which is equal in width to the FWHM laser spot. This region was chosen to investigate the detail of the acceleration mechanisms taking place along the laser axis for the optimum cases with collisions for each pulse duration: the 140 fs laser pulse on the 30 nm target, and the 650 fs laser pulse on the 100 nm target.

For the 140 fs laser, when the laser peak reaches the target (time t' = 0), the target has yet to go transparent. Figure 4a illustrates that the laser pulse oscillation in the y-direction cannot yet penetrate the overdense target at 36.8 fs (Figure 6.3a). The initial opacity of the target agrees with an estimation of the relativistic skin depth, in which a foil target is assumed to be composed of Ti^{20+}, the dominant charge state estimated by the ADK model. The skin depth of $c/\omega_p \approx 20$ nm is near the 30 nm optimum thickness determined in the previous section, indicating that this is the domain where volumetric heating is the most efficient.

The radiation pressure of the laser pulse pushes the electrons forward and drives a charge separation between electrons and ions within the target, giving rise to a spike in the longitudinal electric field (Figure 6.3b). This field produces a momentum spike in the phase space within the target bulk (Figure 6.3c), distinct from the smooth phase space profile characteristic of TNSA [12], clearest in the 5.5 – 6.5 μm region of Figure 6.3i. The electron cloud continues to expand 6.7 fs later, though the laser has yet to break through the target (Figure 6.3d). The radiation pressure front moves through the target during the expansion, and a shock is generated, as suggested by the flattening of the phase map within the target (Figure 6.3f). At 63.4 fs, relativistic transparency allows the laser to penetrate the overcritical target (Figure 6.3g). The longitudinal electric field along the laser axis dampens (Figure 6.3h). The shock has dissipated, and the radiation pressure front has reached the rear surface of the target. The injection of radiation-pressure ions into the sheath field of the TNSA enhances the energy of the ions. The phase map continues to smooth as RIT-enhanced TNSA dominates over the other acceleration mechanisms (Figure 6.3i).

Only high charge titanium, namely Ti^{20-22+}, is generated along the laser axis. All lower charge states are short-lived, as the combination of the laser field and the strong longitudinal fields within the plasma drive the ions to higher charge states. Ti^{22+} dominates the expansion on the front side of the target, as this is where the incident and reflected laser fields combine to generate a total electric field strong enough to fully strip titanium of all its electrons. As TNSA takes over at 64.3 fs, Ti^{20+} dominates the expansion on the target rear. Note that this expansion is

in agreement with the energy spectra for multiply charged ions discussed in Figure 6.6 of Section 6.3, where Ti^{20+} is the most populous and most energetic charge state.

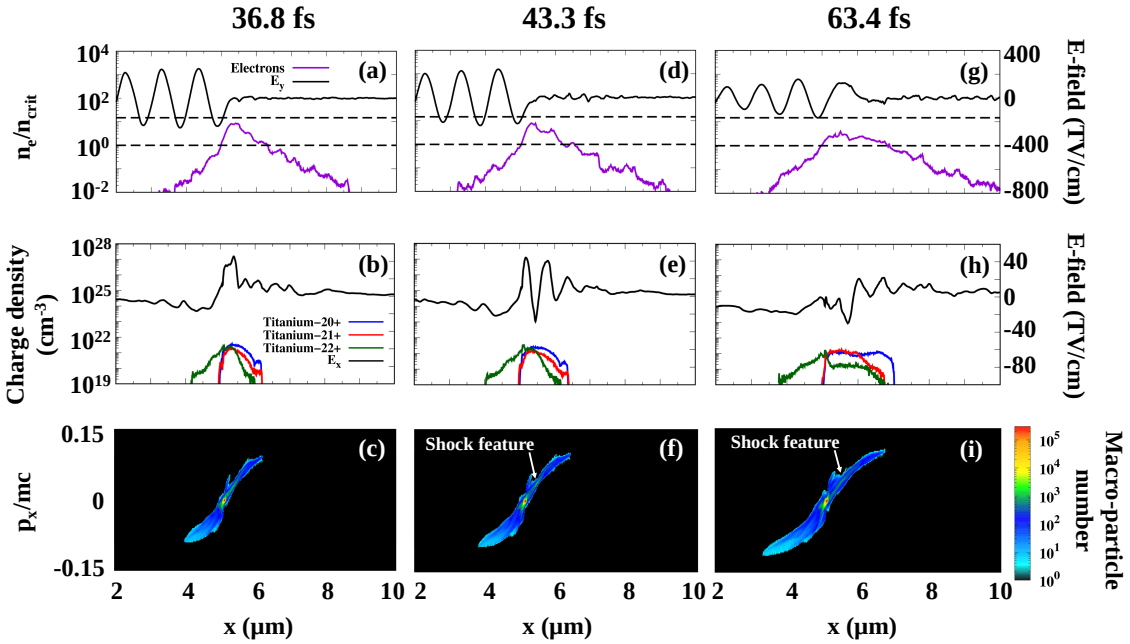

Figure 6.3: 1D lineouts detailing the mechanisms of the 140 fs laser interacting with the optimum foil thickness (30 nm). Time *t'* = 0 is defined as the time the laser peak reaches the front surface of the foil at 5.0 μm. The dashed line at n/n_{crit} = 1 represents the classical critical density, and n/n_{crit} = 14.76 represents the relativistically corrected critical density for electrons with $\gamma_{max} = (1 + a_0^2/2)^{1/2}$. Figures a-c demonstrate that radiation pressure takes place before transparency, and d-f show the shock that arises shortly after. Figures g-i show that the radiation pressure front has moved to the rear surface to enhance TNSA.

For the 650 fs pulse duration, the mechanisms are the same, though there are a few key differences in the process, as a result of the much longer laser-plasma interaction time. -146.7 fs before the laser peak reaches the target, the target is opaque to the laser field (Figure 6.4a). The radiation pressure of the laser drives a longitudinal electric field within the target bulk (Figure 6.4b). Trace amounts of Ti^{19+} remain there at this time, but are soon ionized to higher charge states as the laser field continues to rise. Although the rear surface is expanding, the front surface, now ionized to Ti^{20-22+}, retains a steep gradient due to the radiation pressure. The radiation pressure causes a kink in the phase map within the target at 5.0 μm, further indicating that TNSA

is not the only acceleration mechanism at this time (Figure 6.4c). The target transparency occurs 120 fs later, as the target expands and the electron density lowers (Figure 6.4d). The front surface also expands, which is composed solely of Ti^{22+} due to the strong laser field here (Figure 6.4e). Ti^{20+} expands the furthest along the rear side, as the electric fields here are not strong enough to produce similar populations of Ti^{21-22+}. At this same time, the rising laser pulse drives a shock within the plasma, which causes another spike in the longitudinal electric field. This field spatially corresponds with a sharp stairstep in the phase map (Figure 6.4f), indicating a quasi-monoenergetic population of titanium. Unlike the 140 fs optimum case, where the target flattening is a very narrow region, the 650 fs laser pulse drives a shock that persists longer in time. This stairstep region between 5 – 6 μm resembles the phase map characteristic of laser-driven shock acceleration from overdense plasmas as identified by Macchi, et al. [38]. Macchi showed that the shock piston velocity can be estimated using conservation of momentum via the formula $u_p = a_0 c \sqrt{\frac{Z}{A}\frac{m_e}{m_p}\frac{n_e}{n_c}}$. For L-shell titanium, a conservative estimate yields a shock velocity of $\sim$0.04c, and ions can be accelerated up to twice the shock velocity. This estimate agrees with the flat-top ion population seen in Figure 6.4(f), where the ions move with velocity $\sim$0.07c.

The laser peak then reaches the target at t'=0 fs, and 33.3 fs later, the target is fully transparent (Figure 6.4g), indicating the end of the radiation pressure stage. The strong longitudinal field spikes dissipate, and the number of Ti^{22+} ions increases in the forward direction (Figure 6.4h). The phase map smooths as RIT-enhanced TNSA takes over (Figure 6.4i), yet the signature of the shock stairstep remains as this quasi-monoenergetic population moves forward in space. In the following section, we show that this shock population remains intact until the end of the simulation, and is responsible for the quasi-monoenergetic peak of Ti^{20+}, centered on 5 MeV/u (Figure 6.6c-d).

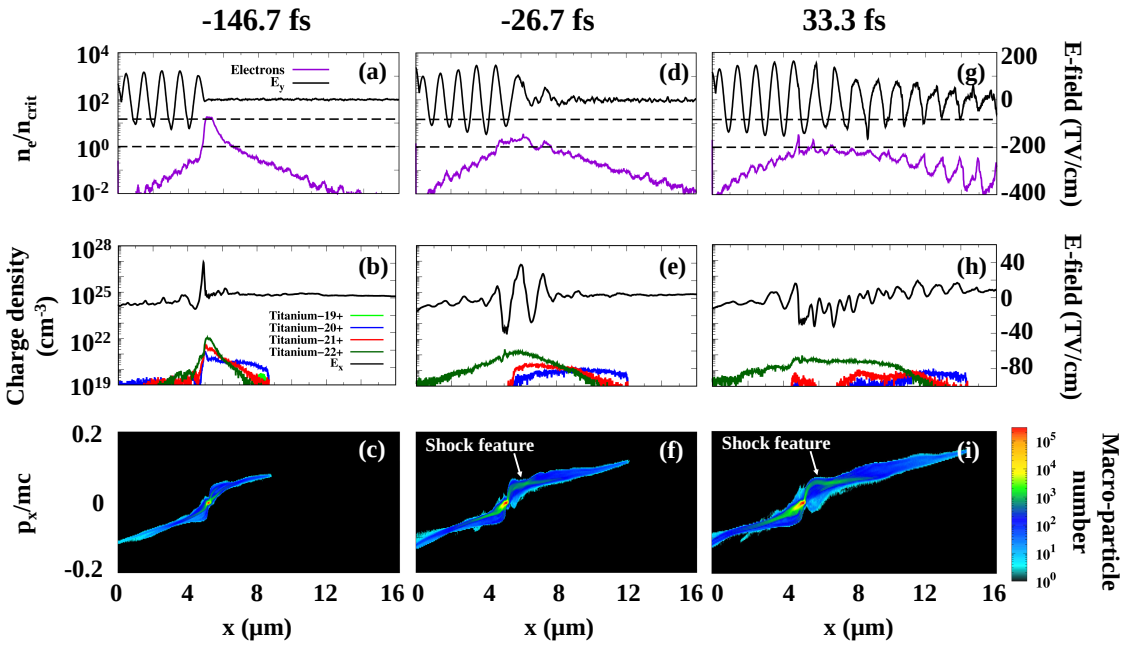

Figure 6.4: 1D lineouts detailing the mechanisms of the 650 fs laser interacting with the optimum foil thickness (100 nm). Time *t'* = 0 is defined as the time the laser peak reaches the front surface of the foil at 5.0 μm. The dashed line at n/n_{crit} = 1 represents the classical critical density, and n/n_{crit} = 14.76 represents the relativistically corrected critical density for electrons with $\gamma_{max} = (1 + a_0^2/2)^{1/2}$. Figures a-c indicate that radiation pressure takes place before transparency, and d-f show the shock that arises just as transparency begins. Figures g-i show that the radiation pressure front has moved to the rear surface to enhance TNSA. A distinct shock feature remains in the phase map (i) at 5 – 6 μm.

6.3 Charge properties of the titanium ion beam

The charge distribution in a mid-Z ion beam is more complex than the more commonly studied proton and carbon beams, as these low-Z species are easily stripped by lasers of intensity $> 10^{19}$ W/cm^2 [83]. Ions with the highest q/m ratio, namely Ti^{22+} are not necessarily the most dominantly accelerated, even if this charge state is present in all optimum cases. High charge state titanium takes a longer time to be generated on the rear side, and is preferentially generated on the front side before target transparency takes place (Figures 6.3-6.4e).

For both pulse durations, collisional ionization increases the population of Ti^{21-22+} accelerated in the forward direction by approximately one order of magnitude, as shown in Figure

6.5. Lower charge states ($\leq Ti^{14+}$ for the 140 fs laser, and $\leq Ti^{16+}$ for the 650 fs laser) are excited to higher ionization states via collisions. Though Ti^{20+} remains dominant with the 140 fs case regardless of collisions, with the 650 fs laser, Ti^{20+} and Ti^{22+} reach equal counts, with Ti^{21+} not far behind. Although the extraction condition shows all ions accelerated in the forward direction, most lower q/m ions are neither energetic nor populous enough to affect the energy spectra.

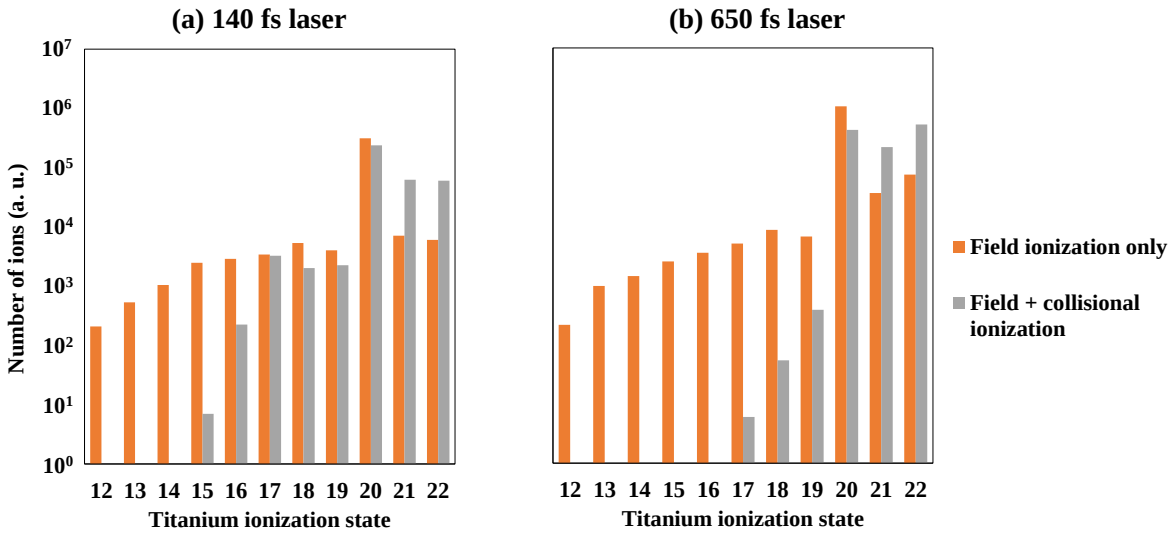

Figure 6.5: Distribution of titanium ionization states of ions accelerated in the forward direction ($\pm 90^\circ$ from target normal), for the 140 fs laser (a) and the 650 fs laser (b). In both cases, collisional ionization shifts the ions to higher charge states. Ionization energies for the K-shell are relatively high [162], resulting in the charge state build-up at Ti^{20+}. No charge states below Ti^{12+} were observed. These data were extracted at the end of the simulation: at 333 fs for the 140 fs case, and 1.0 ps for the 650 fs case.

The energy spectra of the titanium can be decomposed into individual charge states, which is depicted in Figure 6.6. For both pulse durations, Ti^{20+} is dominant for all cases, with the notable exception of the 650 fs laser with collisions (Figure 6.6d). Here, the energy distribution of Ti^{21-22+} converges with that of Ti^{20+} above 10 MeV/u. Quantitatively, including collisions in the simulation increases the conversion efficiency of Ti^{21-22+} for energies > 10 MeV by $20\times$. In this case, > 10 MeV Ti^{20-22+} all occupy similar energy distributions, whereas in all other cases, Ti^{20+} ions are preferentially accelerated. The dramatic increase in Ti^{21-22+} generation is

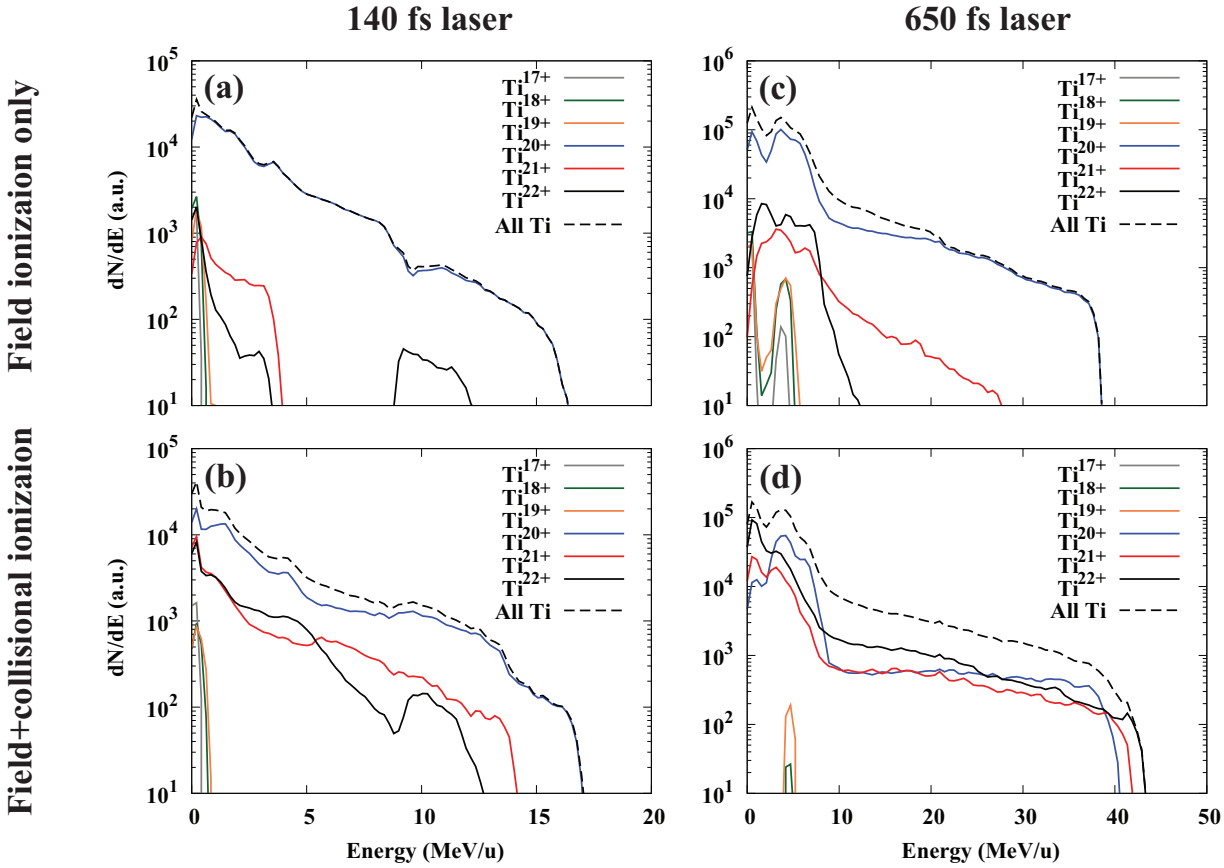

Figure 6.6: Energy spectra for the forward-accelerated charge states from 30 nm foils (a-b), and 100 nm foils (c-d) for each laser case. In both laser cases, the energy spectra of Ti^{21+} and Ti^{22+} are enhanced when collisions are turned on. For the 650 fs laser, collisions nearly eliminate the number of accelerated ions $\leq Ti^{20+}$, and increase the prominence of the quasi-monoenergetic peak of Ti^{20+} at 5 MeV/u. These data were extracted at the end of the simulation: at 333 fs for the 140 fs case, and 1.0 ps for the 650 fs case.

responsible for boosting the cutoff energy by $\sim 15\%$. However, for the total titanium spectrum (represented by a dashed line in Figure 6.6c-d), the difference in conversion efficiency is $< 1\%$.

The lower energy part of the spectrum shows a strong quasi-monoenergetic peak centered on 5 MeV/u. The energy of this peak corresponds with the shock acceleration feature observed in Figure 6.4. This same peak is seen without collisions (Figure 6.6c), but it is of a much lower prominence. For this pulse duration, collisions also decrease the number of titanium charge states accelerated in the forward direction. Without collisions, Ti^{17-19+} reach a few MeV/u, but with collisions, these charge states are nearly eliminated.

Collisions have a much smaller effect on the energy spectra accelerated from the shorter pulse laser (Figure 6.6a-b). The spectrum of Ti^{17-19+} shows no dependence on collisions, albeit this component of the spectrum is of very low energy, < 1 MeV/u. There is enhancement of Ti^{21+} and Ti^{22+} up to 14 and 13 MeV/u, respectively, but the energy and counts are still too low for these charge states to compete with Ti^{20+}. In addition, the shock acceleration stage seen in Figure 6.3 is too short-lived with the 140 fs laser to produce any signatures within the energy spectra.

As evident by the energy spectra of the multiply charged ions, turning on collisions dramatically changes the ionization dynamics in the 650 fs laser-plasma interaction. Figure 6.7 shows a 2D map which provides insight into the effect of collisions on the ionization and acceleration of various charge states. In the collisionless case (Figure 6.7a), approximately 300 fs before the laser peak reaches the target, much of the remaining target is of a low charge state, at $\leq Ti^{15+}$. The expanding plasma around the wings is dominantly Ti^{16-19+}, and along the laser axis, Ti^{20+} is the dominant state. The combination of three electric fields – the laser field, the laser field reflected from the critical surface, and the sheath field – ionize trace amounts of Ti^{20+} to Ti^{21-22+} on the front surface. By the time the laser peak reaches the target at $t' = 0$ fs, a well-defined jet of Ti^{21-22+} begins to form, and is accelerated in the forward direction by RIT-enhanced TNSA (shown here in Figure 6.7b at 133.3 fs). However, Ti^{20+} remains the dominantly accelerated titanium species in the forward direction.

When collisions are included in the simulation, $\leq Ti^{15+}$ species are no longer present at -166.7 fs, and more Ti^{21-22+} is generated along the laser axis (see Figure 6.7c). The laser-plasma interaction continues to generate Ti^{21-22+}, as transparency onsets (Figure 6.7d). We estimate that, near the laser peak, the transition from Ti^{20+} to Ti^{22+} takes $\sim$100 fs. Ti^{20+} reaches closest to the right edge of the simulation domain at this time, showing that it was generated and accelerated before Ti^{21-22+}, even though its q/m ratio is lower. Ti^{20+} also remains dominant within the intact portion of the target, as well as farther away from the laser axis.

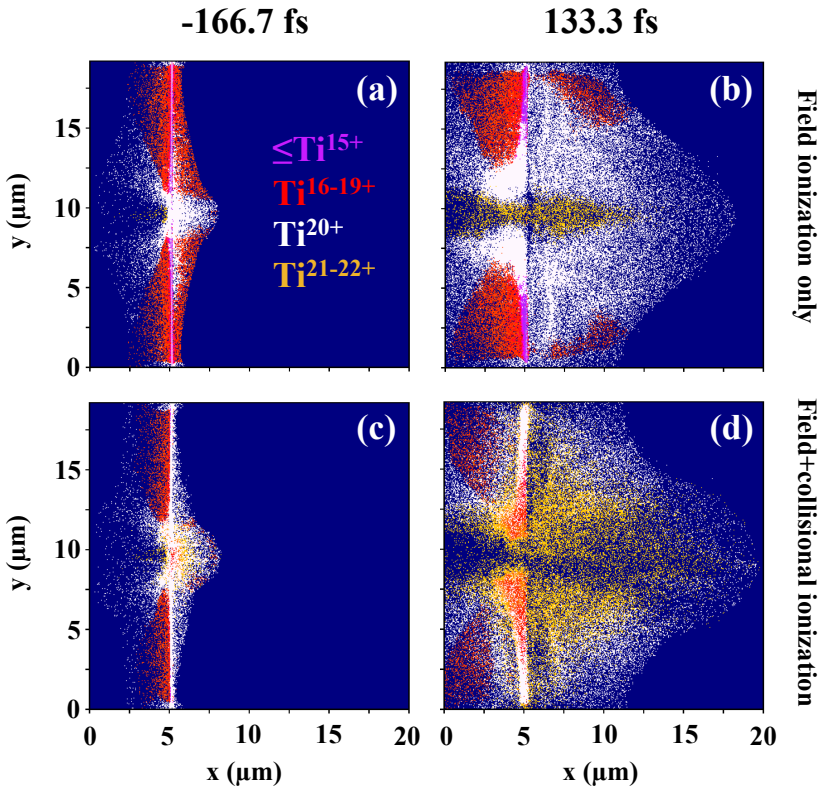

Figure 6.7: Scatter plots for the charge states generated from the 650 fs laser incident on the 100 nm foil. In the case with only field ionization (a-b), Ti^{20+} is the preferentially accelerated charge state, surrounding a collimated beam of Ti^{21-22+} along the laser axis. Charge states $\leq Ti^{19+}$ are dominant along the wings of the target. When collisions are included in the simulation (c-d), the wings are ionized to Ti^{20+}. Ti^{21-22+} is generated within the target bulk, and the forward accelerated population dominates near the laser axis.

6.4 Summary

Laser-acceleration of titanium ions was investigated for a laser of fixed intensity (6.0×10^{20} W/cm^2) with two pulse durations (140 and 650 fs). The choice of a mid-Z material was motivated by the ability to show the interplay between field and collisional ionization, which is far less pronounced, or possibly absent, in the acceleration of low-Z materials such as carbon. The interaction was studied over a wide range of foil thicknesses (10 – 500 nm), with an optimum thickness of 30 nm for the 140 fs laser, and 100 nm for the 650 fs laser when collisions are accounted for. In both cases, TNSA is the dominant mechanism at the thickness optima, though

other acceleration mechanisms contribute to its enhancement. A brief stage of hole-boring RPA, followed by a shock wave, work together to inject energetic titanium ions into the sheath field on the rear side of the target.

The mechanisms of ion acceleration are independent of collisions. In the 650 fs pulse case, collisions play a more significant role because the laser-plasma interaction is $\sim 5\times$ as long. However, for the 650 fs laser, including collisions decreases the optimum thickness from 150 nm to 100 nm for the following reasons. Collisional ionization increases the electron density, which delays the time of transparency. To compensate, the optimum thickness is reduced by 50 nm. In addition, collisions dramatically improve the conversion efficiency of highly energetic, highly charged titanium ions, boosting the yield by $20\times$ for Ti^{21-22+} with energies > 10 MeV/u. As a result, collisions enhance the maximum energy of titanium ions by $\sim 15\%$. Collisions also increase the prominence of the quasi-monoenergetic peak of Ti^{20+} centered on 5 MeV/u.

This study is of particular relevance to the previous work of J. Li, et al. [163], which studied titanium foils irradiated by a 650 fs laser pulse length. The authors used near-identical parameters to our longer pulse case studied here ($a_0 = 20.82$, $\tau_{FWHM} = 650$ fs), and assumed field ionization was the sole ionization mechanism. Through both experimental data and simulation data generated using the EPOCH code [86], titanium acceleration from ~ 100 nm foils in the RIT regime was observed, consistent with the results presented here. In addition, they identified that self-generating fields can further accelerate the ion beam picoseconds after the laser-plasma interaction has ended. Multi-picosecond simulations require extensive computational resources, so these effects were not studied in this work due to the resources demanded by the thickness scan. Hence, the role of collisions in the production of these self-generated fields is a topic of future numerical study.

For mid-Z ion acceleration with near-ps lasers, field ionization remains the dominant mechanism, but collisions begin to play a significant role in ion beam generation. High charge states of heavy ions are essential for localized energy deposition, which is important for heavy

ion heating of warm dense matter [164]. Highly charged ion sources can also decrease the size and running cost of large-scale accelerators, as the injected ions can be highly ionized and highly energetic (tens of MeV/u) [165]. We have shown that for a near-ps laser incident on a mid-Z foil, both field and collisional ionization are essential in generating highly ionized, energetic ion beams. Future investigation will expand upon the interplay of ionization mechanisms, laser pulse length, and the dynamics of heavy ion acceleration.

6.5 Acknowledgements

Chapter 6 contains a partial reprint as it appears in J. Strehlow, D. Kawahito, M. Bailly-Grandvaux, F. N. Beg, and G. M. Petrov. "The effects of laser pulse length and collisional ionization on the acceleration of titanium ions." *Plasma Physics and Controlled Fusion* 63, 065011 (2021). The dissertation author is the primary investigator and author of this paper. This material is based on work supported by the Department of Energy, National Nuclear Security Administration (NNSA) under Award Number DE-NA0003842. JS is partially funded by Sandia National Labs which is managed and operated by National Technology & Engineering Solutions of Sandia, LLC, a subsidiary of Honeywell International, Inc., for the U.S Dept. of Energy's National Nuclear Security Administration under contract DE-NA0003525. GP wishes to acknowledge financial support from Naval Research Laboratory 6.1 Base Program.

Chapter 7

Conclusions and future work

Among the body of work conducted by the author, the common theme is optimizing ion acceleration via a study of laser and target parameters. In order to evaluate the ion beams generated in experiments, it is important to have the detectors calibrated for absolute counts. In summary, for this first project, described in Chapter 4, the author extended the repository of peer-reviewed imaging plate calibrations into the mid-Z regime. The author then compared his work to other published calibrations to suggest that IP response can be estimated for any arbitrary mid-to-high-Z species (Figure 4.8). Recent progress in this area has been highlighted in Section 7.1, describing the author's interest in extending these results.

The role of pulse length has been shown to play a role in ion acceleration in both the ultrathin target regime and the enhanced TNSA regime with microstructures (Chapters 5-6). However, the pulse length dependence is for different reasons. For the former case, collisions play a significant role for a sufficiently long pulse length ($\gtrsim$ 200 fs) in volumetric acceleration. Including collisions in the simulation changes the evolution of the multiply charged ion beam, favoring fully stripped titanium ions over the otherwise dominant Ti^{20+}. For the experimental study with microstructured targets, the foil substrate is 1 μm, which is too thick to be volumetrically accelerated. The role of the pulse length for a fixed intensity is if it is too

long, it shutters the tubes before the peak of the laser pulse can interact with the structures. With respect to a fixed pulse duration but higher intensity, the corresponding larger pre-pulse can also shutter the microtube before the main pulse arrives, meaning it does not outperform a flat target. Due to computational resource constraints, the numerical work presented in this dissertation is all conducted in 2 dimensions. Hence, it is of great interest to the author to explore this limitation, as for PIC simulations to best replicate experimental results, they should be benchmarked.

Chapter 6 identifies ion acceleration regimes where collisional ionization is and is not negligible. This is beneficial for the numerical study of collisions in the generation of multiply charged ions, as well as determining when collisions can be omitted to preserve computational resources. However, this should still be studied in experiments to ensure that including collisions match experimental results in heavy ion acceleration. Two avenues for validating the collisional models in PIC simulation are comparing the ionization distribution with and without PIC. Practically speaking, this can be done by comparing the proportions of multiply charged ions measured on a Thomson parabola to the proportion extracted from a PIC simulation (see for example Figure 6.5). In addition, PIC simulations indicate that including collisions significantly modifies the energy spectra for multiply charged ions (Figure 6.6, which would be immediately evident from a Thomson parabola analysis.

As discussed in Chapter 5, running PIC simulations in 3D for ps laser-plasma interactions is prohibitively demanding on resources. However, in a direct comparison with 2D and 3D simulations, Wang et al. [166] have shown that 2D simulations overestimate electron and photon energies and collimation. Though 2D simulations are notorious for overpredicting the beam quality of laser-driven radiation sources, this study has not yet been benchmarked with experimental results. MeV photons generated from conventional accelerators have seen tremendous success in radiographing dense, high-Z materials. However, their large ($\sim$mm) spot size and $\sim$ns pulse duration limit their probing of finer features for both static and dynamic imaging. If PIC can reliably predict the laser requirements for driving quality MeV photon beams,

it can enable the first commercial application of PW lasers, as the spot size and duration of these sources is on the order of the laser pulse [149]. Section 7.3 presents an upcoming experiment by the author to achieve this goal.

7.1 Calibrating image plates to energetic ions

Since the author completed the work described in Chapter 4.2 in 2019, several articles have been published extending this area of research. Lelasseux and Fuchs (2020) [167] have developed a model attempting to comprehensively describe the response of any arbitrary ion to a TR-type imaging plate (IP). Using Birks' law, developed for organic scintillators, the authors fit the parameters for various published IP calibrations, in the form

$$A\int_0^W \frac{\frac{dE}{dz}(E,z)}{1+B|\frac{dE_{dep}}{dz}|}e^{-z/L}dz \tag{7.1}$$

where W is the thickness of the active layer and A and B are the constants of fit. Unfortunately, the fit for low-Z ions breaks down in the mid-Z regime (Figure 7.1). In a future experiment on heavy ion acceleration, the author intends to field several shots with CR-39 to conduct additional calibrations and test their fits in the same manner as Lelasseux and Fuchs.

Nishiuchi, et al. [168] followed with several calibrations on the SR-type, and show that after penetrating the active layer, the IP response to energetic ions is largely independent of energy, and the authors argue the need for future calibrations is now negated. As shown in Figure 7.2, the IP sensitivity is roughly constant for ions heavier than carbon (Z>6). This transition region could explain the breakdown of the methods of Lelasseux and Fuchs. This trend is in approximate agreement with the power law fited in this thesis in Figure 4.9.

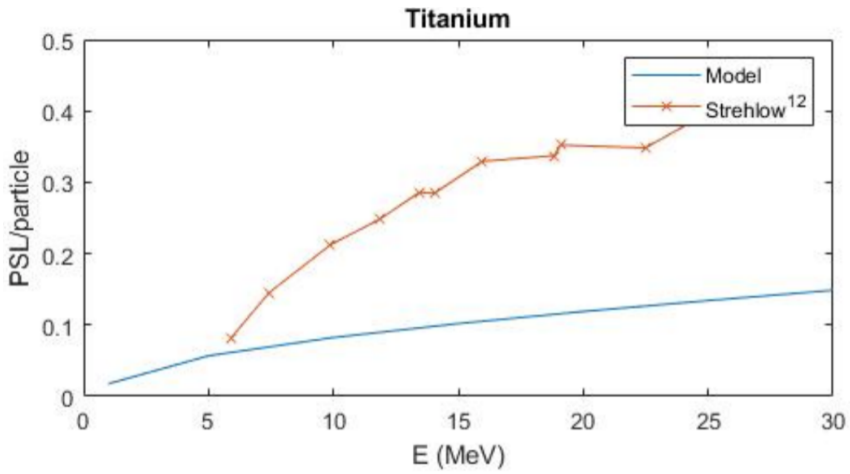

Figure 7.1: A strong fit to the IP calibration with low-Z ions breaks down in the mid-Z regime. Figure courtesy of Ref. [167].

7.2 The role of dimensionality in flat and structured targets

In Chapter 6, analysis is presented on acceleration mechanisms from ultrathin, mid-Z targets. In summary, the three stages of acceleration are: hole-boring radiation pressure acceleration (HB-RPA), followed by shock wave acceleration (SWA), which work to inject fast ions into a sheath field characteristic of enhanced TNSA. The optimum thickness occurs when the laser transparency time is concurrent with the peak intensity of the laser pulse reaching the target, in good agreement with prior studies in the relativistically induced transparency (RIT) regime. However, there are several other ion acceleration mechanisms in the RIT regime, most notably breakout afterburner (BOA) [4]. In BOA, a fluid instability is responsible for accelerating a volumetric population of ions [42], and favorably accelerates ions off-axis. BOA has largely been studied rigorously in 3D simulations [41], though the mechanism was first predicted in a single dimension [4]. Several open questions remain at the intersection of RIT processes, ionization processes, and simulation dimensionality. Firstly, is there a dimensional effect that impacts BOA in the mid-Z regime? In addition, are mid-Z ions not favored by the BOA mechanism? The author of this thesis would like to extend to a material study of ion acceleration, with and without collisions, to discuss further transitions in ion acceleration mechanisms. It would be pertinent to

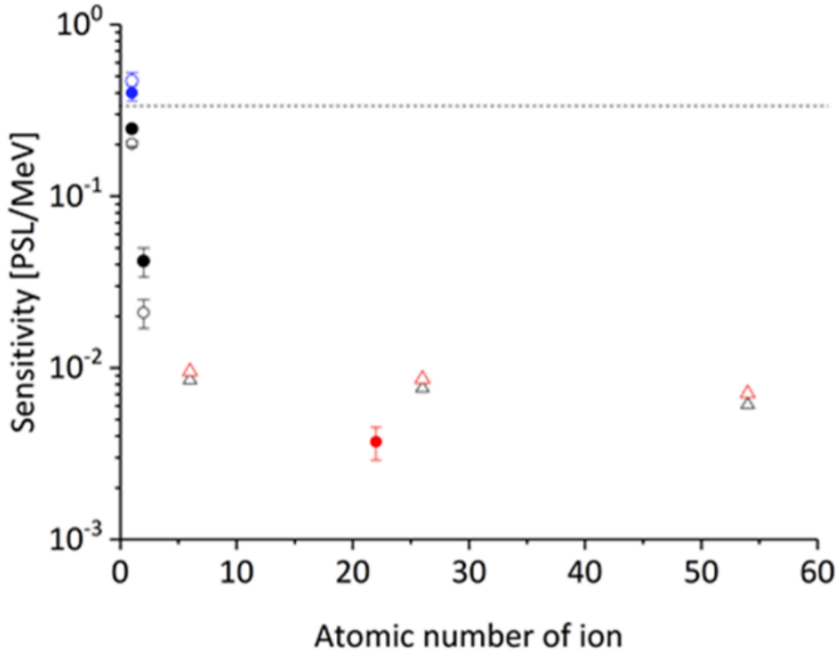

Figure 7.2: The IP sensitivity flattens out for mid-Z ions and beyond. The black dashed line represents the constant sensitivity for MeV electrons, and the red circle at Z = 22 represents the calibration presented this thesis. Figure courtesy of Ref. [168].

the field as BOA has not been observed accelerating ions heavier than carbon [43].

On a similar note, the limitations of 2D simulation have recently been elucidated for a fs laser interacting with a microtube targets. In Wang, et al. (2021) [166], the authors show that 2D can qualitatively reproduce the features of 3D simulations, but overestimates the maximum electron energy and conversion efficiency (Figure 7.3). The 30 fs laser pulse used in the simulation is not cost prohibitive to study, but replicating this work to ps laser-plasma interaction would be difficult. However, a compromise can be reached with 2D cylindrical simulations, a capability of the OSIRIS code [169]. 2D cylindrical can be thought of as "quasi-3D", and replicating this study with a 30 fs laser, as well as a 140 fs laser (representative of TPW) is a planned pursuit. This future study would also include ion generation from a $\sim$1 μm foil superimposed on the rear of the tube, representative of the targets studied in Chapter 5.

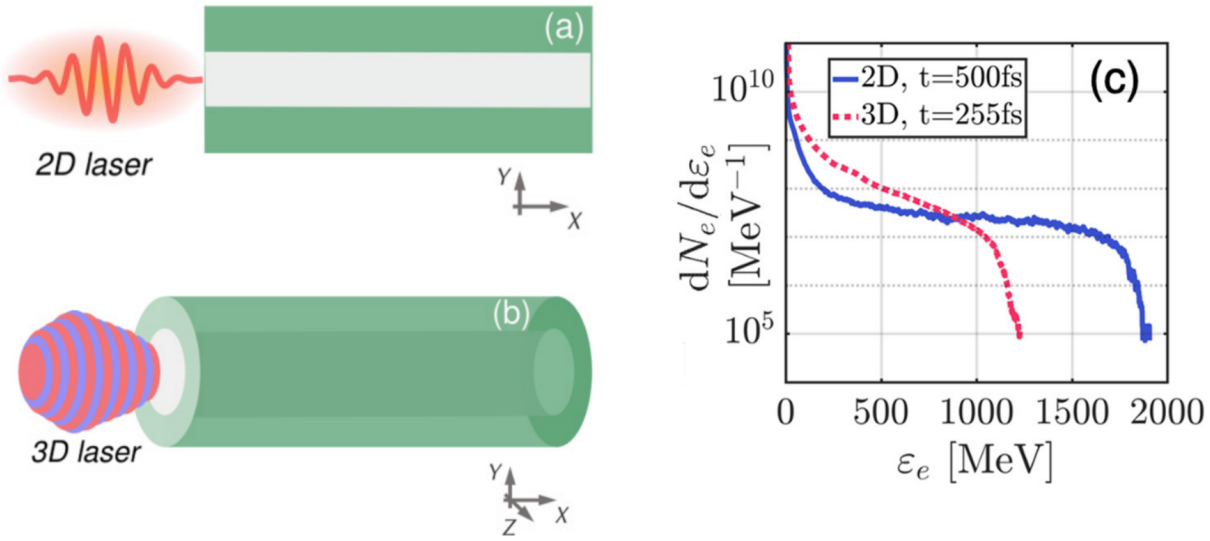

Figure 7.3: 2D vs 3D geometries (a & b, respectively) of a laser pulse incident on a microtube. Resultant spectra from each case shown in (c), assuming a laser intensity of $\sim 10^{22}$ W/cm^2 with a 30 fs pulse length. Figure adapted from Ref. [166].

7.3 Structured targets for γ-ray generation

Photons of MeV energies, or γ-rays, rely on hot electron generation, much like ion acceleration in the TNSA and RIT regimes. One avenue to converting energetic electrons into photons is with a dense "catcher" material, such as an electron beam directed into several mm of tungsten. Due to conservation of momentum, MeV electrons emit MeV photons when stopped in the material. With a laser-driven system, this process can be compactified into a single stage, with a laser incident on a tungsten target. Hot electrons generated at the front surface will travel through the mm-thick target, emitting γ-rays in the same manner. Like TNSA, γ-ray generation can be enhanced with surface structures [111, 170].

Because a PW-class laser can be focused down to a few μm spot, the γ-ray source size will not be much larger. A matrix comparing laser-driven sources to conventional x- and γ-ray sources (Figure 7.4) shows the superior spatial resolution of a laser-driven source. In addition, its pulse duration is 5 orders of magnitude smaller, which is of benefit for dynamic experiments. Figure 7.5 shows the resultant spectra from these sources, with Trident-like parameters (80 J,

Application	Target optical depth	Current state-of-the-art	Dose	End-point x-ray energy	X-ray Spot Size	X-ray pulse duration
Static (NDT)	Variable	LANL Microtron, commercial Linacs and tubes	Variable up to 10,000R/min at 1m*	0.03-20MeV**	~1 μm (<225keV); ~1mm (>225keV); << 1mm strongly desired	(Not a critical parameter for NDT)
Dynamic	Thin	Febetron	0.5 R at 1 m	<2.1 MeV	~1mm	~200ns
Dynamic	Intermediate	Cygnus	4 R at 1 m	<2.2 MeV	~1mm	~200ns
Dynamic	Thick	DARHT	100s of R at 1 m	1-20 MeV	~1.5mm	~200ns
Static/Dynamic	**Variable**	**High-power-laser**	**2.2 R at 1 m**	**1-20 MeV tunable**	**<<100μm (!)**	**~1ps**

Figure 7.4: Comparison of conventional energetic photon sources for radiography, along with laser-driven sources (highlighted). Note that the figure does not explicitly draw the line between x-rays and γ-rays. Figure courtesy of Ref. [171].

650 fs, 6×10^{20} W/cm^2) outperforming the CSU ALEPH laser (10 J, 45 fs, 3×10^{21} W/cm^2). However, the DARHT facility generates an order of magnitude more photons, indicating it is superior for probing larger length scales of material, at the expense of lower resolution.

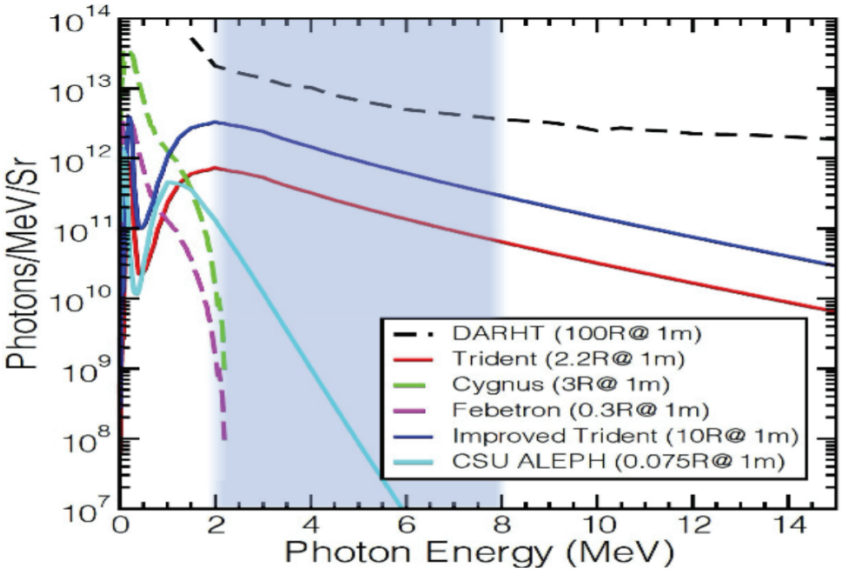

Figure 7.5: Comparison of MeV photon spectra from various sources, with the shaded area showing the ideal region for radiography of special nuclear materials. Figure courtesy of Ref. [171].

In order to commercialize a PW laser system to fill this niche, improved understanding of γ-ray scaling with laser parameters is needed. An experiment at TPW is being planned to

explore this parameter space. The laser energy will be varied from 30 - 120 J incident on foam and nanowire targets, which will be engineered directly onto tungsten disks. Flat disks will also be shot at to benchmark performance. The 6" disk can afford thousands of shots, as it can be translated and rotated as shown in Figure 7.6. Figure 7.6 also shows the diagnostic suite. On the front side, a MACOR screen will scatter reflected laser light, which will be captured with a CCD to measure absorption. The MACOR has line-of-sight holes drilled for EPPS and fiber spectrometer measurements. On the rear side, a deflection magnet sweeps away charged particles in order to lower the background on the γ-ray spectrometer and radiographic suite. To measure forward escaping electrons, the magnet will be removed and the γ-ray spectrometer replaced with an EPPS.

This project is a natural extension of the author's thesis work as relativistic transparency and direct laser acceleration are expected in the target structures. In addition, with such thick, high-Z materials, collisional processes certainly play a role in the generation of secondary radiation. Ensuring that the simulations are comprehensive is essential in predicting the laser parameters necessary for commissioning a PW for its first industrial application.

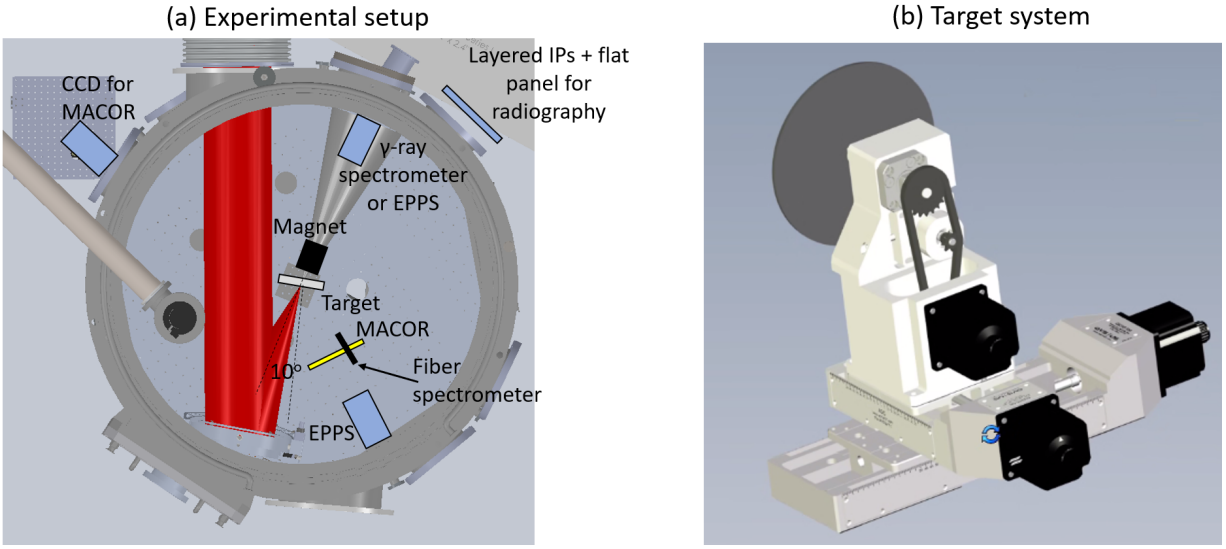

Figure 7.6: (a) Proposed experimental setup at TPW. The primary objective is understanding γ-ray scaling with laser energy and intensity. (b) The target is a 3 mm thick W wheel with x-y and rotational motion. Target structures will be engineered directly onto the wheel.

Bibliography

[1] M. C. Kelley, *The Earth's Electric Field: Sources from Sun to Mud*. Newnes, 2013.

[2] R. P. Drake, "Introduction to high-energy-density physics," in *High-Energy-Density Physics*, pp. 1–20, Springer, 2018.

[3] J. Daligault and T. Sjostrom, "Dense plasma theory: The physical regimes," Los Alamos National Laboratory, Public Release (Accessed Jan 2022).

[4] L. Yin, B. Albright, B. Hegelich, and J. Fernández, "Gev laser ion acceleration from ultrathin targets: The laser break-out afterburner," *Laser and Particle Beams*, vol. 24, no. 2, pp. 291–298, 2006.

[5] F. Fiúza, A. Stockem, E. Boella, R. Fonseca, L. Silva, D. Haberberger, S. Tochitsky, C. Gong, W. B. Mori, and C. Joshi, "Laser-driven shock acceleration of monoenergetic ion beams," *Physical Review Letters*, vol. 109, no. 21, p. 215001, 2012.

[6] P. Patel, A. Mackinnon, M. Key, T. Cowan, M. Foord, M. Allen, D. Price, H. Ruhl, P. Springer, and R. Stephens, "Isochoric heating of solid-density matter with an ultrafast proton beam," *Physical review letters*, vol. 91, no. 12, p. 125004, 2003.

[7] A. Zylstra, C. Li, H. Rinderknecht, F. Séguin, R. Petrasso, C. Stoeckl, D. Meyerhofer, P. Nilson, T. Sangster, S. Le Pape, A. Mackinnon, and P. Patel, "Using high-intensity laser-generated energetic protons to radiograph directly driven implosions," *Review of scientific instruments*, vol. 83, no. 1, p. 013511, 2012.

[8] K. Ledingham and P. Norreys, "Nuclear physics merely using a light source," *Contemporary Physics*, vol. 40, no. 6, pp. 367–383, 1999.

[9] S. Mangles, B. Walton, Z. Najmudin, A. Dangor, K. Krushelnick, V. Malka, M. Manclossi, N. Lopes, C. Carias, G. Mendes, and F. Dorchies, "Table-top laser-plasma acceleration as an electron radiography source," *Laser and Particle Beams*, vol. 24, no. 1, pp. 185–190, 2006.

[10] M. Bailly-Grandvaux, J. Santos, C. Bellei, P. Forestier-Colleoni, S. Fujioka, L. Giuffrida, J. Honrubia, D. Batani, R. Bouillaud, M. Chevrot, J. E. Cross, R. Crowston, S. Dorad, J. L.

Dubois, M. Ehret, G. Gregori, S. Hulin, S. Kojima, E. Loyez, J. R. Marques, A. Morace, P. H. Nicolai, M. Roth, S. Sakata, G. Schaumann, F. Serres, S. J, V. T. Tikhonchuk, N. Woolsey, and Z. Zhang, "Guiding of relativistic electron beams in dense matter by laser-driven magnetostatic fields," *Nature communications*, vol. 9, no. 1, pp. 1–8, 2018.

[11] W. Leemans, A. Gonsalves, H.-S. Mao, K. Nakamura, C. Benedetti, C. Schroeder, C. Tóth, J. Daniels, D. Mittelberger, S. Bulanov, J. L. Vay, C. G. R. Geddes, and E. Esarey, "Multi-gev electron beams from capillary-discharge-guided subpetawatt laser pulses in the self-trapping regime," *Physical review letters*, vol. 113, no. 24, p. 245002, 2014.

[12] S. Wilks, A. Langdon, T. Cowan, M. Roth, M. Singh, S. Hatchett, M. Key, D. Pennington, A. MacKinnon, and R. Snavely, "Energetic proton generation in ultra-intense laser–solid interactions," *Physics of plasmas*, vol. 8, no. 2, pp. 542–549, 2001.

[13] T. Esirkepov, M. Borghesi, S. Bulanov, G. Mourou, and T. Tajima, "Highly efficient relativistic-ion generation in the laser-piston regime," *Physical review letters*, vol. 92, no. 17, p. 175003, 2004.

[14] M. Bailly-Grandvaux, D. Kawahito, C. McGuffey, J. Strehlow, B. Edghill, M. Wei, N. Alexander, A. Haid, C. Brabetz, V. Bagnoud, R. Hollinger, M. G. Capeluto, J. J. Rocca, and F. N. Beg, "Ion acceleration from microstructured targets irradiated by high-intensity picosecond laser pulses," *Physical Review E*, vol. 102, no. 2, p. 021201, 2020.

[15] H. Rinderknecht, T. Wang, A. L. Garcia, G. Bruhaug, M. Wei, H. Quevedo, T. Ditmire, J. Williams, A. Haid, D. Doria, T. T. Spohr, K M, and A. Arefiev, "Relativistically transparent magnetic filaments: scaling laws, initial results and prospects for strong-field qed studies," *New Journal of Physics*, vol. 23, no. 9, p. 095009, 2021.

[16] A. Higginson, R. Gray, M. King, R. Dance, S. Williamson, N. Butler, R. Wilson, R. Capdessus, C. Armstrong, J. Green, S. J. Hawkes, P. Martin, W. Q. Wei, S. R. Mirfayzi, X. H. Yuan, S. Kar, M. Borghesi, R. J. Clarke, D. Neely, and P. McKenna, "Near-100 mev protons via a laser-driven transparency-enhanced hybrid acceleration scheme," *Nature communications*, vol. 9, no. 1, pp. 1–9, 2018.

[17] A. Einstein, "Zur quantentheorie der strahlung," *First published in*, pp. 121–128, 1916.

[18] H. Kopfermann and R. Ladenburg, "Experimental proof of 'negative dispersion.'," *Nature*, vol. 122, no. 3073, pp. 438–439, 1928.

[19] A. Kastler, "Optical methods of atomic orientation and of magnetic resonance," *JOSA*, vol. 47, no. 6, pp. 460–465, 1957.

[20] J. P. Gordon, H. J. Zeiger, and C. H. Townes, "The maser—new type of microwave amplifier, frequency standard, and spectrometer," *Physical review*, vol. 99, no. 4, p. 1264, 1955.

[21] J. T. Verdeyen, "Laser electronics," 1989.

[22] J. Jarnestad, "Tools made of light," *Royal Swedish Academy of Sciences*, Press release, 2018.

[23] J. R. Klauder, A. Price, S. Darlington, and W. J. Albersheim, "The theory and design of chirp radars," *Bell System Technical Journal*, vol. 39, no. 4, pp. 745–808, 1960.

[24] J. W. Yoon, Y. G. Kim, I. W. Choi, J. H. Sung, H. W. Lee, S. K. Lee, and C. H. Nam, "Realization of laser intensity over 10^{23} watts/cm^2," *Optica*, vol. 8, no. 5, pp. 630–635, 2021.

[25] P. Mulser and D. Bauer, *High power laser-matter interaction*, vol. 238. Springer, 2010.

[26] D. Forslund, J. Kindel, and K. Lee, "Theory of hot-electron spectra at high laser intensity," *Physical Review Letters*, vol. 39, no. 5, p. 284, 1977.

[27] C. E. Max, "Physics of the coronal plasma in laser fusion targets," in *Laser-plasma interaction*, 1982.

[28] F. Brunel, "Not-so-resonant, resonant absorption," *Physical review letters*, vol. 59, no. 1, p. 52, 1987.

[29] P. Gibbon and E. Förster, "Short-pulse laser-plasma interactions," *Plasma physics and controlled fusion*, vol. 38, no. 6, p. 769, 1996.

[30] E. Fourkal, I. Velchev, and C.-M. Ma, "Coulomb explosion effect and the maximum energy of protons accelerated by high-power lasers," *Physical Review E*, vol. 71, no. 3, p. 036412, 2005.

[31] S. Bulanov, A. Brantov, V. Y. Bychenkov, V. Chvykov, G. Kalinchenko, T. Matsuoka, P. Rousseau, S. Reed, V. Yanovsky, D. Litzenberg, K. Krushelnick, and A. Maksimchuk, "Accelerating monoenergetic protons from ultrathin foils by flat-top laser pulses in the directed-coulomb-explosion regime," *Physical Review E*, vol. 78, no. 2, p. 026412, 2008.

[32] J. Li, A. V. Arefiev, S. S. Bulanov, D. Kawahito, M. Bailly-Grandvaux, G. M. Petrov, C. McGuffey, and F. N. Beg, "Ionization injection of highly-charged copper ions for laser driven acceleration from ultra-thin foils," *Scientific reports*, vol. 9, no. 1, pp. 1–11, 2019.

[33] A. Macchi, M. Borghesi, and M. Passoni, "Ion acceleration by superintense laser-plasma interaction," *Reviews of Modern Physics*, vol. 85, no. 2, p. 751, 2013.

[34] M. Borghesi, "Laser-driven ion acceleration: State of the art and emerging mechanisms," *Nuclear Instruments and Methods in Physics Research Section A: Accelerators, Spectrometers, Detectors and Associated Equipment*, vol. 740, pp. 6–9, 2014.

[35] M. Borghesi, A. Bigongiari, S. Kar, A. Macchi, L. Romagnani, P. Audebert, J. Fuchs, T. Toncian, O. Willi, S. Bulanov, A. J. MacKinnon, and J. C. Gauthier, "Laser-driven proton acceleration: source optimization and radiographic applications," *Plasma Physics and Controlled Fusion*, vol. 50, no. 12, p. 124040, 2008.

[36] A. A. Sahai, F. S. Tsung, A. R. Tableman, W. B. Mori, and T. C. Katsouleas, "Relativistically induced transparency acceleration of light ions by an ultrashort laser pulse interacting with a heavy-ion-plasma density gradient," *Physical Review E*, vol. 88, no. 4, p. 043105, 2013.

[37] T. Nakamura, S. V. Bulanov, T. Z. Esirkepov, and M. Kando, "High-energy ions from near-critical density plasmas via magnetic vortex acceleration," *Physical review letters*, vol. 105, no. 13, p. 135002, 2010.

[38] A. Macchi, F. Cattani, T. V. Liseykina, and F. Cornolti, "Laser acceleration of ion bunches at the front surface of overdense plasmas," *Physical review letters*, vol. 94, no. 16, p. 165003, 2005.

[39] P. Poole, L. Obst, G. Cochran, J. Metzkes, H. Schlenvoigt, I. Prencipe, T. Kluge, T. Cowan, U. Schramm, D. Schumacher, and K. Zeil, "Laser-driven ion acceleration via target normal sheath acceleration in the relativistic transparency regime," *New Journal of Physics*, vol. 20, no. 1, p. 013019, 2018.

[40] R. Mishra, F. Fiuza, and S. Glenzer, "Enhanced ion acceleration in transition from opaque to transparent plasmas," *New Journal of Physics*, vol. 20, no. 4, p. 043047, 2018.

[41] L. Yin, B. Albright, K. Bowers, D. Jung, J. Fernández, and B. Hegelich, "Three-dimensional dynamics of breakout afterburner ion acceleration using high-contrast short-pulse laser and nanoscale targets," *Physical review letters*, vol. 107, no. 4, p. 045003, 2011.

[42] B. Albright, L. Yin, K. J. Bowers, B. Hegelich, K. Flippo, T. Kwan, and J. Fernandez, "Relativistic buneman instability in the laser breakout afterburner," *Physics of Plasmas*, vol. 14, no. 9, p. 094502, 2007.

[43] B. Hegelich, I. Pomerantz, L. Yin, H. Wu, D. Jung, B. Albright, D. Gautier, S. Letzring, S. Palaniyappan, R. Shah, K. Allinger, R. Horlein, J. Schreiber, D. Habs, J. Blakeney, G. Dyer, L. Fuller, E. McCary, A. R. Meadows, C. Wang, T. Ditmire, and J. C. Fernandez, "Laser-driven ion acceleration from relativistically transparent nanotargets," *New Journal of physics*, vol. 15, no. 8, p. 085015, 2013.

[44] D. Jung, B. Albright, L. Yin, D. Gautier, B. Dromey, R. Shah, S. Palaniyappan, S. Letzring, H.-C. Wu, T. Shimada, R. Johnson, D. Habs, M. Roth, J. Fernandez, and B. Hegelich, "Scaling of ion energies in the relativistic-induced transparency regime," *Laser and Particle Beams*, vol. 33, no. 4, pp. 695–703, 2015.

[45] G. Petrov, C. McGuffey, A. Thomas, K. Krushelnick, and F. Beg, "Heavy ion acceleration in the radiation pressure acceleration and breakout afterburner regimes," *Plasma Physics and Controlled Fusion*, vol. 59, no. 7, p. 075003, 2017.

[46] D. Kawahito and Y. Kishimoto, "Ionization and acceleration of multiply charged gold ions in solid film irradiated by high intensity laser," *Physics of Plasmas*, vol. 27, no. 3, p. 033108, 2020.

[47] A. Robinson, P. Gibbon, M. Zepf, S. Kar, R. Evans, and C. Bellei, "Relativistically correct hole-boring and ion acceleration by circularly polarized laser pulses," *Plasma Physics and Controlled Fusion*, vol. 51, no. 2, p. 024004, 2009.

[48] A. Robinson, M. Zepf, S. Kar, R. Evans, and C. Bellei, "Radiation pressure acceleration of thin foils with circularly polarized laser pulses," *New journal of Physics*, vol. 10, no. 1, p. 013021, 2008.

[49] F. Fiuza, A. Stockem, E. Boella, R. Fonseca, L. Silva, D. Haberberger, S. Tochitsky, W. Mori, and C. Joshi, "Ion acceleration from laser-driven electrostatic shocks," *Physics of Plasmas*, vol. 20, no. 5, p. 056304, 2013.

[50] S. Wilks, W. Kruer, M. Tabak, and A. Langdon, "Absorption of ultra-intense laser pulses," *Physical review letters*, vol. 69, no. 9, p. 1383, 1992.

[51] M. Nishiuchi, N. Dover, M. Hata, H. Sakaki, K. Kondo, H. Lowe, T. Miyahara, H. Kiriyama, J. Koga, N. Iwata, M. A. Alkhimova, A. S. Prizhkov, A. Y. Faenov, T. A. Pikiz, A. Sagisaka, Y. Watanabe, M. Kando, K. Kondo, E. J. Ditter, O. C. Ettlinger, G. S. Hicks, Z. Najmudin, T. Ziegler, K. Zeil, U. Schramm, and Y. Sentoku, "Dynamics of laser-driven heavy-ion acceleration clarified by ion charge states," *Physical Review Research*, vol. 2, no. 3, p. 033081, 2020.

[52] S. Gitomer, R. Jones, F. Begay, A. Ehler, J. Kephart, and R. Kristal, "Fast ions and hot electrons in the laser–plasma interaction," *The Physics of fluids*, vol. 29, no. 8, pp. 2679–2688, 1986.

[53] P. Mora, "Plasma expansion into a vacuum," *Physical Review Letters*, vol. 90, no. 18, p. 185002, 2003.

[54] A. Arefiev, V. Khudik, A. Robinson, G. Shvets, L. Willingale, and M. Schollmeier, "Beyond the ponderomotive limit: Direct laser acceleration of relativistic electrons in sub-critical plasmas," *Physics of Plasmas*, vol. 23, no. 5, p. 056704, 2016.

[55] L. Ji, J. Snyder, A. Pukhov, R. Freeman, and K. Akli, "Towards manipulating relativistic laser pulses with micro-tube plasma lenses," *Scientific reports*, vol. 6, p. 23256, 2016.

[56] G. Marx, "Interstellar vehicle propelled by terrestrial laser beam," *Nature*, vol. 211, no. 5044, pp. 22–23, 1966.

[57] A. Macchi, S. Veghini, T. V. Liseykina, and F. Pegoraro, "Radiation pressure acceleration of ultrathin foils," *New Journal of Physics*, vol. 12, no. 4, p. 045013, 2010.

[58] L. Willingale, G. Petrov, A. Maksimchuk, J. Davis, R. Freeman, A. Joglekar, T. Matsuoka, C. Murphy, V. Ovchinnikov, A. Thomas, L. Van Woerkom, and K. Krushelnick, "Comparison of bulk and pitcher-catcher targets for laser-driven neutron production," *Physics of Plasmas*, vol. 18, no. 8, p. 083106, 2011.

[59] H. Schamel, "Stationary solitary, snoidal and sinusoidal ion acoustic waves," *Plasma Physics*, vol. 14, no. 10, p. 905, 1972.

[60] D. Haberberger, S. Tochitsky, F. Fiuza, C. Gong, R. A. Fonseca, L. O. Silva, W. B. Mori, and C. Joshi, "Collisionless shocks in laser-produced plasma generate monoenergetic high-energy proton beams," *Nature Physics*, vol. 8, no. 1, pp. 95–99, 2012.

[61] H. Zhang, B. Shen, W. Wang, Y. Xu, Y. Liu, X. Liang, Y. Leng, R. Li, X. Yan, J. Chen, , and Z. Z. Xu, "Collisionless shocks driven by 800 nm laser pulses generate high-energy carbon ions," *Physics of Plasmas*, vol. 22, no. 1, p. 013113, 2015.

[62] H. Zhang, B. Shen, W. Wang, S. Zhai, S. Li, X. Lu, J. Li, R. Xu, X. Wang, X. Liang, Y. X. Leng, R. X. Li, and Z. Z. Xu, "Collisionless shock acceleration of high-flux quasimonoenergetic proton beams driven by circularly polarized laser pulses," *Physical review letters*, vol. 119, no. 16, p. 164801, 2017.

[63] E. W. Gaul, M. Martinez, J. Blakeney, A. Jochmann, M. Ringuette, D. Hammond, T. Borger, R. Escamilla, S. Douglas, W. Henderson, G. Dyer, A. Erlandson, R. Cross, J. Caird, C. Ebbers, and T. Ditmire, "Demonstration of a 1.1 petawatt laser based on a hybrid optical parametric chirped pulse amplification/mixed nd: glass amplifier," *Applied optics*, vol. 49, no. 9, pp. 1676–1681, 2010.

[64] U. A. C. for HED Science, "Texas petawatt laser." Available at http://texaspetawatt.ph.utexas.edu/ (2021/10/21).

[65] D. O. of Science, "Center for high energy density science: Texas petawatt laser." Available at https://www.lasernetus.org/facility/center-high-energy-density-science-texas-petawatt-laser (2021/10/21).

[66] E. Gaul, T. Toncian, M. Martinez, J. Gordon, M. Spinks, G. Dyer, N. Truong, C. Wagner, G. Tiwari, M. Donovan, T. Ditmire, and B. M. Hegelich, "Improved pulse contrast on the texas petawatt laser," in *Journal of Physics: Conference Series*, vol. 717, p. 012092, IOP Publishing, 2016.

[67] R. Roycroft, B. Bowers, H. Smith, E. McCary, F. Aymond, G. M. Dyer, H. J. Quevedo, P. A. Bradley, E. L. Vold, L. Yin, and B. M. Hegelich, "Streaked optical pyrometer for proton-driven isochoric heating experiments of solid and foam targets," *AIP Advances*, vol. 10, no. 4, p. 045220, 2020.

[68] C. Freeman, G. Fiksel, C. Stoeckl, N. Sinenian, M. Canfield, G. Graeper, A. Lombardo, C. Stillman, S. Padalino, C. Mileham, T. Sangster, and J. Frenje, "Calibration of a thomson

parabola ion spectrometer and fujifilm imaging plate detectors for protons, deuterons, and alpha particles," *Review of Scientific Instruments*, vol. 82, no. 7, p. 073301, 2011.

[69] S. Bandyopadhyay, D. Neely, G. Gregori, D. Carroll, P. McKenna, M. Borghesi, F. Lindau, O. Lundh, C. Wahlström, and A. Higginbotham, "Analysis on a wedge-shaped thomson spectrometer for ion studies," tech. rep., Technical Report 1, Central Laser Facility, CCLRC Rutherford Appleton Lab, 2005.

[70] J. Cobble, K. Flippo, D. Offermann, F. Lopez, J. Oertel, D. Mastrosimone, S. Letzring, and N. Sinenian, "High-resolution thomson parabola for ion analysis," *Review of Scientific Instruments*, vol. 82, no. 11, p. 113504, 2011.

[71] H. Chen, A. J. Link, R. van Maren, P. K. Patel, R. Shepherd, S. C. Wilks, and P. Beiersdorfer, "High performance compact magnetic spectrometers for energetic ion and electron measurement in ultraintense short pulse laser solid interactions," *Review of Scientific Instruments*, vol. 79, no. 10, p. 10E533, 2008.

[72] N. Rabhi, D. Batani, G. Boutoux, J.-E. Ducret, K. Jakubowska, I. Lantuejoul-Thfoin, C. Nauraye, A. Patriarca, A. Saïd, A. Semsoum, L. Serani, B. Thomas, and B. Vauzour, "Calibration of imaging plate detectors to mono-energetic protons in the range 1-200 mev," *Review of Scientific Instruments*, vol. 88, no. 11, p. 113301, 2017.

[73] K. U. Akli, P. K. Patel, R. Van Maren, R. B. Stephens, M. H. Key, D. P. Higginson, B. Westover, C. D. Chen, A. J. Mackinnon, T. Bartal, F. N. Beg, S. Chawla, R. Fedosejevs, R. R. Freeman, D. S. Hey, G. E. Kemp, S. LePape, A. Link, T. Ma, A. G. MacPhee, H. S. McLean, Y. Ping, Y. Y. Tsui, L. D. Van Woerkom, M. S. Wei, T. Yabuuchi, and S. Yuspeh, "A dual channel x-ray spectrometer for fast ignition research," *Journal of Instrumentation*, vol. 5, no. 07, p. P07008, 2010.

[74] S. Glenzer, G. Gregori, F. Rogers, D. Froula, S. Pollaine, R. Wallace, and O. Landen, "X-ray scattering from solid density plasmas," *Physics of Plasmas*, vol. 10, no. 6, pp. 2433–2441, 2003.

[75] L. Pugachev, N. Andreev, P. Levashov, and O. Rosmej, "Acceleration of electrons under the action of petawatt-class laser pulses onto foam targets," *Nuclear Instruments and Methods in Physics Research Section A: Accelerators, Spectrometers, Detectors and Associated Equipment*, vol. 829, pp. 88–93, 2016.

[76] S. K. Saha, J. S. Oakdale, J. A. Cuadra, C. Divin, J. Ye, J.-B. Forien, L. B. Bayu Aji, J. Biener, and W. L. Smith, "Radiopaque resists for two-photon lithography to enable submicron 3d imaging of polymer parts via x-ray computed tomography," *ACS applied materials & interfaces*, vol. 10, no. 1, pp. 1164–1172, 2018.

[77] J. S. Oakdale, J. Ye, W. L. Smith, and J. Biener, "Post-print uv curing method for improving the mechanical properties of prototypes derived from two-photon lithography," *Optics express*, vol. 24, no. 24, pp. 27077–27086, 2016.

[78] Y. Liang, C. Zhen, D. Zou, and D. Xu, "Preparation of free-standing nanowire arrays on conductive substrates," *Journal of the American Chemical Society*, vol. 126, no. 50, pp. 16338–16339, 2004.

[79] B. Fryxell, K. Olson, P. Ricker, F. Timmes, M. Zingale, D. Lamb, P. MacNeice, R. Rosner, J. Truran, and H. Tufo, "Flash: An adaptive mesh hydrodynamics code for modeling astrophysical thermonuclear flashes," *The Astrophysical Journal Supplement Series*, vol. 131, no. 1, p. 273, 2000.

[80] M. Gittings, R. Weaver, M. Clover, T. Betlach, N. Byrne, R. Coker, E. Dendy, R. Hueckstaedt, K. New, W. R. Oakes, *et al.*, "The rage radiation-hydrodynamic code," *Computational Science & Discovery*, vol. 1, no. 1, p. 015005, 2008.

[81] K. Yee, "Numerical solution of initial boundary value problems involving maxwell's equations in isotropic media," *IEEE Transactions on antennas and propagation*, vol. 14, no. 3, pp. 302–307, 1966.

[82] R. Courant, K. Friedrichs, and H. Lewy, "Über die partiellen differenzengleichungen der mathematischen physik," *Mathematische annalen*, vol. 100, no. 1, pp. 32–74, 1928.

[83] S. Augst, D. D. Meyerhofer, D. Strickland, and S.-L. Chin, "Laser ionization of noble gases by coulomb-barrier suppression," *JOSA B*, vol. 8, no. 4, pp. 858–867, 1991.

[84] M. V. Ammosov, "Tunnel ionization of complex atoms and of atomic ions in an altemating electromagnetic field," *Sov. Phys. JETP*, vol. 64, p. 1191, 1987.

[85] D. Kawahito and Y. Kishimoto, "Multi-phase ionization dynamics of carbon thin film irradiated by high power short pulse laser," *Physics of Plasmas*, vol. 24, no. 10, p. 103105, 2017.

[86] T. Arber, K. Bennett, C. Brady, A. Lawrence-Douglas, M. Ramsay, N. Sircombe, P. Gillies, R. Evans, H. Schmitz, A. Bell, and C. P. Ridgers, "Contemporary particle-in-cell approach to laser-plasma modelling," *Plasma Physics and Controlled Fusion*, vol. 57, no. 11, p. 113001, 2015.

[87] A. Pak, K. Marsh, S. Martins, W. Lu, W. Mori, and C. Joshi, "Injection and trapping of tunnel-ionized electrons into laser-produced wakes," *Physical Review Letters*, vol. 104, no. 2, p. 025003, 2010.

[88] J. Derouillat, A. Beck, F. Pérez, T. Vinci, M. Chiaramello, A. Grassi, M. Flé, G. Bouchard, I. Plotnikov, N. Aunai, J. Dargent, C. Riconda, and M. Grech, "Smilei: A collaborative, open-source, multi-purpose particle-in-cell code for plasma simulation," *Computer Physics Communications*, vol. 222, pp. 351–373, 2018.

[89] X. Zhang, V. N. Khudik, A. Pukhov, and G. Shvets, "Laser wakefield and direct acceleration with ionization injection," *Plasma Physics and Controlled Fusion*, vol. 58, no. 3, p. 034011, 2016.

[90] Y.-K. Kim and M. E. Rudd, "Binary-encounter-dipole model for electron-impact ionization," *Physical Review A*, vol. 50, no. 5, p. 3954, 1994.

[91] M. E. Rudd and Y. Kim, "Electron-impact total ionization cross sections of ch and c2h2," 1997.

[92] V. Tarnovsky, A. Levin, H. Deutsch, and K. Becker, "Electron impact ionization of (x= 1-4)," *Journal of Physics B: Atomic, Molecular and Optical Physics*, vol. 29, no. 1, p. 139, 1996.

[93] Y.-K. Kim and J.-P. Desclaux, "Ionization of carbon, nitrogen, and oxygen by electron impact," *Physical Review A*, vol. 66, no. 1, p. 012708, 2002.

[94] J. Santos, F. Parente, and Y.-K. Kim, "Cross sections for k-shell ionization of atoms by electron impact," *Journal of Physics B: Atomic, Molecular and Optical Physics*, vol. 36, no. 21, p. 4211, 2003.

[95] D. Doria, S. Kar, H. Ahmed, A. Alejo, J. Fernandez, M. Cerchez, R. Gray, F. Hanton, D. MacLellan, P. McKenna, Z. Najmudin, D. Neely, L. Romognani, J. Ruiz, G. Sarri, C. Scullion, M. Streeter, M. Swantusch, O. Willi, M. Zepf, and M. Borghesi, "Calibration of bas-tr image plate response to high energy (3-300 mev) carbon ions," *Review of Scientific Instruments*, vol. 86, no. 12, p. 123302, 2015.

[96] J. Strehlow, P. Forestier-Colleoni, C. McGuffey, M. Bailly-Grandvaux, T. Daykin, E. McCary, J. Peebles, G. Revet, S. Zhang, T. Ditmire, M. Donovan, G. Dyer, J. Fuchs, E. Gaul, D. Higginson, G. Kemp, M. Martinez, H. McLean, M. Spinks, H. Sawada, and F. Beg, "The response function of fujifilm bas-tr imaging plates to laser-accelerated titanium ions," *Review of Scientific Instruments*, vol. 90, no. 8, p. 083302, 2019.

[97] A. Mančić, J. Fuchs, P. Antici, S. Gaillard, and P. Audebert, "Absolute calibration of photostimulable image plate detectors used as (0.5–20 mev) high-energy proton detectors," *Review of Scientific Instruments*, vol. 79, no. 7, p. 073301, 2008.

[98] A. Alejo, S. Kar, H. Ahmed, A. Krygier, D. Doria, R. Clarke, J. Fernandez, R. Freeman, J. Fuchs, A. Green, J. Green, D. Jung, A. Kleinschmidt, C. Lewis, J. Morrison, Z. Najmudin, H. Nakamura, G. Nersisyan, P. Norreys, M. Notley, M. Oliver, M. Roth, J. Ruiz, L. Vassura, M. Zepf, and M. Borghesi, "Characterisation of deuterium spectra from laser driven multispecies sources by employing differentially filtered image plate detectors in thomson spectrometers," *Review of Scientific Instruments*, vol. 85, no. 9, p. 093303, 2014.

[99] K. Bhutwala, M. Bailly-Grandvaux, J. Kim, M. Dozières, E. Galtier, C. B. Curry, M. Gauthier, E. Cunningham, H. J. Lee, P. Forestier-Colleoni, A. Higginson, N. Aybar, R. Hua, B. Edghill, J. Strehlow, G. Dyer, S. H. Glenzer, J. B. Kim, N. Alexander, E. Del Rio, M. S. Wei, Y. Ping, A. McKelvey, G. W. Collins, F. N. Beg, and C. McGuffey, "Development of a platform at the matter in extreme conditions end station for characterization of matter heated by intense laser-accelerated protons," *IEEE Transactions on Plasma Science*, vol. 48, no. 8, pp. 2751–2758, 2020.

[100] J. Green, M. Borghesi, C. Brenner, D. Carroll, N. Dover, P. Foster, P. Gallegos, S. Green, D. Kirby, K. Kirkby, P. McKenna, M. J. Merchant, Z. Najmudin, C. A. J. Palmer, D. Parker, R. Prasad, K. E. Quinn, P. P. Rajeev, M. P. Read, L. Romagnani, J. Shreiber, M. J. V. Streeter, O. Tresca, C. G. Wahlstrom, M. Zepf, and D. Neely, "Scintillator-based ion beam profiler for diagnosing laser-accelerated ion beams," in *Laser Acceleration of Electrons, Protons, and Ions; and Medical Applications of Laser-Generated Secondary Sources of Radiation and Particles*, vol. 8079, p. 807919, International Society for Optics and Photonics, 2011.

[101] T. Bonnet, M. Comet, D. Denis-Petit, F. Gobet, F. Hannachi, M. Tarisien, M. Versteegen, and M. Aleonard, "Response functions of fuji imaging plates to monoenergetic protons in the energy range 0.6–3.2 mev," *Review of Scientific Instruments*, vol. 84, no. 1, p. 013508, 2013.

[102] N. Sinenian, M. Rosenberg, M. Manuel, S. McDuffee, D. Casey, A. Zylstra, H. Rinderknecht, M. Gatu Johnson, F. Séguin, J. Frenje, C. K. Li, and R. D. Petrasso, "The response of cr-39 nuclear track detector to 1–9 mev protons," *Review of Scientific Instruments*, vol. 82, no. 10, p. 103303, 2011.

[103] J. F. Ziegler, M. D. Ziegler, and J. P. Biersack, *SRIM: the stopping and range of ions in matter*. Cadence Design Systems, 2008.

[104] B. Hidding, G. Pretzler, M. Clever, F. Brandl, F. Zamponi, A. Lübcke, T. Kämpfer, I. Uschmann, E. Förster, U. Schramm, R. Sauerbrey, E. Kroupp, L. Veisz, K. Schmid, S. Benavides, and S. Karsch, "Novel method for characterizing relativistic electron beams in a harsh laser-plasma environment," *Review of Scientific Instruments*, vol. 78, no. 8, p. 083301, 2007.

[105] H. Bethe, "Zur theorie des durchgangs schneller korpuskularstrahlen durch materie," *Annalen der Physik*, vol. 397, no. 3, pp. 325–400, 1930.

[106] T. Bonnet, M. Comet, D. Denis-Petit, F. Gobet, F. Hannachi, M. Tarisien, M. Versteegen, and M. Aléonard, "Response functions of imaging plates to photons, electrons and 4he particles," *Review of Scientific Instruments*, vol. 84, no. 10, p. 103510, 2013.

[107] J. B. Birks, "Scintillations from organic crystals: specific fluorescence and relative response to different radiations," *Proceedings of the Physical Society. Section A*, vol. 64, no. 10, p. 874, 1951.

[108] G. Chatterjee, P. K. Singh, S. Ahmed, A. Robinson, A. D. Lad, S. Mondal, V. Narayanan, I. Srivastava, N. Koratkar, J. Pasley, A. K. Sood, and G. R. Kumar, "Macroscopic transport of mega-ampere electron currents in aligned carbon-nanotube arrays," *Physical review letters*, vol. 108, no. 23, p. 235005, 2012.

[109] S. Jiang, L. Ji, H. Audesirk, K. George, J. Snyder, A. Krygier, P. Poole, C. Willis, R. Daskalova, E. Chowdhury, N. S. Lewis, D. W. Schumacher, A. Pukhov, R. R. Freeman,

and K. U. Akli, "Microengineering laser plasma interactions at relativistic intensities," *Physical review letters*, vol. 116, no. 8, p. 085002, 2016.

[110] D. Khaghani, M. Lobet, B. Borm, L. Burr, F. Gärtner, L. Gremillet, L. Movsesyan, O. Rosmej, M. E. Toimil-Molares, F. Wagner, and P. Neumayer, "Enhancing laser-driven proton acceleration by using micro-pillar arrays at high drive energy," *Scientific reports*, vol. 7, no. 1, pp. 1–9, 2017.

[111] A. Moreau, R. Hollinger, C. Calvi, S. Wang, Y. Wang, M. G. Capeluto, A. Rockwood, A. Curtis, S. Kasdorf, V. Shlyaptsev, V. Kaymak, A. Pukhov, and J. J. Rocca, "Enhanced electron acceleration in aligned nanowire arrays irradiated at highly relativistic intensities," *Plasma Physics and Controlled Fusion*, vol. 62, no. 1, p. 014013, 2019.

[112] D. Gozhev, S. Bochkarev, N. Busleev, A. Brantov, S. Kudryashov, A. Savel'ev, and V. Y. Bychenkov, "Laser-triggered stochastic volumetric heating of sub-microwire array target," *High Energy Density Physics*, vol. 37, p. 100856, 2020.

[113] D. Zou, D. Yu, X. Jiang, M. Yu, Z. Chen, Z. Deng, T. Yu, Y. Yin, F. Shao, H. Zhuo, C. T. Zhou, and S. C. Ruan, "Enhancement of target normal sheath acceleration in laser multi-channel target interaction," *Physics of Plasmas*, vol. 26, no. 12, p. 123105, 2019.

[114] T. Kluge, S. Gaillard, K. Flippo, T. Burris-Mog, W. Enghardt, B. Gall, M. Geissel, A. Helm, S. Kraft, T. Lockard, J. Metzkes, D. T. Offerman, M. Schollmeier, U. Schramm, K. Zeil, M. Bussman, and T. E. Cowan, "High proton energies from cone targets: electron acceleration mechanisms," *New Journal of Physics*, vol. 14, no. 2, p. 023038, 2012.

[115] D. Zou, A. Pukhov, L. Yi, H. Zhuo, T. Yu, Y. Yin, and F. Shao, "Laser-driven ion acceleration from plasma micro-channel targets," *Scientific reports*, vol. 7, no. 1, pp. 1–9, 2017.

[116] D. Zou, D. Yu, M. Yu, T. Huang, A. Pukhov, H. Zhuo, C. Zhou, and S. Ruan, "Efficient generation of 100 mev ions from ultrashort 1021 w cm- 2 laser pulse interaction with a waveguide target," *Nuclear Fusion*, vol. 59, no. 6, p. 066034, 2019.

[117] J. Bin, M. Yeung, Z. Gong, H. Wang, C. Kreuzer, M. Zhou, M. Streeter, P. Foster, S. Cousens, B. Dromey, J. Meyer-ter Vehn, M. Zepf, and J. Schreiber, "Enhanced laser-driven ion acceleration by superponderomotive electrons generated from near-critical-density plasma," *Physical review letters*, vol. 120, no. 7, p. 074801, 2018.

[118] J. Snyder, L. Ji, K. M. George, C. Willis, G. E. Cochran, R. Daskalova, A. Handler, T. Rubin, P. L. Poole, D. Nasir, A. Zingale, E. Chowdhury, B. F. Shen, and D. W. Schumacher, "Relativistic laser driven electron accelerator using micro-channel plasma targets," *Physics of Plasmas*, vol. 26, no. 3, p. 033110, 2019.

[119] V. Kaymak, A. Pukhov, V. N. Shlyaptsev, and J. J. Rocca, "Nanoscale ultradense z-pinch formation from laser-irradiated nanowire arrays," *Physical review letters*, vol. 117, no. 3, p. 035004, 2016.

[120] R. Hollinger, S. Wang, Y. Wang, A. Moreau, M. Capeluto, H. Song, A. Rockwood, E. Bayarsaikhan, V. Kaymak, A. Pukhov, V. N. Shlyaptsev, and J. Rocca, "Extreme ionization of heavy atoms in solid-density plasmas by relativistic second-harmonic laser pulses," *Nature Photonics*, vol. 14, no. 10, pp. 607–611, 2020.

[121] S. Mondal, Q. Wei, W. Ding, H. A. Hafez, M. Fareed, A. Laramée, X. Ropagnol, G. Zhang, S. Sun, Z. Sheng, J. Zhang, and T. Ozaki, "Aligned copper nanorod arrays for highly efficient generation of intense ultra-broadband thz pulses," *Scientific reports*, vol. 7, no. 1, pp. 1–8, 2017.

[122] A. Curtis, C. Calvi, J. Tinsley, R. Hollinger, V. Kaymak, A. Pukhov, S. Wang, A. Rockwood, Y. Wang, V. N. Shlyaptsev, and J. J. Rocca, "Micro-scale fusion in dense relativistic nanowire array plasmas," *Nature communications*, vol. 9, no. 1, pp. 1–7, 2018.

[123] S. Bochkarev, A. Brantov, D. Gozhev, and V. Y. Bychenkov, "Neutron production from structured targets irradiated by an ultrashort laser pulse," *Journal of Russian Laser Research*, vol. 42, no. 3, pp. 292–303, 2021.

[124] X. Jiang, D. Zou, Z. Zhao, L. Hu, P. Han, J. Yu, T. Yu, Y. Yin, and F. Shao, "Microstructure-assisted laser-driven photonuclear pulsed neutron source," *Physical Review Applied*, vol. 15, no. 3, p. 034032, 2021.

[125] R. Hollinger, C. Bargsten, V. N. Shlyaptsev, V. Kaymak, A. Pukhov, M. G. Capeluto, S. Wang, A. Rockwood, Y. Wang, A. Townsend, A. Prieto, P. Stockton, A. Curtis, and J. J. Rocca, "Efficient picosecond x-ray pulse generation from plasmas in the radiation dominated regime," *Optica*, vol. 4, no. 11, pp. 1344–1349, 2017.

[126] T. Wang, X. Ribeyre, Z. Gong, O. Jansen, E. d'Humières, D. Stutman, T. Toncian, and A. Arefiev, "Power scaling for collimated γ-ray beams generated by structured laser-irradiated targets and its application to two-photon pair production," *Physical Review Applied*, vol. 13, no. 5, p. 054024, 2020.

[127] S. Jiang, A. Link, D. Canning, J. Fooks, P. Kempler, S. Kerr, J. Kim, M. Krieger, N. Lewis, R. Wallace, G. J. Williams, S. Yalamanchili, and H. Chen, "Enhancing positron production using front surface target structures," *Applied Physics Letters*, vol. 118, no. 9, p. 094101, 2021.

[128] J.-J. Liu, T.-P. Yu, Y. Yin, X.-L. Zhu, and F.-Q. Shao, "All-optical bright γ-ray and dense positron source by laser driven plasmas-filled cone," *Optics express*, vol. 24, no. 14, pp. 15978–15986, 2016.

[129] Y. He, T. G. Blackburn, T. Toncian, and A. V. Arefiev, "Dominance of γ-γ electron-positron pair creation in a plasma driven by high-intensity lasers," *Communications Physics*, vol. 4, no. 1, pp. 1–9, 2021.

[130] D. Margarone, O. Klimo, I. Kim, J. Prokpek, J. Limpouch, T. Jeong, T. Mocek, J. Pšikal, H. Kim, J. Proška, K. H. Nam, L. Stolcova, I. W. Choi, S. K. Lee, J. H. Sung, T. J. Yu, and G. Korn, "Laser-driven proton acceleration enhancement by nanostructured foils," *Physical review letters*, vol. 109, no. 23, p. 234801, 2012.

[131] M. Dozières, G. Petrov, P. Forestier-Colleoni, P. Campbell, K. Krushelnick, A. Maksimchuk, C. McGuffey, V. Kaymak, A. Pukhov, M. Capeluto, R. Hollinger, V. N. Shlyaptsev, J. J. Rocca, and F. N. Beg, "Optimization of laser-nanowire target interaction to increase the proton acceleration efficiency," *Plasma Physics and Controlled Fusion*, vol. 61, no. 6, p. 065016, 2019.

[132] A. Zigler, S. Eisenman, M. Botton, E. Nahum, E. Schleifer, A. Baspaly, I. Pomerantz, F. Abicht, J. Branzel, G. Priebe, S. Steinke, A. Andreev, M. Schnuerer, W. Sandner, D. Gordon, P. Sprangle, and K. W. D. Ledingham, "Enhanced proton acceleration by an ultrashort laser interaction with structured dynamic plasma targets," *Physical review letters*, vol. 110, no. 21, p. 215004, 2013.

[133] L. Willingale, S. Mangles, S. Nagel, C. Bellei, A. Dangor, M. Kaluza, C. Kamberidis, S. Kneip, Z. Najmudin, P. Nilson, A. G. R. Thomas, and K. Krushelnick, "Proton acceleration from near critical density foam targets using the vulcan petawatt laser," *CLF Annual Report 2005/2006*, pp. 61–63, 2005.

[134] D. O. Golovin, S. R. Mirfayzi, Y. J. Gu, Y. Abe, Y. Honoki, T. Mori, H. Nagatomo, K. Okamoto, S. Shokita, K. Yamanoi, Y. Arikawa, G. Korn, T. A. Pikuz, F. Fujioka, R. Kodama, S. V. Bulanov, and A. Yogo, "Enhancement of ion energy and flux by the influence of magnetic reconnection in foam targets," *High Energy Density Physics*, vol. 36, p. 100840, 2020.

[135] B. Feng, L. Ji, B. Shen, X. Geng, Z. Guo, Q. Yu, T. Xu, and L. Zhang, "Effects of microstructures on laser-proton acceleration," *Physics of plasmas*, vol. 25, no. 10, p. 103109, 2018.

[136] G. Cantono, A. Permogorov, J. Ferri, E. Smetanina, A. Dmitriev, A. Persson, T. Fülöp, and C.-G. Wahlström, "Laser-driven proton acceleration from ultrathin foils with nanoholes," *Scientific Reports*, vol. 11, no. 1, pp. 1–10, 2021.

[137] N. Rabhi, K. Bohacek, D. Batani, G. Boutoux, J.-E. Ducret, E. Guillaume, K. Jakubowska, C. Thaury, and I. Thfoin, "Calibration of imaging plates to electrons between 40 and 180 mev," *Review of scientific instruments*, vol. 87, no. 5, p. 053306, 2016.

[138] A. C. Thompson and D. Vaughan, *X-ray data booklet*, vol. 8. Lawrence Berkeley National Laboratory, University of California Berkeley, CA, 2001.

[139] J. MacFarlane, I. Golovkin, and P. Woodruff, "Helios-cr–a 1-d radiation-magnetohydrodynamics code with inline atomic kinetics modeling," *Journal of Quantitative Spectroscopy and Radiative Transfer*, vol. 99, no. 1-3, pp. 381–397, 2006.

[140] J. Snyder, L. Ji, and K. Akli, "Enhancement of laser intensity and proton acceleration using micro-tube plasma lens targets," *Physics of plasmas*, vol. 23, no. 12, p. 123122, 2016.

[141] D. Offermann, R. Freeman, L. Van Woerkom, M. Foord, D. Hey, M. Key, A. Mackinnon, A. MacPhee, P. Patel, Y. Ping, J. Sanchez, N. Shen, T. Bartal, F. N. Beg, L. Espada, and C. D. Chen, "Observations of proton beam enhancement due to erbium hydride on gold foil targets," *Physics of Plasmas*, vol. 16, no. 9, p. 093113, 2009.

[142] Z. Lécz, J. Budai, A. Andreev, and S. Ter-Avetisyan, "Thickness of natural contaminant layers on metal surfaces and its effects on laser-driven ion acceleration," *Physics of Plasmas*, vol. 27, no. 1, p. 013105, 2020.

[143] C. McGuffey, J. Kim, M. Wei, P. Nilson, S. Chen, J. Fuchs, P. Fitzsimmons, M. Foord, D. Mariscal, H. McLean, P. K. Patel, R. B. Stephens, and F. N. Beg, "Focussing protons from a kilojoule laser for intense beam heating using proximal target structures," *Scientific reports*, vol. 10, no. 1, pp. 1–10, 2020.

[144] N. Naumova, I. Sokolov, J. Nees, A. Maksimchuk, V. Yanovsky, and G. Mourou, "Attosecond electron bunches," *Physical review letters*, vol. 93, no. 19, p. 195003, 2004.

[145] S. Busold, A. Almomani, V. Bagnoud, W. Barth, S. Bedacht, A. Blažević, O. Boine-Frankenheim, C. Brabetz, T. Burris-Mog, T. Cowan, O. Deppert, M. Droba, H. Eickhoff, U. Eisenbarth, K. Harres, G. Hoffmeister, O. Jaeckel, R. Jaeger, M. Joost, S. Kraft, F. Kroll, M. Kaluza, O. Kester, Z. Lecz, T. Merz, F. Nurnberg, H. Al-Omari, A. Orzhekhovskaya, G. Paulus, J. Polz, U. Ratzinger, M. Roth, G. Schaumann, P. Schmidt, U. Schramm, G. Schreiber, D. Schumacher, T. Stoehlker, A. Tauschwitz, W. Vinzenz, F. Wagner, S. Yaramyshev, and B. Zielbauer, "Shaping laser accelerated ions for future applications–the light collaboration," *Nuclear Instruments and Methods in Physics Research Section A: Accelerators, Spectrometers, Detectors and Associated Equipment*, vol. 740, pp. 94–98, 2014.

[146] J. Apiñaniz, S. Malko, R. Fedosejevs, W. Cayzac, X. Vaisseau, D. de Luis, G. Gatti, C. McGuffey, M. Bailly-Grandvaux, K. Bhutwala, V. Ospina-Bohorquez, J. Balboa, J. J. Santos, D. Batani, F. N. Beg, L. Roso, J. A. Perez-Hernandez, and L. Volpe, "A quasi-monoenergetic short time duration compact proton source for probing high energy density states of matter," *Scientific Reports*, vol. 11, no. 1, pp. 1–11, 2021.

[147] K. Lancaster, S. Karsch, H. Habara, F. Beg, E. Clark, R. Freeman, M. Key, J. King, R. Kodama, K. Krushelnick, K. W. D. Ledingham, P. McKenna, C. D. Murphy, P. A. Norreys, R. Stephens, C. Stoeckl, Y. Toyama, M. S. Wei, and M. Zepf, "Characterization of 7 li (p, n) 7 be neutron yields from laser produced ion beams for fast neutron radiography," *Physics of plasmas*, vol. 11, no. 7, pp. 3404–3408, 2004.

[148] M. Roth, D. Jung, K. Falk, N. Guler, O. Deppert, M. Devlin, A. Favalli, J. Fernandez, D. Gautier, M. Geissel, R. Haight, C. E. Hamilton, B. M. Hegelich, R. P. Johnson, F. Merril, G. Schaumann, K. Schoenberg, M. Schollmeier, T. Shimada, T. Taddeucci, J. L. Tybo,

F. Wagner, S. A. Wender, C. H. Wilde, and G. A. Wurden, "Bright laser-driven neutron source based on the relativistic transparency of solids," *Physical review letters*, vol. 110, no. 4, p. 044802, 2013.

[149] S. Palaniyappan, D. C. Gautier, B. J. Tobias, J. Fernandez, J. Mendez, T. Burris-Mog, C. Huang, A. Favalli, J. Hunter, M. Espy, D. W. Schmidt, R. O. Nelson, A. Sefkow, T. Shimada, and R. P. Johnson, "Mev bremsstrahlung x rays from intense laser interaction with solid foils," *Laser and Particle Beams*, vol. 36, no. 4, pp. 502–506, 2018.

[150] F. Wagner, O. Deppert, C. Brabetz, P. Fiala, A. Kleinschmidt, P. Poth, V. Schanz, A. Tebartz, B. Zielbauer, M. Roth, T. Stohlker, and V. Bagnoud, "Maximum proton energy above 85 mev from the relativistic interaction of laser pulses with micrometer thick ch 2 targets," *Physical review letters*, vol. 116, no. 20, p. 205002, 2016.

[151] A. Henig, S. Steinke, M. Schnürer, T. Sokollik, R. Hörlein, D. Kiefer, D. Jung, J. Schreiber, B. Hegelich, X. Yan, J. Meyer-ter Vehn, T. Tajima, P. V. Nickles, W. Sandner, and D. Habs, "Radiation-pressure acceleration of ion beams driven by circularly polarized laser pulses," *Physical Review Letters*, vol. 103, no. 24, p. 245003, 2009.

[152] S. Steinke, A. Henig, M. Schnürer, T. Sokollik, P. Nickles, D. Jung, D. Kiefer, R. Hörlein, J. Schreiber, T. Tajima, X. Q. Yan, B. M. Hegelich, J. Meyer-ter Vehn, W. Sandner, and D. Habs, "Efficient ion acceleration by collective laser-driven electron dynamics with ultra-thin foil targets," *laser and particle beams*, vol. 28, no. 1, pp. 215–221, 2010.

[153] D. Jung, B. Albright, L. Yin, D. Gautier, R. Shah, S. Palaniyappan, S. Letzring, B. Dromey, H. Wu, T. Shimada, R. P. Johnson, M. Roth, J. C. Fernandez, D. Habs, and B. M. Hegelich, "Beam profiles of proton and carbon ions in the relativistic transparency regime," *New Journal of Physics*, vol. 15, no. 12, p. 123035, 2013.

[154] C. Scullion, D. Doria, L. Romagnani, A. Sgattoni, K. Naughton, D. Symes, P. McKenna, A. Macchi, M. Zepf, S. Kar, and M. Borghesi, "Polarization dependence of bulk ion acceleration from ultrathin foils irradiated by high-intensity ultrashort laser pulses," *Physical review letters*, vol. 119, no. 5, p. 054801, 2017.

[155] T. V. Liseykina, M. Borghesi, A. Macchi, and S. Tuveri, "Radiation pressure acceleration by ultraintense laser pulses," *Plasma Physics and Controlled Fusion*, vol. 50, no. 12, p. 124033, 2008.

[156] G. Petrov, C. McGuffey, A. Thomas, K. Krushelnick, and F. Beg, "Proton acceleration from high-contrast short pulse lasers interacting with sub-micron thin foils," *Journal of Applied Physics*, vol. 119, no. 5, p. 053302, 2016.

[157] T. Takizuka and H. Abe, "A binary collision model for plasma simulation with a particle code," *Journal of computational physics*, vol. 25, no. 3, pp. 205–219, 1977.

[158] Y. Sentoku and A. J. Kemp, "Numerical methods for particle simulations at extreme densities and temperatures: Weighted particles, relativistic collisions and reduced currents," *Journal of Computational Physics*, vol. 227, no. 14, pp. 6846–6861, 2008.

[159] L. Spitzer Jr and R. Härm, "Transport phenomena in a completely ionized gas," *Physical Review*, vol. 89, no. 5, p. 977, 1953.

[160] A. Macchi, *A superintense laser-plasma interaction theory primer*. Springer Science & Business Media, 2013.

[161] M. Kaluza, J. Schreiber, M. I. Santala, G. D. Tsakiris, K. Eidmann, J. Meyer-ter Vehn, and K. J. Witte, "Influence of the laser prepulse on proton acceleration in thin-foil experiments," *Physical review letters*, vol. 93, no. 4, p. 045003, 2004.

[162] A. Kramida, Yu. Ralchenko, J. Reader, and and NIST ASD Team. NIST Atomic Spectra Database (ver. 5.7.1), [Online]. Available: `https://physics.nist.gov/asd` [2020, April 29]. National Institute of Standards and Technology, Gaithersburg, MD., 2019.

[163] J. Li, P. Forestier-Colleoni, M. Bailly-Grandvaux, C. McGuffey, A. Arefiev, S. Bulanov, J. Peebles, C. Krauland, A. Hussein, T. Batson, J. C. Fernandez, S. Palaniyappan, R. P. Johnson, G. M. Petrov, and F. N. Beg, "Laser-driven acceleration of quasi-monoenergetic, near-collimated titanium ions via a transparency-enhanced acceleration scheme," *New Journal of Physics*, vol. 21, no. 10, p. 103005, 2019.

[164] J. Barnard, J. Armijo, and F. Bieniosek, "Ion-beam-driven warm dense matter experiments," in *Journal of Physics: Conference Series*, vol. 244, p. 032028, 2010.

[165] M. Nishiuchi, H. Sakaki, T. Z. Esirkepov, K. Nishio, T. Pikuz, A. Y. Faenov, I. Y. Skobelev, R. Orlandi, H. Sako, A. Pirozhkov, K. Matsukawa, A. Sagisaka, K. Ogura, M. Kanasaki, H. Kiriyama, Y. Fukuda, H. Koura, M. Kando, T. Yamauchi, Y. Watanabe, S. V. Bulanov, K. Kondo, K. Imai, and S. Nagamiya, "Acceleration of highly charged gev fe ions from a low-z substrate by intense femtosecond laser," *Physics of Plasmas*, vol. 22, no. 3, p. 033107, 2015.

[166] T. Wang, D. Blackman, K. Chin, and A. Arefiev, "Effects of simulation dimensionality on laser-driven electron acceleration and photon emission in hollow micro-channel targets," *arXiv preprint arXiv:2104.07251*, 2021.

[167] V. Lelasseux and J. Fuchs, "Modelling energy deposition in tr image plate detectors for various ion types," *Journal of Instrumentation*, vol. 15, no. 04, p. P04002, 2020.

[168] M. Nishiuchi, H. Sakaki, N. Dover, T. Miyahara, K. Shiokawa, S. Manabe, T. Miyatake, K. Kondo, K. Kondo, Y. Iwata, Y. Watanabe, and K. Kondo, "Ion species discrimination method by linear energy transfer measurement in fujifilm bas-sr imaging plate," *Review of Scientific Instruments*, vol. 91, no. 9, p. 093305, 2020.

[169] R. A. Fonseca, L. O. Silva, F. S. Tsung, V. K. Decyk, W. Lu, C. Ren, W. B. Mori, S. Deng, S. Lee, T. Katsouleas, and J. Adam, "Osiris: A three-dimensional, fully relativistic particle in cell code for modeling plasma based accelerators," in *International Conference on Computational Science*, pp. 342–351, Springer, 2002.

[170] D. Stark, T. Toncian, and A. Arefiev, "Enhanced multi-mev photon emission by a laser-driven electron beam in a self-generated magnetic field," *Physical review letters*, vol. 116, no. 18, p. 185003, 2016.

[171] B. J. Albright, "Laser-based radiographic imaging." Internal report, Los Alamos National Laboratory (2021).